

Silicon Nanotubes and Selected Investigations in Energy and Biomaterial Applications

by

ROBERTO GONZALEZ RODRIGUEZ

Bachelor of sciences, July 2011

Universidad de las Americas Puebla

Cholula, Puebla, Mexico

Submitted to the Graduate Faculty of

College of Science and Engineering

Texas Christian University

in partial fulfillment of the requirements

for the degree of

Doctor of Philosophy

May 2017

ACKNOWLEDGEMENTS

I would like to express my deep and sincere gratitude to my advisor, Dr. Jeffery L. Coffey, for his constant inspiration, guidance, encouragements and assistance throughout my graduate research at Texas Christian University. I would also like to thank to our collaborators Dr. Petra Granitzer and Dr. Klemens Rumpf of the Institute of Physics of Karl Franzens University, Saar group at the Hebrew University, Alexander T. Tesfaye and Thierry Djenizian at Aix-Marseille University, France. The Robert A. Welch Foundation is gratefully acknowledged for financial support. I also want to thank to Dr Coffey Lab members, Friends, and Family.

Table of Contents

| | |
|---|-----------|
| Acknowledgments..... | ii |
| Table of contents..... | iii |
| List of figures | vi |
| List of tables | xii |
| I. Literature Review | 1 |
| 1.1. Semiconductor Nanoparticles | 2 |
| 1.1.1. Fabrication Methods of Silicon Nanoparticles | 3 |
| 1.1.1.1. Chemical Routes | 3 |
| 1.1.1.2. Pulse Laser Ablation | 5 |
| 1.1.1.3. Ball Milling | 6 |
| 1.2. Silicon Nanowires | 7 |
| 1.2.1. Nanowire Fabrication Mechanisms | 9 |
| 1.2.1.1. Vapor Liquid Solid (VLS)..... | 9 |
| 1.2.1.2. Solution based synthesis | 10 |
| 1.2.2. Applications of Silicon Nanowires | 11 |
| 1.3. Porous Silicon (pSi) | 13 |
| 1.3.1. Porous Silicon fabrication process | 14 |
| 1.3.1.1. Anodization | 14 |
| 1.3.1.2. Stain Etching | 15 |
| 1.3.2. Application of pSi in drug delivery | 16 |
| 1.4. Silicon Nanotubes (SiNTs) | 17 |
| 1.4.1. Filling Alumina Templates | 18 |
| 1.4.2. Arc discharge | 20 |
| 1.4.3. Zinc Oxide Template | 21 |
| II. Silicon Nanotubes Fabrication | 24 |
| 2.1. Introduction | 25 |
| 2.2. Experimental | 26 |
| 2.2.1. Substrate preparation..... | 26 |
| 2.2.2. ZnO nanocrystal seed preparation | 27 |
| 2.2.3. ZnO nanowire array fabrication..... | 27 |
| 2.2.4. Si deposition by Chemical Vapor Deposition (CVD) | 27 |
| 2.2.5. ZnO etching / template removal | 28 |
| 2.2.6. Silica dissolution assay | 28 |
| 2.3. Results and Discussion | 29 |
| 2.3.1. Growth of ZnO NW array templates | 29 |

| | | |
|----------|---|----|
| 2.3.2. | Si Deposition and etching of ZnO NWs. | 31 |
| 2.3.3. | Dissolution Assays of Si NTs | 38 |
| 2.4. | Summary | 40 |
| III. | Silicon Nanotubes and Applications in Lithium Ion Batteries | 41 |
| 3.1. | Introduction | 42 |
| 3.1.1. | Separator and Electrolyte | 45 |
| 3.1.2. | Cathode Materials | 45 |
| 3.1.3. | Anode Materials | 47 |
| 3.1.3.1. | Carbon | 48 |
| 3.1.3.2. | Lithium titanium Oxide | 49 |
| 3.1.3.3. | Silicon anodes | 49 |
| 3.1.3.4. | Silicon Nanotubes | 51 |
| 3.2. | Experimental | 52 |
| 3.2.1. | Assembly of lithium battery | 52 |
| 3.3. | Results and Discussion..... | 53 |
| 3.3.1. | SEM, TEM and EDX characterization | 53 |
| 3.3.2. | Electrochemical Characterization | 54 |
| 3.4. | Summary | 58 |
| IV. | Silicon Nanotubes Loaded with Iron Oxide Nanoparticles | 59 |
| 4.1. | Introduction | 60 |
| 4.2. | Experimental – Fundamental Magnetization Measurements..... | 61 |
| 4.2.1. | Loading of iron oxide nanoparticles in thick walled Si NTs | 61 |
| 4.2.2. | Procedure for loading 4 nm Fe ₃ O ₄ NPs in 10 nm Shell thickness Si NTs | 62 |
| 4.3. | Results and Discussion | 64 |
| 4.3.1. | Morphological characterization of Fe ₃ O ₄ NPs and Fe ₃ O ₄ NPs in Si NTs | 64 |
| 4.3.2. | Magnetic characterization of Fe ₃ O ₄ NPs and Fe ₃ O ₄ NPs in Si NTs | 65 |
| 4.4. | Experimental-Si NTs loaded with Iron Oxide Nanoparticles for Relaxometry Measurements..... | 69 |
| 4.4.1. | Loading of iron oxide nanoparticles in thick wall Si NTs | 69 |
| 4.4.2. | APTES and PEG-diacid (600) functionalization | 69 |
| 4.4.3. | Ferrozine assay | 71 |
| 4.5. | Results and Discussion | 71 |
| 4.5.1. | Si NTs loaded with Fe ₃ O ₄ NP characterization | 71 |
| 4.5.2. | T ₁ and T ₂ measurements | 73 |
| 4.6. | Summary | 79 |
| V. | Perovskite Formation Dictated by Silicon Nanotube Templates | 80 |
| 5.1. | Introduction | 81 |

| | |
|--|-----|
| 5.2. Experimental | 83 |
| 5.3. Results and Discussion | 85 |
| 5.3.1. Morphological characterization | 85 |
| 5.3.2. PL Characterization | 90 |
| 5.4. Bromide-Iodide systems | 94 |
| 5.5. Bromide-Chloride systems | 99 |
| 5.6. Summary | 105 |
| | |
| VI. Fabrication of solar cells using perovskite microwires and perovskites loaded into silicon nanotubes | 107 |
| 6.1. Introduction | 108 |
| 6.2. Solar cell fabrication process | 111 |
| 6.2.1. Experimental | 112 |
| 6.2.1.1. Titanium dioxide / Si NT deposition and fabrication | 112 |
| 6.2.1.2. Etching of FTO | 113 |
| 6.3. Results and Discussion | 114 |
| 6.3.1. Morphological characterization | 114 |
| 6.3.2. Electrical characterization | 115 |
| 6.4. Summary | 119 |
| | |
| VII. Concluding remarks..... | 120 |
| VIII. References | 124 |
| | |
| Vita and abstract | |

List of Figures

| | |
|--|----|
| 1. Energy level structure of a molecule, quantum dot and bulk solid | 3 |
| 2. TEM image of Si NPs embedded in an amorphous material..... | 4 |
| 3. A typical PLA system used to produce Si NPs | 5 |
| 4. Diameter of Si NPs as a function of helium pressure using PLA system | 6 |
| 5. Experimental designs for silicon nanowire preparation..... | 8 |
| 6. Vapor-liquid-solid (VLS) growth mechanism for nanowire (NW) synthesis..... | 9 |
| 7. SEM images of Si NWs obtained by a SLS method | 10 |
| 8. a) SEM of Si NWs and b) associated PL spectrum..... | 11 |
| 9. Binding and internalization of SiNWs (red) in CHO- β cells. | 13 |
| 10. Electrochemical cell used for porous Si formation | 15 |
| 11. Diagram show pSi pore expansion and functionalization | 16 |
| 12. Release profile using pSi vs pSi functionalized with 1-dodecene..... | 17 |
| 13. TEM morphology showing the coexistence of a) Si nanowires and b) Si nanotubes..... | 19 |
| 14. Mechanism to obtain Si nanowires and Si Nanotubes | 20 |
| 15. TEM of Si NTs produced by an arc-discharge technique | 21 |
| 16. Process to produce GaN nanotubes | 22 |
| 17. Characterization by TEM and EDX of GaN/ZnO core shell and GaN nanotubes | 23 |
| 18. Si NTs fabrication steps | 26 |

| | |
|--|----|
| 19. a) SEM image of a ZnO NW array on Si substrate. | 30 |
| 20. SEM and EDX of etched Si/ZnO NW samples with 10 nm Si shell thickness | 32 |
| 21. SEM and EDX of samples etched Si/ZnO NW with 60 nm Shell thickness | 33 |
| 22. Confocal fluorescence microscopy image of a Si NT array infiltrated with Ru(bpy) ₃ ²⁺ | 35 |
| 23. Different wall thickness of silicon nanotubes | 36 |
| 24. Silicon deposition system | 37 |
| 25. a) HR-TEM of unannealed SiNT and FFT associated with the HR-TEM image (inset). b) HR-TEM of Si NT after the annealing process and FFT associated with the HR-TEM image | 38 |
| 26. Dissolution of three different wall thickness Si NTs in PBS at 37 °C | 39 |
| 27. Dissolution of three different wall thickness Si NTs in PBS at 37 °C. | 39 |
| 28. A comparison of energy and power densities of common rechargeable batteries | 42 |
| 29. : Basic structure of a Lithium Ion Battery | 43 |
| 30. Crystal structures of representative intercalation cathodes..... | 46 |
| 31. Schematic representation of the plot of Li-ion battery cathode material potentials vs. capacity. | 46 |
| 32. Conversion type anodes as a function of specific capacity | 47 |
| 33. Crystal structures of (a) lithiated graphite, (b) lithium titanate (LTO), and (c) silicon during lithiation | 48 |
| 34. Schematic of morphological changes that occur in different morphologies of elemental Si during electrochemical cycling | 50 |

| | |
|--|----|
| 35. The schematic picture for the empty space in the silicon nanotube that allows for expansion during the discharging/charging processes | 51 |
| 36. Field-emission SEM image of SiNTs | 53 |
| 37. Cyclic voltammogram recorded for the SiNTs in the potential window of 0.01–1.75 V vs Li/Li+ at the scan rate of 0.1 mV s ⁻¹ | 54 |
| 38. (a) Galvanostatic discharge–charge profile of SiNTs at C/20 and (b) their cycling performance at multiple C-rates. | 56 |
| 39. SEM of Si NTs after lithiation | 57 |
| 40. EDX spectrum and atomic/weight percentages of Si NTs after lithiation | 58 |
| 41. Process for loading Fe ₃ O ₄ NPs in ‘uncapped’ Si NTs | 62 |
| 42. Process for loading Fe ₃ O ₄ NPs in Si NTs by magnetic field-assisted diffusion | 63 |
| 43. TEM images of Fe ₃ O ₄ NPs | 64 |
| 44. Si NTs loaded with 4 nm Fe ₃ O ₄ NPs..... | 65 |
| 45. ZFC/FC measurements showing size dependent shift of <i>T_B</i> in the case of Si NTs filled with Fe ₃ O ₄ NPs | 67 |
| 46. ZFC/FC measurements showing the effect of infiltrating a 10 nm Fe ₃ O ₄ NP sample with a polydisperse size range into a SiNT template with a 70 nm wall thickness..... | 68 |
| 47. Size distribution for 10 nm Fe ₃ O ₄ NPs from Sigma-Aldrich | 68 |
| 48. Diagram showing the process for Si NTs functionalized with APTES and PEG(diacid) | 70 |
| 49. Gradient of colours obtained during the calibration curve, | 71 |
| 50. TEM of 40 nm Si NTs | 72 |

| | |
|---|----|
| 51. Plots of T_2 vs Fe concentration for 5 nm Fe_3O_4 NPs in 40 nm and 70 nm wall thickness Si NTs in PBS and water | 74 |
| 52. Plots of T_2 vs Fe concentration for 8 nm Fe_3O_4 NPs in 40 nm and 70 nm wall thickness Si NTs in PBS and water | 74 |
| 53. Plots of T_1 vs Fe concentration for 5 and 8 nm Fe_3O_4 NPs in 40 nm and 70 nm wall thickness Si NTs in PBS and water | 75 |
| 54. Solar cell efficiencies for different systems | 82 |
| 55. Procedure for perovskite formation inside Si NTs; on the left, the procedure for perovskite microwires/cubes formation | 85 |
| 56. SEM image of $\text{CH}_3\text{NH}_3\text{PbI}_3$ microwires | 86 |
| 57. SEM for empty Si NTs | 87 |
| 58. TEM for empty Si NTs | 88 |
| 59. a) EDX-TEM line scan of 70 nm ID Si NTs, b) TEM image associated with the EDX-TEM line scan | 89 |
| 60. HRTEM for 70 nm ID SiNTs loaded with $\text{CH}_3\text{NH}_3\text{PbI}_3$. Lattice spacings associated with both the (002) and (220) directions are shown. | 89 |
| 61. Large area fluorescence image of a) $\text{CH}_3\text{NH}_3\text{PbI}_3$ microwires, b) 70 m ID Si NTs with $\text{CH}_3\text{NH}_3\text{PbI}_3$ | 90 |
| 62. PL (solid lines) and absorption (dashed lines) spectra for 200 nm (in green), 70 nm (in red) diameter perovskites loaded into SiNTs, and perovskite microwires (in blue); b) the absolute value of the first derivative of the absorbance | 91 |
| 63. PL spectra from room temperature down to 4 K for the perovskite nanostructures 70 nm in diameter, along with perovskite microwires | 93 |
| 64. SEM image of $\text{CH}_3\text{NH}_3\text{PbBr}_3$ microcubes | 94 |
| 65. Line scan of $\text{CH}_3\text{NH}_3\text{PbI}_{2.5}\text{Br}_{0.5}$ | 95 |

| | |
|---|-----|
| 66. Fluorescence image associated with $\text{CH}_3\text{NH}_3\text{PbBr}_3$ microcubes..... | 95 |
| 67. PL emission peaks of perovskite microcubes/microwires..... | 98 |
| 68. SEM Images of $\text{CH}_3\text{NH}_3\text{PbBr}_{0.5}\text{Cl}_{2.5}$ cubes..... | 100 |
| 69. TEM-EDX map for 70 nm ID Si NTs loaded with perovskites..... | 101 |
| 70. TEM-EDX lines scan of $\text{CH}_3\text{NH}_3\text{PbBr}_2\text{Cl}$ in 200 nm ID Si NT..... | 102 |
| 71. Fluorescence images of: a) $\text{CH}_3\text{NH}_3\text{PbBr}_{0.5}\text{Cl}_{2.5}$ cubes | 102 |
| 72. a) PL emission peaks of perovskite micro cubes..... | 105 |
| 73. Basic architecture of a perovskite solar cell | 108 |
| 74. Idealized equivalent circuit of a photovoltaic cell | 109 |
| 75. Typical forward bias I-V characteristics of a solar cell..... | 110 |
| 76. Solar cell structure..... | 111 |
| 77. Solar cell energy diagram for the perovskite-based structures described in this chapter | 112 |
| 78. a) ZnO NWs on FTO glass with the ZnO paste, b) Si-ZnO NWs and c) Si NTs after the etching process | 113 |
| 79. FTO etching process described in the section above | 114 |
| 80. SEM of cross section showing the thickness of FTO, TiO_2 and Si NTs. a) low magnification, b) high magnification | 115 |
| 81. SEM of carbon on a FTO glass substrate (top layer) | 115 |
| 82. Voltage versus current density plot of a solar cell fabricated with perovskite microwires | 116 |
| 83. SEM-EDX of FTO- TiO_2 - $\text{CH}_3\text{NH}_3\text{PbI}_3$ inside 200nm ID Si NTs..... | 117 |

List of Tables

| | |
|--|-----|
| 1. ZnO NW template diameter and length as a function of concentration, reaction time, and presence/absence of PEI | 30 |
| 2. τ_1 and τ_1 for films $\text{Ru}(\text{bpy})_3^{2+}$ and Si NTs with $\text{Ru}(\text{bpy})_3^{2+}$ | 35 |
| 3. Comparison of the electrochemical performance of various Si NTs with regard to lithium cycling | 56 |
| 4. r_1 , r_2 , and r_2/r_1 values associated with Fe_3O_4 NPs loaded in different Si NTs | 76 |
| 5. Mole ratios of precursors used for perovskite formation | 84 |
| 6. SEM-EDX at % composition data for $\text{CH}_3\text{NH}_3\text{PbI}_{2.25}\text{Br}_{0.75}$ formed as microwires ($\square w$) and inside Si NTs with 200 nm ID, 70 nm ID and 70 nm ID, as well as associated PL max in each case | 99 |
| 7. Mole ratios used for perovskite formation in Br-Cl systems | 99 |
| 8. Comparison of Solar cell parameter of controls, perovskite microwires and Si NTs loaded with perovskite | 118 |
| 9. Solar cell parameters based on grain size distribution in a $\text{CH}_3\text{NH}_3\text{PbI}_3$ perovskite based solar cell platform | 119 |

Chapter I
Literature Review

I Literature Review

Silicon (Si) has been recognized as one of the most important materials of the 20th century. It is due to its role as the fundamental component in integrated circuits and the subsequent microelectronic revolution.¹ Silicon, at a nanoscale feature size, has the advantages of higher surface area and associated unique physical and chemical properties.² There are several classes of silicon in nanostructured form currently under investigation, including spherical Si nanoparticles (Si NPs),³ one dimensional Si nanowires (Si NWs),⁴ porous Si (pSi) films and particles,⁵ and hollow Si nanotubes (SiNTs).⁶ Silicon is a very versatile material with applications in microelectronics,⁷ battery technology,⁸ solar cells⁹ and biomedical applications.¹⁰

1.1 Semiconductor Nanoparticles

In the past two decades there has been a significant amount of research concerning semiconductor nanoparticles that possess a narrow band gap, such as II-VI compound semiconductors CdTe, CdS, CdSe, IV-VI structures like PbTe, PbS, PbSe, and III-V materials such as InP and InAs.¹¹ Quantum Dots (QDs) have unique electronic characteristics, most prominently, the presence of more discrete energy levels (as a consequence of fewer atoms) and an associated size-dependent bandgap (as we can observe in Figure 1).¹² As a result, these QDs are sometimes referred to as ‘artificial atoms.’¹²

Selected applications with most of these quantum dots (QDs) are limited due to their toxicity.¹³ For this reason it is necessary to find new alternatives. In this regard, silicon (Si) is a promising material, especially for biomedical applications, due to its abundance and low toxicity.¹⁴

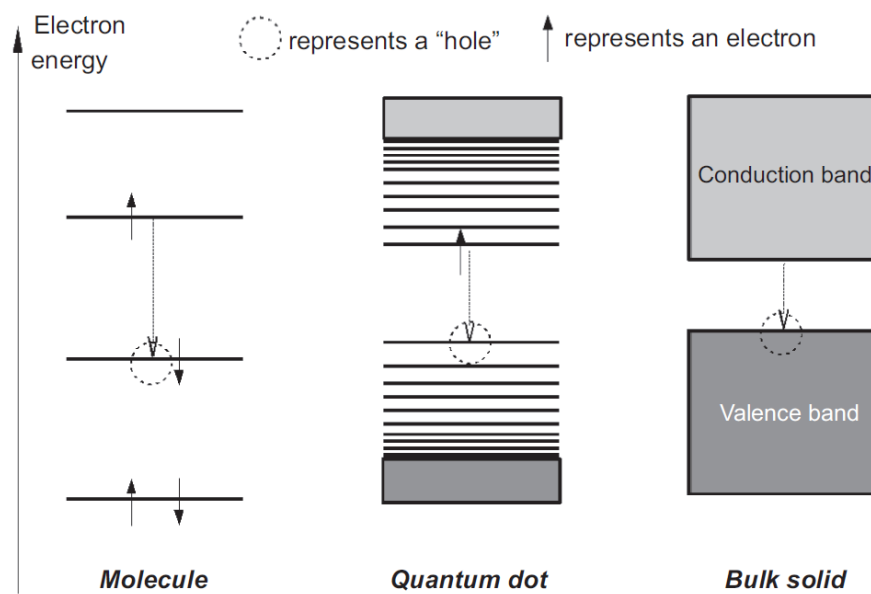


Figure 1: Energy level structure of a molecule, quantum dot and bulk solid. Adapted from Ref. 12.

1.1.1. Fabrication Methods of Silicon Nanoparticles

Silicon Nanoparticles (Si NPs) can be produced by a chemical or physical process. Examples of chemical routes to such nanoparticles include electrochemical methods¹⁴ and metal-catalyzed reduction.¹⁵ Si NPs can also be prepared by physical routes such as pulse laser ablation (PLA)¹⁶ and ball milling.¹⁷

1.1.1.1. Chemical Routes

Chemical routes are a preferred way to obtain large quantities of Si NPs. For example, one method consists of using “Zintl phases” such as NaSi to produce Si NPs (or NaGe for Ge NPs).¹⁸ These salts are typically mixed with metal halides like CuCl or CoBr₂ or ammonium salts like NH₄Cl, with reaction temperatures on the order of 200-500 °C.¹⁸ A Zintl phase contains tetrahedral clusters of Si₄⁴⁻ surrounded by Na⁺ atoms.¹⁹ When the Zintl phases are mixed with the metal halides the following reaction occurs:



In addition to nanocrystal yield, the other main advantage with this method is the strong photoluminescence (PL) intensity of the material, useful to applications to LEDs or imaging. However, the biggest problem is the material produced by this route is a lack of purity due to the presence of other solid products (e.g Na salts), and therefore purification steps have to be added. In addition, the particle size distribution is relatively wide (± 10 nm). In Figure 2, a TEM image of a typical reaction product is shown, illustrating crystalline Si NPs embedded in an amorphous matrix.¹⁸

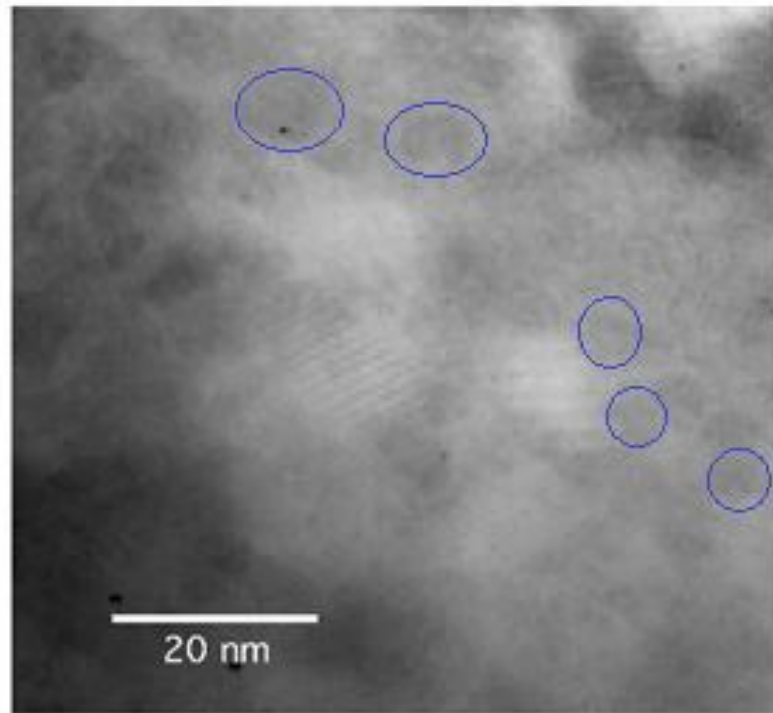


Figure 2: TEM image of Si NPs embedded in an amorphous material, blue circles represent the Si NPs location. Adapted from Ref. 18.

1.1.1.2. Pulse Laser Ablation

In contrast to the above chemical route, Pulse Laser Ablation (PLA) can produce nanoparticles that are very uniform in size. This technique involves ablation of a source of Si (usually a single crystalline silicon wafer) in an inert atmosphere using Helium in a low pressure chamber; and the Laser source is typically ArF with an excitation of 193 nm. A typical PLA system is illustrated in Figure 3. In this system the key components are (a) the laser; (b) the single crystalline wafer source (located in a rotating platform with a typical speed of 8 rpm); and (c) the substrate where the Si NPs are collected.²⁰

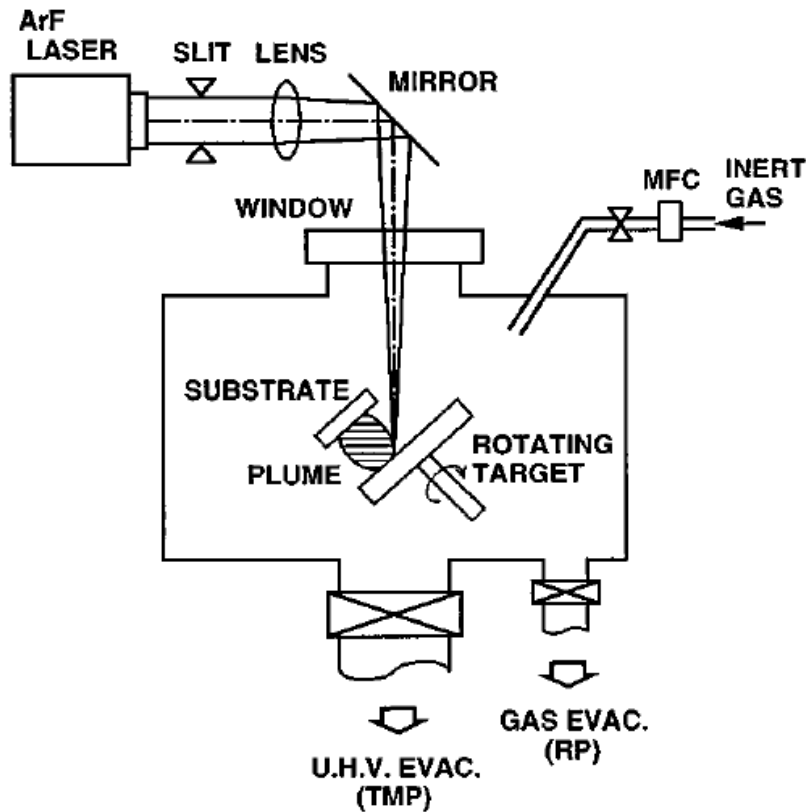


Figure 3: A typical PLA system used to produce Si NPs. Adapted from Ref. 20.

Si NPs produced by this technique are typically high quality single crystals that can be produced as small as 3 nm in diameter. Si NPs sizes in PLA are proportional to the gas pressure, explained by a simple inertia fluid model (illustrated in Figure 4); when the pressure of the gas is increased, particle diameter increases in a directly proportional manner. PLA is one possible method to produce high quality Si NPs in size and uniformity, a necessity for optoelectronic applications. The disadvantage, however, is the very low yield compared with chemical methods.²⁰

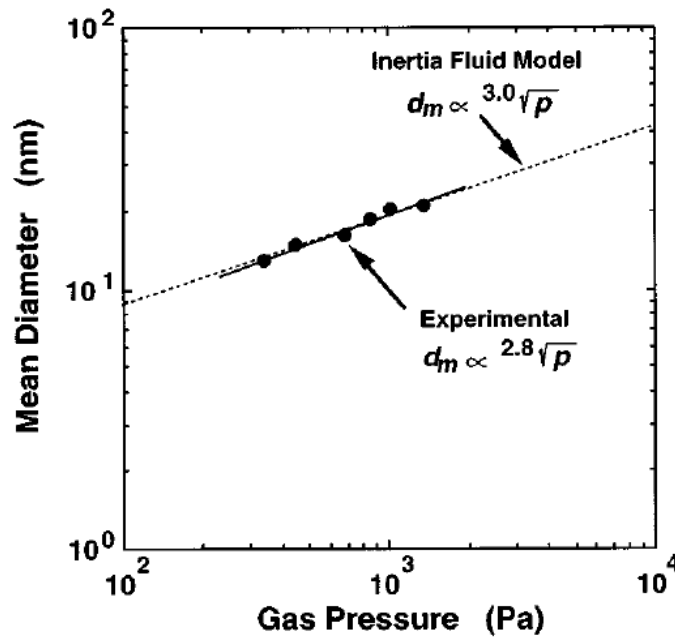


Figure 4: Diameter of Si NPs as a function of Helium pressure using PLA system, d_m =particle diameter (d_m = mean diameter; p = gas pressure). Adapted from Ref. 20.

1.1.1.3. Ball Milling

This method basically consists of grinding the material in bulk form and thereby obtaining very small particles. Ball milling is a good method to produce large quantities of

material. The process can be very long – requiring up to a week in an Argon atmosphere at 150°C. The disadvantages of the method is the rather weak PL intensity of the material (presumably due to defects), and it is difficult to obtain a uniform nanometer size distribution of (macro)particles, microparticles and nanoparticles coexisting.²¹ If silica particles are used as a starting material, this process can be combined with a carbothermic reduction reaction at 200°C to obtain Si NPs; the solid phase reaction that occurs in this process can be simply written as:



1.2. Silicon Nanowires

Treuting and Arnold in 1957 reported a method to prepare Si whiskers.²² Use of the term whisker refers to a relatively large Si microwire, structures no longer of significant interest, However, the basic fundamental mechanism used in their formation can be adapted to the nanoscale. Extensive research on nanoscale Si NWs did not start until the mid-1990s when Lieber and Morales reported a way to produce Si NWs based on laser ablation of a Si source in conjunction with a VLS mechanism.²³ There are several techniques for the synthesis of Si NWs, such as (1) Chemical Vapor Deposition (CVD), (2) Laser Ablation, (3) Solution based Synthesis, and (4) Molecular Beam Epitaxy. There are two main mechanisms that can explain nanowire formation (depending on the phase of the reactants): Vapor-Liquid-Solid (VLS) and Solution-Liquid-Solid (SLS). In Figure 5 we can observe the different experimental designs necessary to produce Si NWs.²⁴

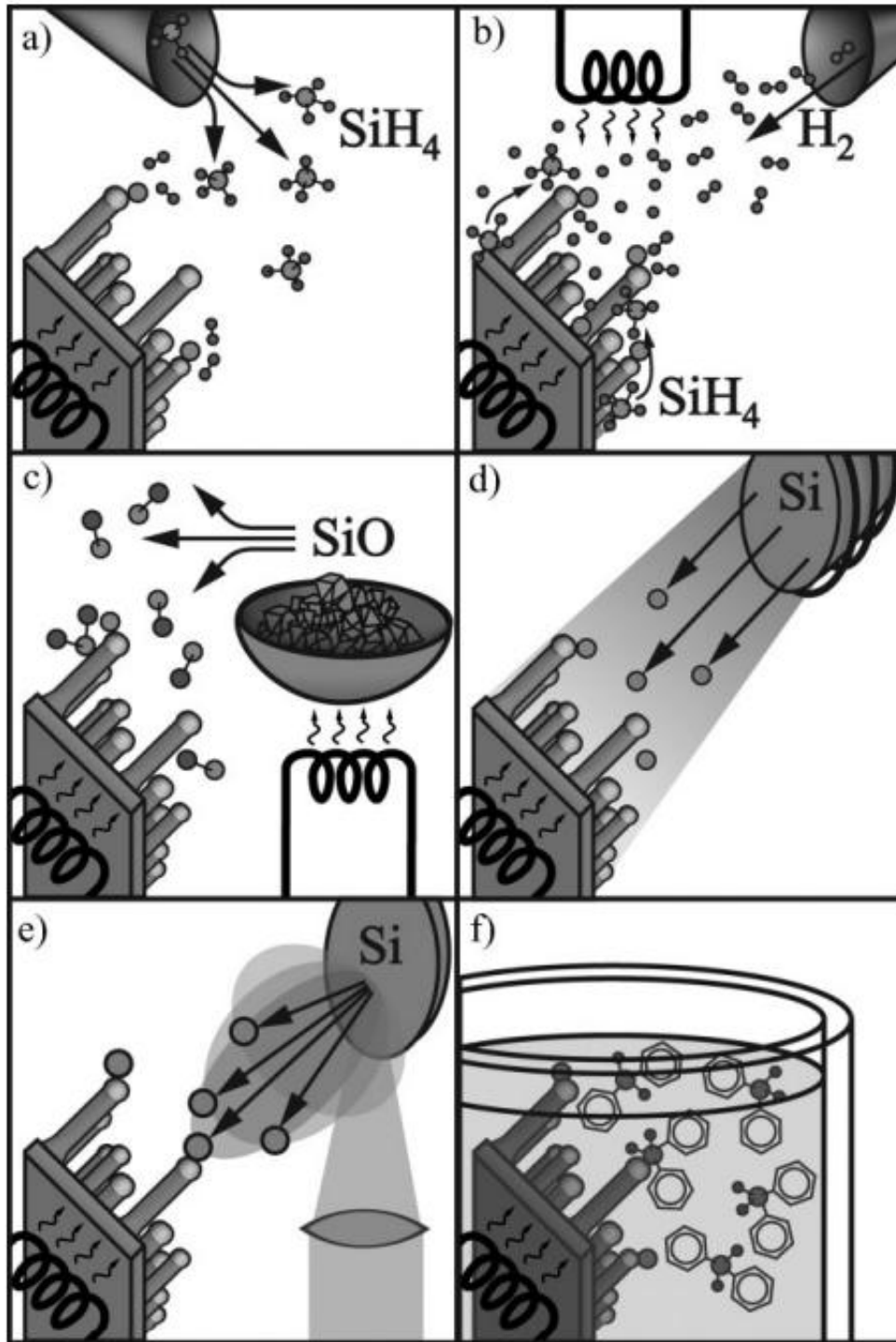


Figure 5: Experimental designs for Silicon nanowire preparation: a) CVD; b) annealing in reactive atmosphere; c) evaporation of SiO; d) MBE; e) laser ablation; and f) solution-based growth. Adapted from Ref. 24.

1.2.1. Nanowire Fabrication Mechanisms

1.2.1.1. Vapor Liquid Solid (VLS)

With this route the source of silicon is SiH_4 or SiCl_4 , and Au functions as a catalyst. With this method it is possible to obtain a tunable range of Si NW widths from micron size to a few nanometers. Some of the parameters that can be altered are the Si source, catalyst, and length of reaction time.^{25,26} In this mechanism, there are several key steps (Figure 6b): 1) silane decomposition at the vapor-liquid interface, 2) Si atom diffusion through the AuSi liquid, and 3) NW crystallization by Si incorporation into a step at the growing liquid-solid interface of the nanowire.^{27,28}

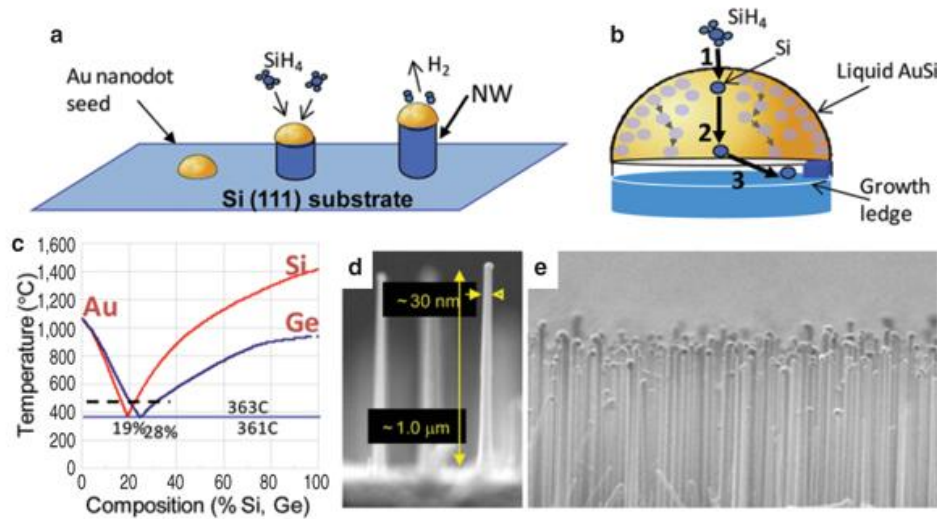


Figure 6: Vapor-liquid-solid (VLS) growth mechanism for nanowire (NW) synthesis. a) Schematic of VLS Si NW growth from a liquid Au catalyst seed which floats on top of the NW as it grows and defines the growth diameter. b) Enlarged view illustrating the three kinetic steps for NW growth. c) Binary phase diagrams for Au-Si and Au-Ge overlaid to illustrate their similar eutectic melt properties; dashed line indicates a typical growth temperature. d) and e) SEM images of Si NWs. Adapted from Ref. 28.

1.2.1.2. Solution based synthesis

In solution-based liquid solid (SLS) routes, the reaction conditions are economically more acceptable since the reaction is carried out at atmospheric pressure. In this process Au is also used as the catalyst, trisilane as silicon source, and squalene as a solvent with reaction temperatures less than 400 °C.²⁹ With this method the length of Si NWs are typically between 1 to 3 μm and a diameter around 30 nm; these parameters can be controlled with reaction time, catalyst used, as well as silicon source. While relatively high yields of Si NWs can be produced with this route, one of the disadvantages is that Si NWs are grown mainly along the (111) direction with a small quantity in the (110) direction and agglomeration occurs frequently.³⁰ In Figure 7 we can observe the agglomeration of Si NWs (via SEM) that occurs by this technique.

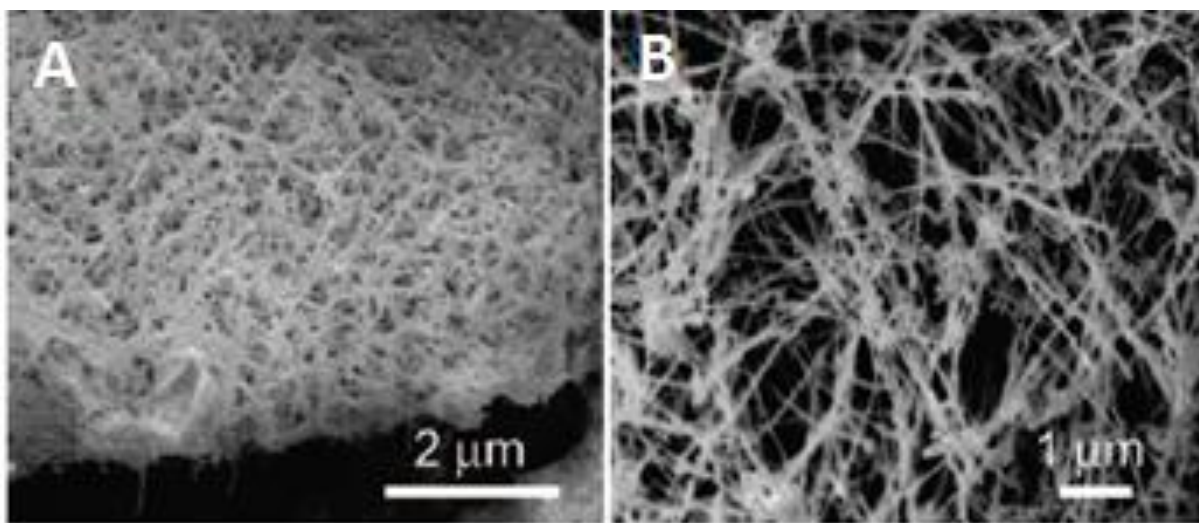


Figure 7: SEM images of Si NWs obtained by a SLS method. Adapted from Ref. 30.

1.2.2. Applications of Silicon Nanowires

Silicon nanowires have multiple applications in electronic devices, lithium batteries, drug delivery, sensors, and imaging.³¹ Si NWs contain a natural silicon oxide layer which makes their functionalization (based on silica chemistry) relatively straightforward.³² In an example relevant to therapeutics, Si NWs have been functionalized with folate; the reason for this conjugation is that malignant cells often overexpress folate, thereby facilitating targeted delivery of cancer therapeutics.³³ The synthesis of Si NWs were made using a VLS method using gold as a catalyst with a dimension of 40 nm. Si NWs obtained had a length from 2 to 8 microns. The SiNWs are readily imaged via SEM (Figure 8); the associated photoluminescence (PL) appears 645 nm. PL is important for bioimaging experiments, as this facilitates where Si NWs are located in the cell.³³

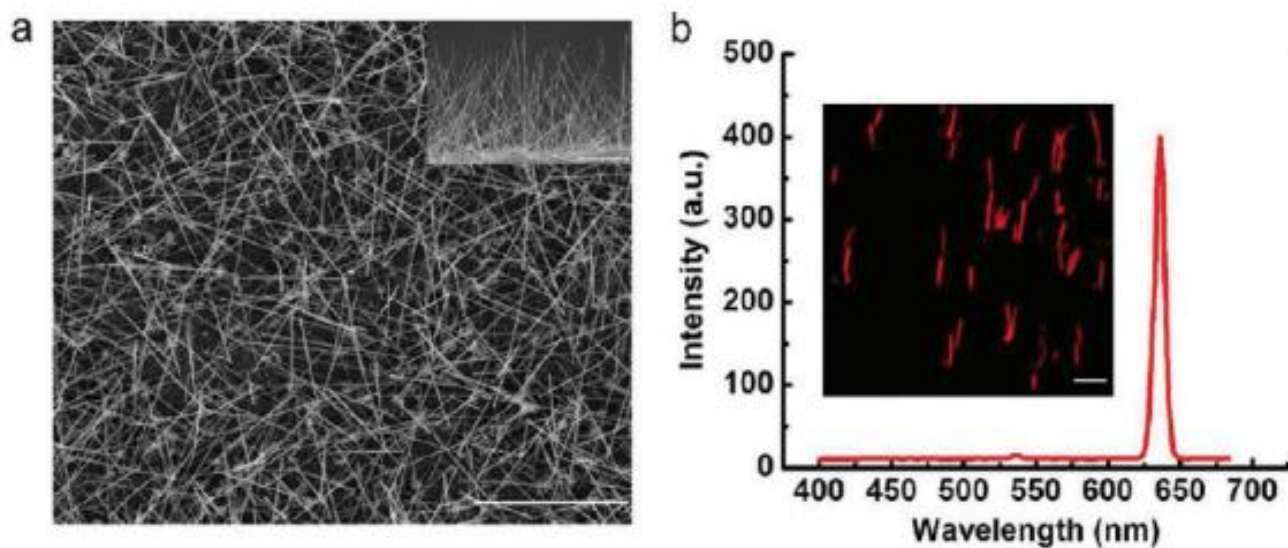


Figure 8: a) SEM of Si NWs and b) associated PL spectrum. Adapted from Ref. 33.

In order to prepare folate-functionalized Si NWs, a series of steps are required (Figure 9). First, Si NWs are treated with an oxygen plasma to obtain a uniform silicon oxide surface, then functionalized with 3-aminopropyltrimethoxysilane (APTMS) to obtain amino-terminated Si NWs. These steps are followed by reactions with a succinimide ester and finally the folate species.³⁴

In order to test the effectiveness of the above approach, the interaction of Si NWs with folate termination was examined; CHO cells were transfected with folate receptors since several cancer types overexpress this particular receptor (such as breast, brain, ovarian and lungs). Results from experiments with these folate-conjugated SiNWs were compared with amine-terminated Si NWs and unfunctionalized Si NWs as controls. In Figure 9, an in vitro comparison between these three types of SiNWs reveals that folate-functionalized Si NWs have the fastest cellular uptake.³³

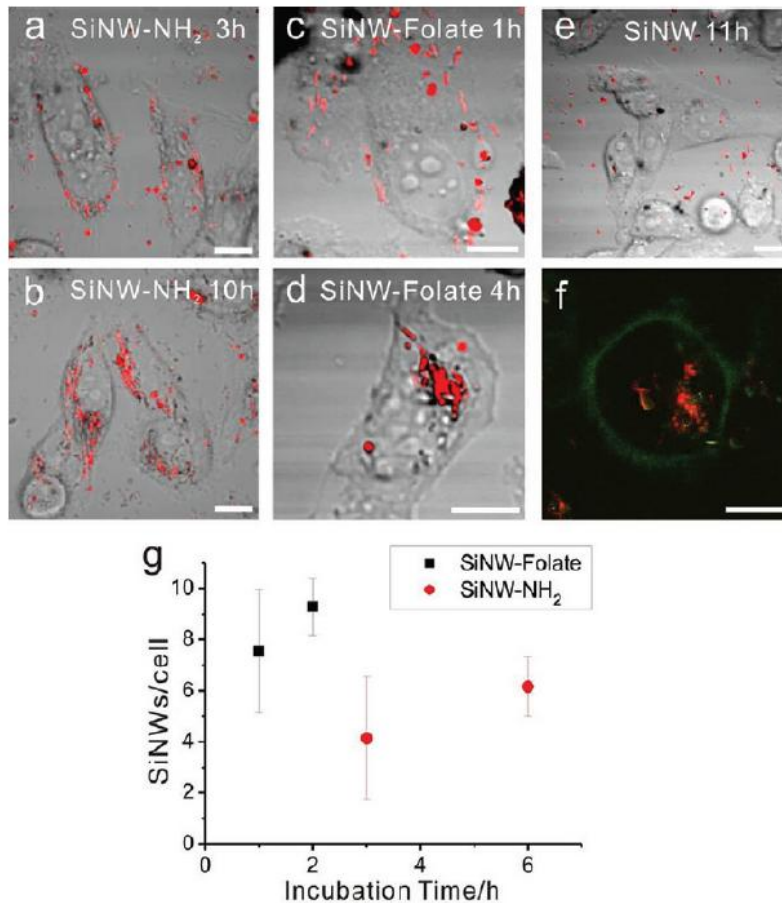


Figure 9: Binding and internalization of SiNWs (red) in CHO-β cells. (a and b) SiNW-NH₂ after incubation for 3 and 10 h, respectively, (c and d) SiNW-Folate after incubation for 1 and 4 h, respectively, and (e) untreated SiNWs after incubation for 11 h. (f) Fluorescence image of a CHO-β cell after internalization of SiNWs. Green, fluorescence from folate-FITC labeled cell membrane. (g) Average number of bound NWs per cell before the onset of internalization as a function of incubation time. Scale bars in a–f, 10 μm. Adapted from Ref. 33.

1.3. Porous Silicon (pSi)

Porous silicon was first discovered in 1956 by Uhlir during silicon electropolishing experiments.³⁵ In this process, hole injection at the outermost Si surface atoms result in their oxidation and subsequent dissolution of silicon occurs (in the form of SiF₆²⁻).³⁶ pSi is a form of elemental silicon that has nanopores present in its microstructure. In 1990, the light emitting properties of nanoporous silicon in the visible region was reported by L. Canham, who showed

room-temperature photoluminescence of an anodized p-type silicon wafer.³⁷ This was the first report of strong visible light emission from an indirect bandgap semiconductor, due likely to quantum confinement effects. pSi is a material which has attracted attention of researchers most prominently in the areas of optoelectronics³⁸ and drug delivery.³⁹

There are three categories for pSi classification:

Microporous: pSi structures with pore diameter < 2 nm.

Mesoporous: pSi structures with pore diameter in the 2-50nm region.

Macroporous: pSi structures with pore diameter > 50nm.

1.3.1. Porous Silicon fabrication process

1.3.1.1. Anodization

pSi is obtained most commonly by using a monocrystalline silicon wafer (c-Si) in an electrochemical oxidation process using methanol (or ethanol) and HF.⁴⁰ Pore size and morphology depends on the potential applied, current, dopant type and concentration, electrolyte, the duration of the etch, etc. As this method is relatively expensive for large scale industrial applications, more economical alternative fabrication routes must be explored; among these, the stain etching process is an appealing option.^{41,42}

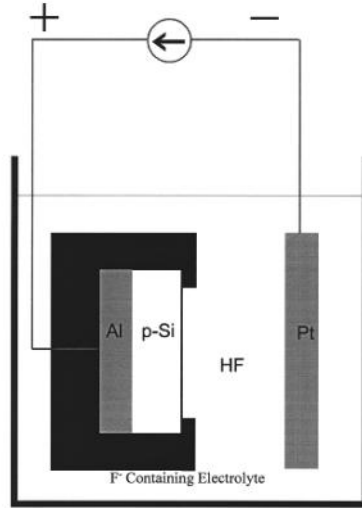
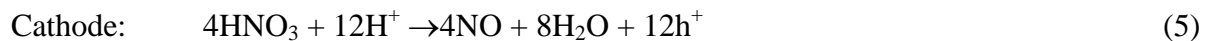
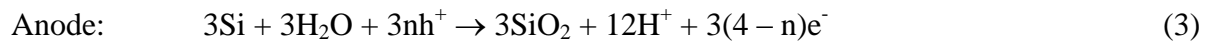


Figure 10. Electrochemical cell used for porous Si formation. Adapted from Ref. 41.

1.3.1.2. Stain Etching

The most common process to prepare stain etched porous silicon is by the immersion of c-Si in HF/NO₃/H₂O.⁴³ A corrosion process is taken place spontaneously on the silicon wafer where the porous are formed. The pore size depends on time and composition of the solution. The etching process in HF-HNO₃-based system on Si is well understood.⁴⁴ In the anode occurs the dissolution of silicon, in the cathode is the reduction of HNO₃ which causes holes (positive charge) to be injected into the silicon. The proposed mechanism is shown below, where e⁻ here refers to an electron and h⁺ represents a hole.



1.3.2. Application of pSi in drug delivery

In order to eliminate the need for multiple administrations of a given drug in the body over a certain period of time, a new drug delivery system is needed. This system should sustain drug release at a targeted concentration over long periods of time.⁴⁵ For this application, pSi is ideal because it permits diffusion of a drug located deep within its pores; it is also biocompatible,⁴⁶ and the pore area and volume can be controlled.⁴⁷ As a model in drug delivery using pSi, they used dexamethasone. Dexamethasone is a hydrophobic steroid, a drug used to treat allergies, asthma, and skin and lung diseases.

In this application porous silicon is obtained from p-type Si wafer, the etching process consisting of anodic electrochemical etching using a solution 1:1 (v/v) HF in ethanol at a constant current density of 33.3 mA/cm² for 5 min.⁴⁸ Since the drug is insoluble in water, functionalization with 1-dodecene has to be made. As observed in Figure 11, after pSi formation, there is a process for additional pore expansion (using an open circuit HF/DMSO etch), followed by surface functionalization with 1-dodecene at 120 °C.⁴⁸



Figure 11: Diagram show pSi pore expansion and functionalization. Adapted from Ref. 48.

Drug loading was accomplished using methanol as a solvent; with this method it is possible to obtain 50 mg of the drug for every gram of pSi. Drug release studies were carried out in phosphate-buffered saline (PBS) at pH 7.4 by monitoring using UV absorbance values associated with the drug at 242 nm. As observed in the release profile of Figure 12, non-

functionalized pSi releases all loaded drug in 1 hr, in contrast to 3 days with dodecene functionalization.⁴⁸

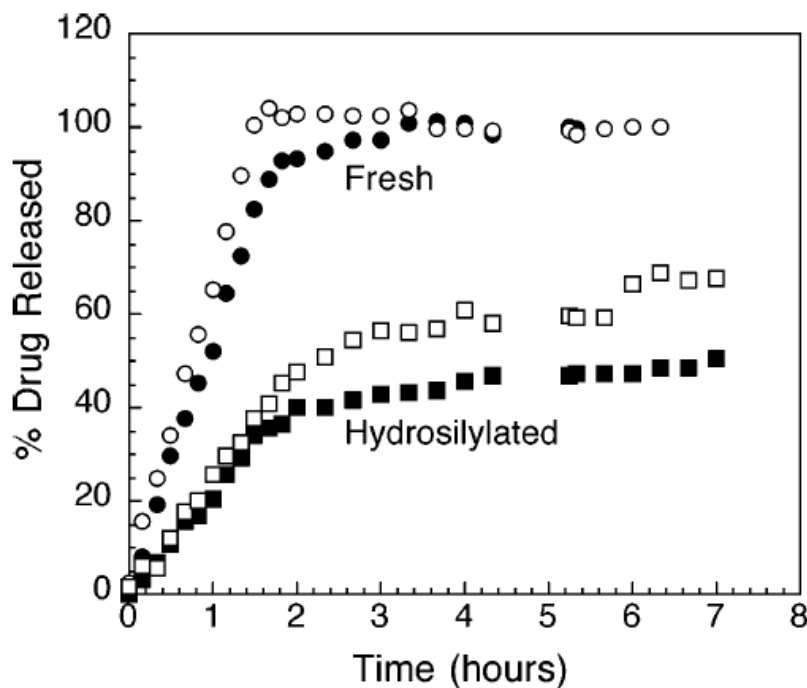


Figure 12: Release profile using pSi vs pSi functionalized with 1-dodecene. Adapted from Ref. 48.

1.4. Silicon Nanotubes (SiNTs)

An alternative Si nanostructure morphology worthy of consideration for a number of applications is Si NTs. Silicon nanotubes are nanostructures which contain a well-defined tube-like interior structure and elemental silicon shell. While early research focus on Si NTs has been in the area of battery storage and related energy applications,⁴⁹ Si NTs possess several fundamental properties that also make it of possible value in biomedical applications such as drug delivery.⁵⁰ These include a tunable inner and outer diameter, diverse surface functional groups, along with porous sidewall morphologies capable of nanoscale infiltration and

release.^{51,52} The nanotube form of elemental silicon remains less investigated, due primarily to the difficulties in its preparation. There are several methods reported in the literature with the goal of making SiNTs. These include: a) the filling of a porous alumina template;⁵³ b) the use of an arc plasma technique;⁵⁴ and c) employing zinc oxide nanowires (ZnO NWs) as a sacrificial template.⁵⁵ With an alumina template, it is easy to overfill the porous matrix, resulting in the formation of solid Si nanowires and thus a mixture of Si nanowires and Si NTs coexist in the final product. The arc plasma method produces a large number of Si nanoparticles, as the Si NTs are produced in small quantities. The most promising method is the use of ZnO nanowires as a sacrificial template; with this method we can control the characteristics of the Si NTs such as internal diameter and shell thickness.

1.4.1. Filling Alumina Templates

This method to produce SiNTs consists of a CVD process and porous alumina as a template; in this case Al₂O₃ possessing nanochannels (NCA) is used.⁵⁶ The first step to produce Si NTs by this route is the deposition of gold on the NCA using magnetic sputtering, and then silicon is deposited on the NCA in a quartz tube at low pressure using a mixture of argon-hydrogen-silane at 620 °C. Finally NCA is dissolved using a dilute solution of HCl.⁵⁶ With this method Si NTs are obtained based on the dimensions of the NCA template. The nanotube wall is polycrystalline with a silicon oxide surface. With this process Si NTs are often contaminated with phosphorous, chlorine and chromium due to the steps associated with NCA preparation. Another problem is the coexistence of Si NWs and Si NTs in the final product, as observed in TEM images of reaction products (Figure 13.)⁵⁶

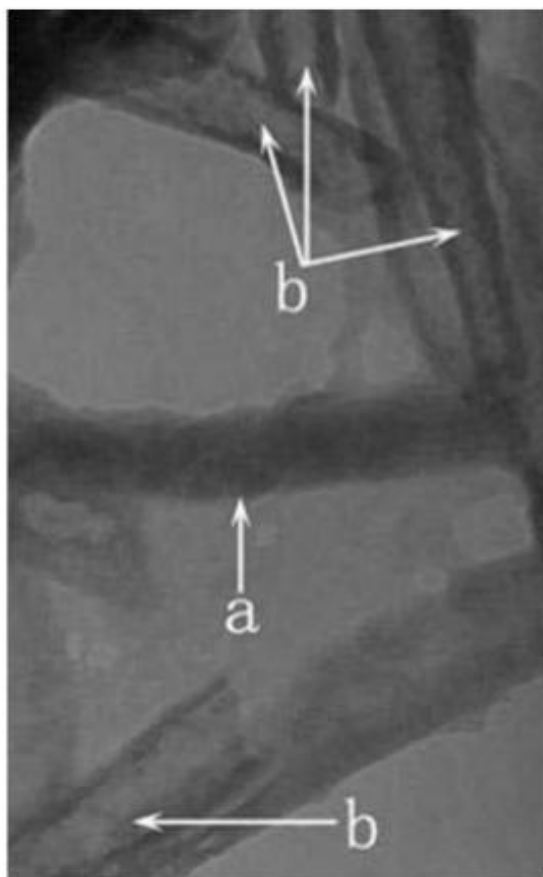


Figure 13: TEM morphology showing the coexistence of a) Si nanowires and b) Si nanotubes. Adapted from Ref. 56.

One way to explain the formation of Si NWs and Si NTs is through the diagram of Figure 14. When the gold is deposited on NCA, sometimes the gold is not deposited in an uniform way on the walls of the NCA; in some cases the gold is deposited in one end of the pore, and when this happens a solid Si NWs is formed. In Figure 14 (left), the gold catalyst (black dots) is deposited at one end of the pore. In the image on the right gold is evenly distributed along the NCA surface.⁵⁶

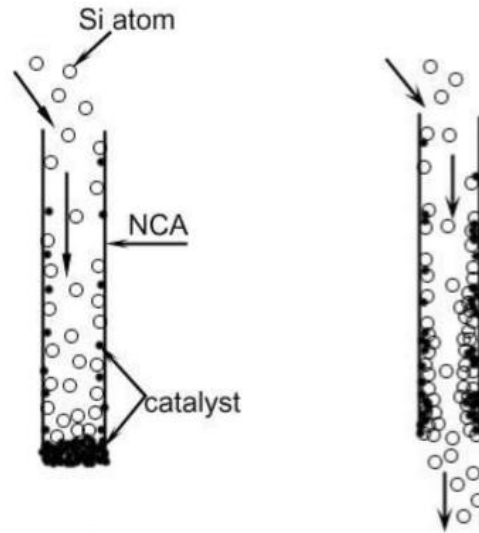


Figure 14: Mechanism to obtain Si nanowires and Si Nanotubes. Adapted from Ref. 56.

1.4.2. Arc discharge

This process consists of the creation of an arc current between two electrodes; one of the electrodes is made of silicon powder with a very high purity. The arc generated is about 30V and maintained at 75 Amps. In this process it is possible to produce gram quantities of material, with a nanotube length from hundreds of nanometers to a few microns and an average nanotube diameter around 7 nm. As we can observe in Figure 15, however, TEM images of a typical reaction product shows the coexistence of Si NTs and Si NPs clusters, with what appears to be a significant amount of spherical nanoparticles present.⁵⁴

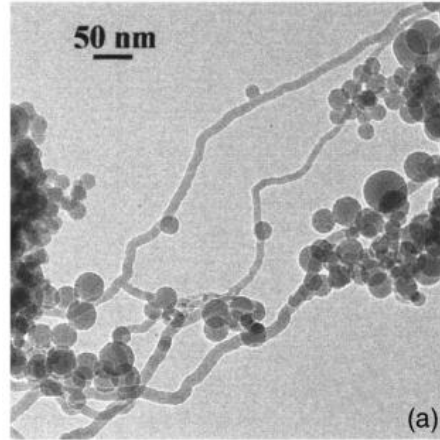


Figure 15: TEM of Si NTs produced by an arc-discharge technique. Adapted from Ref. 54.

1.4.3. Zinc Oxide Template

The key steps of this method consist of the use of ZnO nanowires as a template to produce nanotubes and remove them by a selective etch process. The first reported use of this method is the production of GaN nanotubes by Yang and co-workers.⁵⁵ As observed in Figure 16 there are three main steps to obtain GaN nanotubes. The first step consists in the growth of ZnO on sapphire using a vapor deposition technique. Then GaN is deposited using CVD with trimethylgallium and ammonia as precursors in Argon gas at 600 °C. Finally ZnO is removed using hydrogen (H₂) in Argon at 600 °C. This method can produce GaN nanotubes with a 5-50 nm wall thickness and 30-200 nm diameter. It is also interesting to note that the nanotubes produced by this method have one end open and retain the same morphology as the ZnO nanowire template.⁵⁵

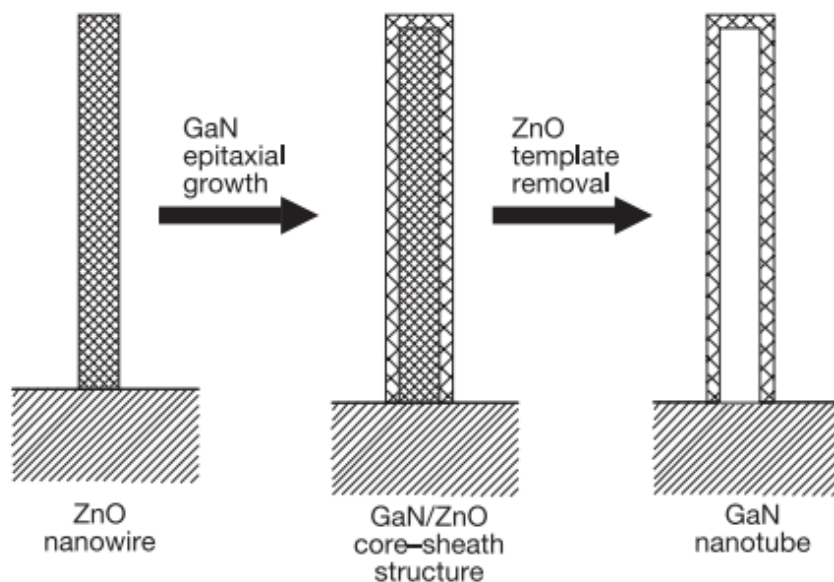


Figure 16: Process to produce GaN nanotubes. Adapted from Ref. 55.

In order to verify the presence of a tubular structure and total ZnO removal from the core, TEM imaging with elemental analysis (EDX) in line scan mode can be used (Figure 17). One can observe after GaN deposition, a strong Zn signal appearing in the middle of a double hump Ga signal. After ZnO etching, the Zn signal disappears, leaving only a Ga signal. With this method, it is possible to produce tubular structures of monocrystalline GaN.⁵⁵

This process developed by Yang and coworkers established a new approach for the formation of other hollow inorganic nanotube materials.⁵⁵

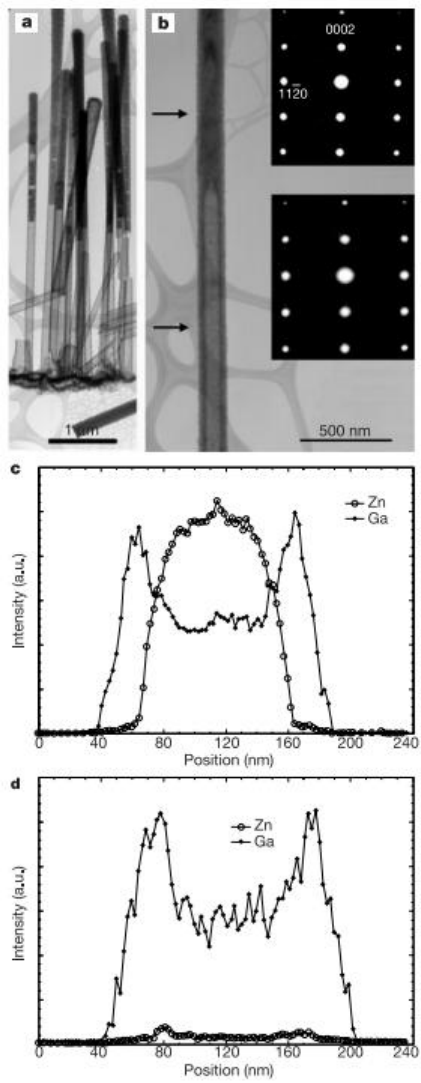


Figure 17: Characterization by TEM and EDX of GaN/ZnO core shell and GaN nanotubes. Adapted from Ref. 55.

Chapter II

Silicon Nanotubes Fabrication

2.1. Introduction

In Chapter I, an overview of currently-available methods for Si NTs fabrication was presented. Based on the advantages and disadvantages associated with those methods, it appears that the use of ZnO as a template, followed by Si deposition and ZnO etch steps, is the most promising method for uniform SiNT preparation.

Si NTs have an advantage over other Si-based nanomaterials such as porous silicon due to the fact that such nanotubes have, in principle, a more well-defined nanostructure orientation and Si thickness. In this chapter, optimization of the parameters in this sacrificial templating method for Si NT fabrication is described, including control of shell thickness, inner diameter, and nanotube length. It should be pointed out here that some initial experiments in Si NT fabrication were carried out by a former group member, Xuezhen Huang. In Figure 18, the different steps to produce Si NTs are illustrated for the sacrificial ZnO template method. In this technique, Si NT inner diameter is controlled by ZnO diameter, nanotube length by ZnO nanowire length, and nanotube shell thickness is controlled by silane concentration/duration of exposure.

In addition to an investigation of the control of SiNT shell thickness, inner diameter, and length, a series of experiments describing the impact of nanotube shell thickness on Si dissolution in aqueous media is also described in this chapter. Such assays are a significant component of evaluating these nanotube platforms for possible use as a biomaterial.

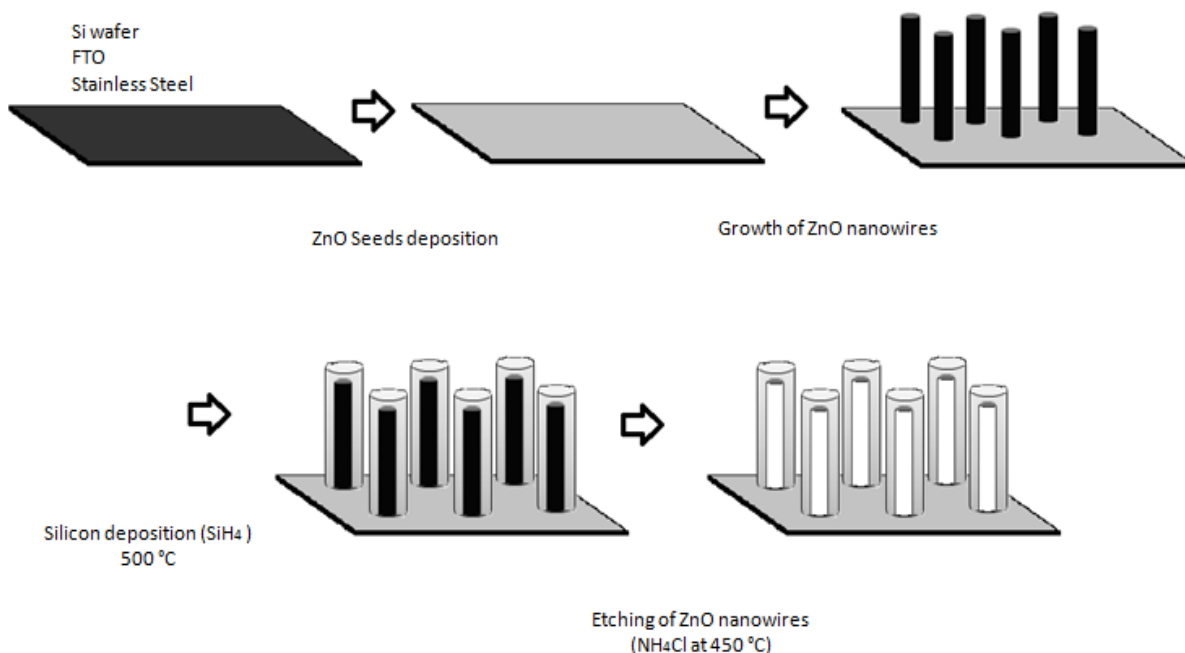


Figure 18. Si NTs fabrication steps.

2.2. Experimental

2.2.1. Substrate preparation

The first step in the process involves cleaning a given substrate, selected from either FTO glass (TEC-15, MTI Co.), Si wafer pieces, or stainless steel. Typical substrate sample size is 1.2 cm x 1.5 cm. The FTO surfaces were cleaned with 10% HCl for 30 min, followed by sonication for 1 hr in acetone. The Si wafer pieces were cleaned with piranha solution (70 % sulfuric acid and 30 % hydrogen peroxide) at 60 °C for 30 min, also followed by sonication for 1 hr in acetone, and blow-drying with N₂. The stainless steel was cleaned by 1 hr of sonication in acetone and blow-drying with N₂.

2.2.2. ZnO nanocrystal seed preparation

ZnO nanocrystal seeds (for subsequent ZnO NW growth) were prepared by mixing solutions of 0.01 M zinc acetate (in methanol) and 0.03M NaOH (also in methanol) (4:1 V:V) at 60°C with constant stirring for 2 hr. Layers of ZnO nanocrystals were deposited on a given substrate by spin coating. In this process, several drops of ZnO nanocrystal seed solution were placed on top of a given substrate, followed by spin coating at 3000 rpm for 1 min, followed by annealing at 300 °C for 30 min. The process is repeated at least 3 times.

2.2.3. ZnO nanowire array fabrication.

ZnO NWA templates were prepared on a given substrate (FTO, Si, or stainless steel) that were previously seeded with ZnO nanocrystals (according to the above procedure) by placing in a mixture (1:1 v:v) of 0.03 M $\text{Zn}(\text{NO}_3)_2$ and 0.03 M hexamethylenetetramine at 92°C for 9h. For selected experiments, polyethylenimine (100 ul, branched, low molecular weight, Aldrich) was added into 100 ml of ZnO growth solution to restrict ZnO NW width. The solution is replaced every 3 hrs to keep precursor concentrations high. Under these conditions, the length of ZnO nanowire is about 2 μm , with an average diameter of 80 nm (40 nm in the presence of PEI).

2.2.4. Si deposition by Chemical Vapor Deposition (CVD)

A ZnO NW array sample was inserted into a quartz tube reactor, and Si deposition on the ZnO NWA was achieved through the use of silane (20 sccm, 0.5% in He, Praxair) mixed with He carrier gas (200 sccm, UHP grade, Praxair) that was passed through a furnace operating at 520-600 °C for 5-10 min.

2.2.5. ZnO etching / template removal

These Si-coated ZnO NW samples were then placed in another quartz reactor and heated to 450 °C; NH₄Cl was loaded in an alumina boat located upstream and heated to 350 °C. The gaseous etchant was transported via He gas downstream (170 sccm) to the furnace for 1 hr for removal of the ZnO NWA substrate. A secondary annealing at 600 °C for 2 hrs can be used to increase the crystallinity of Si NTs, if desired.

2.2.6. Silica dissolution assay

A silicomolybdic acid spectrophotometric method was utilized to measure the relative extent of SiNT dissolution in aqueous media.⁵⁷ Such a method is based on the ability of silicic acid to form a heteropolyacid, silico-12-molybdic acid, in the presence of acidified ammonium heptamolybdate, according to the following equation:⁵⁷



The resulting silicomolybdic acid is a yellow compound. The blue color is obtained from the reduction step; it is stable for several hours.^{58,59}

The samples were selected based on nanotube shell thickness (10, 34 and 80 nm). The dissolution assay was tested in PBS at 37 °C and in some cases, DI water at room temperature. In a typical assay, 0.5 ml of the sample of interest from a given time point is mixed with 4.5 ml of DI water, followed by addition of 3 ml of HCl acid (0.25 M) and 1 ml of ammonium molybdate (5%). 10 minutes later 2 ml of sulfuric acid (50 %) and 1 ml of oxalic acid (1 %) is added. Finally, 10 min later, 10 ml of sodium sulfite 17% is added to this mixture, and the solution is

allowed to stand overnight. The concentration of silicic acid bound to the molybdate species is monitored by the value of its absorbance at 700 nm (via UV-VIS spectroscopy), in conjunction with a standard curve generated from a series of silica standards. After each measurement, the remaining solid Si sample is immersed in fresh PBS for additional measurements.

2.3. Results and Discussion

2.3.1. Growth of ZnO NW array templates

Si NTs can be controlled in terms of inner diameter, shell thickness, and length. The hollow inner diameter of a given nanotube is dependent on the initial ZnO NW diameter. Typical growth conditions produce a dense uniform array of ZnO NWs on a given substrate (Fig 19a). The ZnO NW diameter can ideally be controlled with the concentration of the Zn^{2+} and O^{2-} precursors in the growth solution and reaction time. For a given set of reactant concentrations, the diameter can also be reduced with the addition of polyethylenimine (PEI); PEI moieties are selectively adsorbed on the lateral sidewall crystal facets (1010) of ZnO nanowires by electrostatic attraction.⁶⁰ For example, as shown in Fig 20b, ZnO NWs mean diameter changes from 60 nm to 40 nm with the addition of PEI after 9 hrs in the growth solution. In the absence of PEI, the distribution is more broad and the ZnO NW growth more rapid relative to that when PEI is present.

The data presented in Table 1 confirm the expectation that in general, longer reaction times and higher reactant concentrations lead to larger diameter ZnO NWs as well as an increased length.

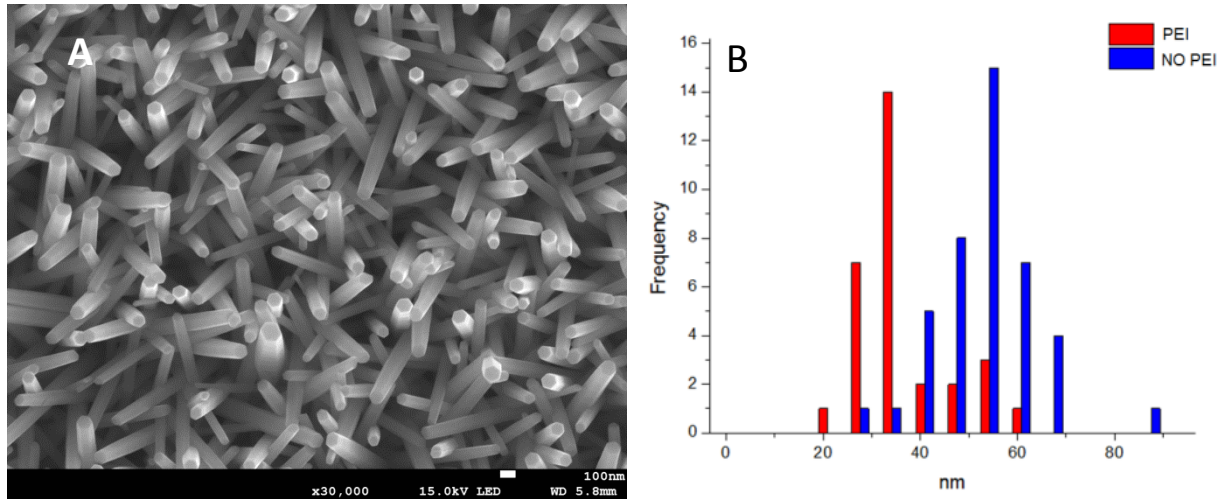


Figure 19. a) SEM image of a ZnO NW array on Si substrate. b) Histogram illustrating the role of PEI on ZnO NW diameter. The average ZnO NW with is 38 nm with PEI and 60 nm without PEI.

Table 1. ZnO NW template diameter and length as a function of concentration, reaction time, and presence/absence of PEI.

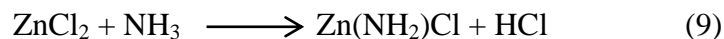
| Concentration | | Diameter (nm) | | Length (nm) |
|---------------|-------|---------------|---------------|------------------|
| 0.08 M | 3 hs | NO PEI | 71.24 ± 16.53 | ----- |
| 0.08 M | 1 hr | NO PEI | 35.95 ± 7.45 | ----- |
| 0.04 M | 9 hrs | NO PEI | 61.07 ± 12.91 | 2072 ± 363 |
| 0.02 M | 9 hrs | NO PEI | 63.06 ± 14.54 | 1771 ± 338 |
| 0.02 M | 9 hrs | PEI | 46.53 ± 8.48 | 2208 ± 147 |
| 0.02 M | 3 hrs | NO PEI | 38.86 ± 6.73 | ----- |
| 0.02 M | 3 hrs | PEI | 29.92 ± 4.83 | 1109 ± 311 |
| 0.01 M | 3 hrs | NO PEI | 30.77 ± 6.63 | NW ≤ 2 μm |
| 0.01 M | 3 hrs | PEI | 25.58 ± 5.96 | ----- |
| 0.005 M | 3 hrs | NO PEI | 21.89 ± 3.65 | 1 μm ≥ NW ≤ 2 μm |
| 0.005 M | 3 hrs | PEI | 33.04 ± 9.87 | ----- |
| 0.04 M | 1 hr | NO PEI | 27.56 ± 4.20 | NW ≥ 1 μm |
| 0.04 M | 1 hr | PEI | 25.50 ± 5.30 | ----- |
| 0.02 M | 1 hr | NO PEI | 20.47 ± 3.17 | ----- |
| 0.01 M | 1 hr | NO PEI | 22.20 ± 4.16 | NW ≤ 1 μm |

The plus/minus values in the above stated diameter and length refer to measured standard deviation of each parameter.

2.3.2. Si Deposition and etching of ZnO NWs.

Chemical vapor deposition (CVD) is used to add the Si component for subsequent nanotube formation. Specifically, silane (150 sccm, 0.5% in He, further diluted in He at 150 sccm) is used to form a Si coating (500 °C) on the surface of the ZnO NWs, with the thickness of the Si shell controlled by the duration of the silane exposure (6–10 min), or alternatively, local Si concentration as a function of sample location in the reactor.

Etching of ZnO can be done with the generation of HCl gas using as a precursor NH₄Cl at relatively low temperatures (around 480 °C). The ZnO core is converted into liquid ZnCl₂ (m.p. 292 °C) at 540 °C in the reaction. While ZnCl₂ can be removed by an evaporation process, the formation of a zinc amide species and its favorable vapor pressure at the temperatures utilized assists in the efficiency of the process.⁶¹ For nanotubes above 40 nm in wall thickness it is necessary to undertake a second or third etching process to completely remove the ZnO. We can observe in figure 21, Si NTs of 60 nm we need a second etching process to remove all ZnO in the core, this is due to the difficulty of the etchant gas to reach the ZnO core. One proof of the removal of zinc oxide during the etching process is the use of energy dispersive x-ray element analysis (EDX) in the SEM. After etching, the Zn signal disappears in a typical EDX spectrum, with the only signal remaining is the Si peak (for Si NTs on a silicon wafer substrate; Figure 20). The mechanism in which the ZnO is removed is shown in the following reaction.⁶¹



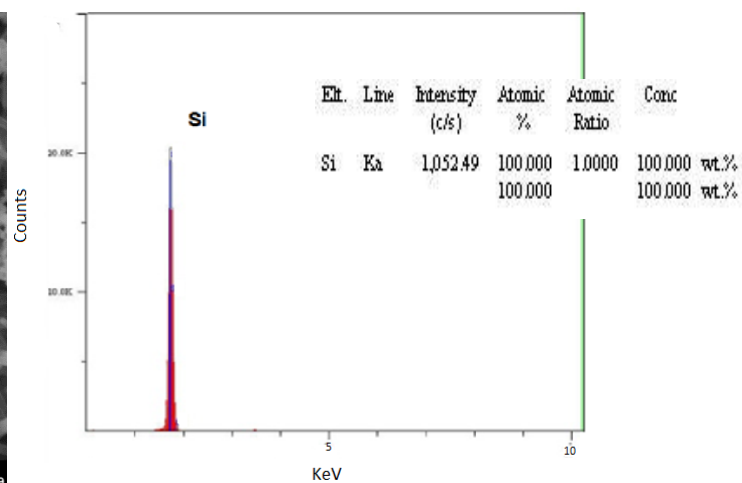
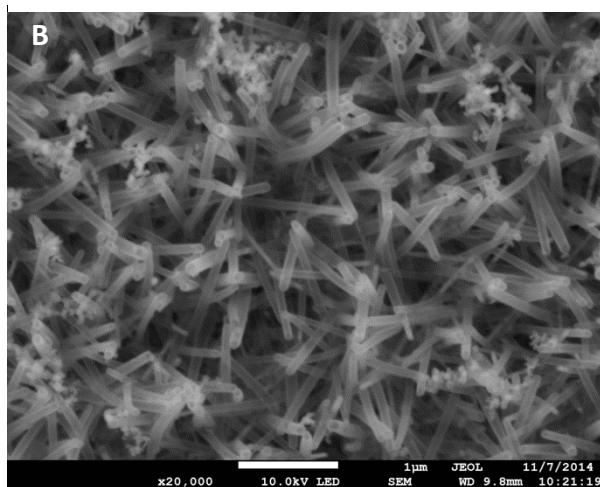
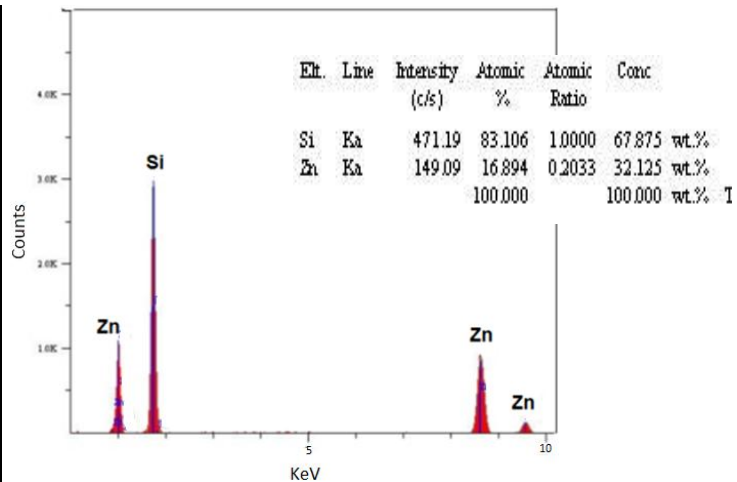
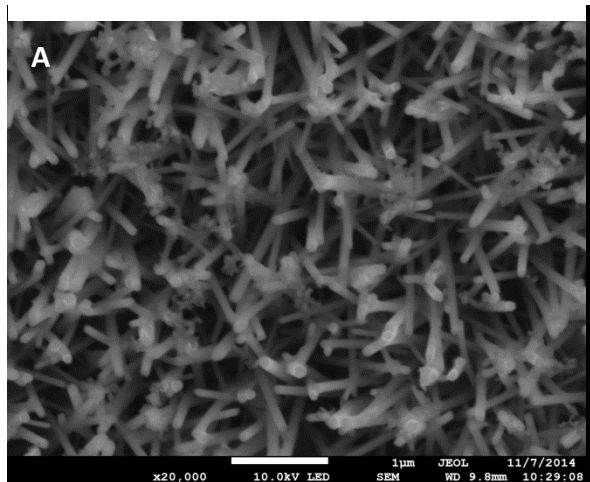


Figure 20. SEM and EDX of etched Si/ZnO NW samples with 10 nm Si shell thickness: a) Si Shell/ZnO core NW before etching; b) Si NTs formed after etching.

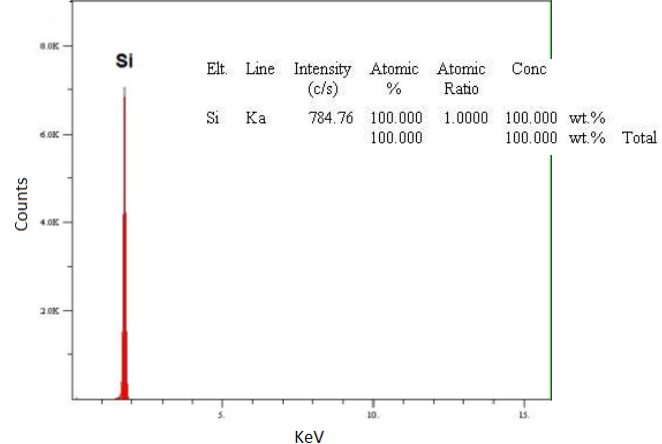
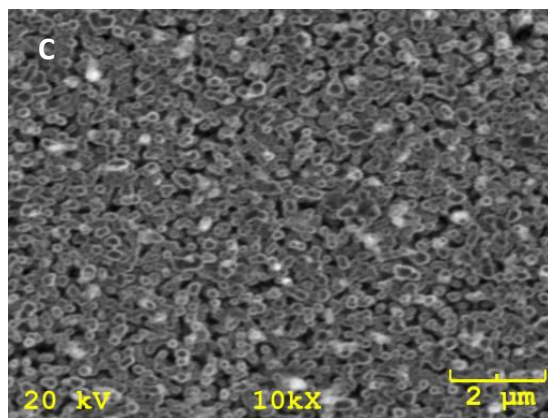
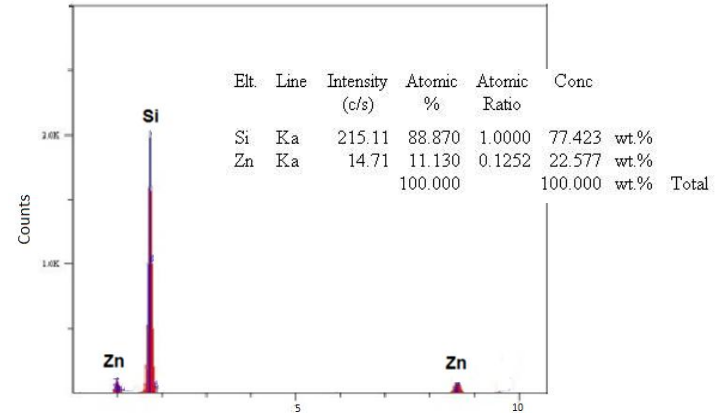
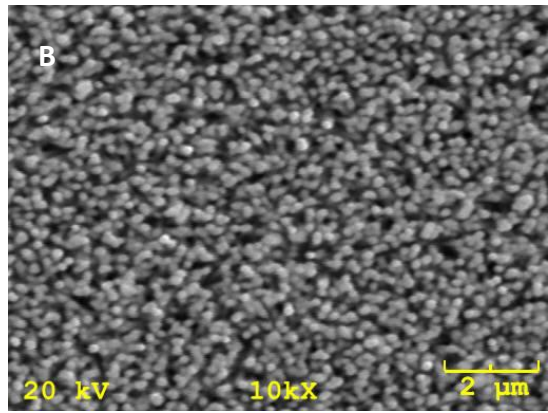
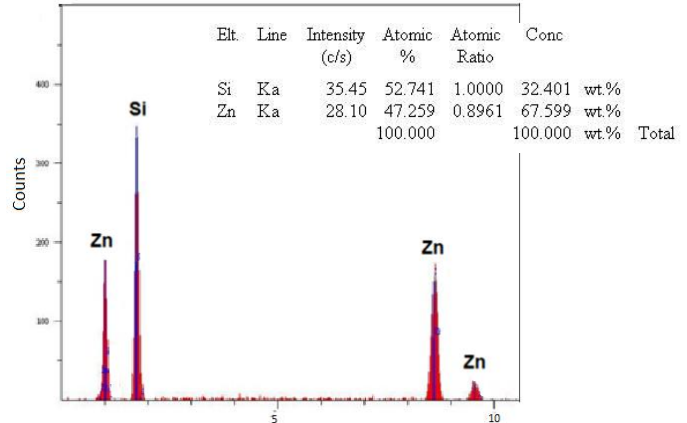
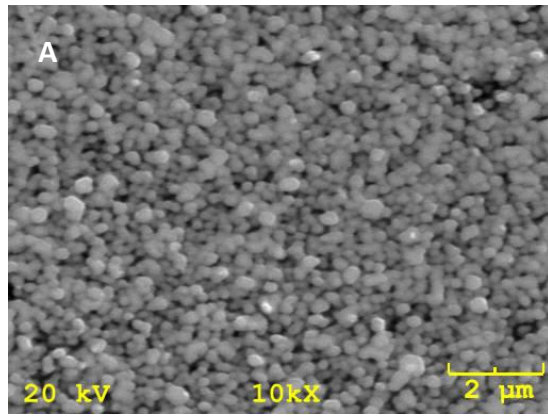


Figure 21. SEM and EDX of samples etched Si/ZnO NW with 60 nm Shell thickness: a) Si Shell, ZnO core NW before etching; b) Si NTs after 1st etching; c) Si NTs formed after 2nd etching.

As pointed out above, the nanotube shell thickness, ranging from 10 nm to 80 nm, is dependent upon the position of the substrate (FTO, Stainless Steel or Si wafer) in the reactor, the duration of reaction, and temperature. Si NTs can be classified into three main categories based on the wall thickness: thin, mid-range, and thick (Figure 23). For a given reaction time and substrate position in the reactor, we find it is most convenient to direct control of Si NTs wall thickness with temperature. With increasing reaction temperature, the Si NTs shell becomes thicker (Fig. 24b). For a given process in the reactors used, temperature it was recorded in the center of the reactor, with the origin of the x-axis taken as the point closest to the furnace opening containing the He stream (Fig. 24a).

In Figure 24a,b, for the SiNTs with a very thin 10 nm wall thickness, porous features are observed. Proof of this porosity can be verified by the infiltration of luminescent dyes such as tris(bipyridyl) ruthenium(II), or alternatively magnetic nanoparticles. The infiltration of magnetic nanoparticles into these nanotubes is discussed in detail in Chapter 4.

For the case of tris(bipyridyl) ruthenium(II), a typical experiment involves the exposure of a given porous Si NT film to a dilute ethanolic solution of $\text{Ru}(\text{bpy})_3^{2+}$, followed by ethanol rinse and air drying. Such films produce strong visible light that can be viewed via confocal fluorescence microscopy (Fig 22a); in this image, the size of the luminescent domains are consistent with the overall widths of a given nanotube. Importantly, measurements of the lifetime of this fluorescence can provide useful information about the local environment of the adsorbed species. These additional experiments were carried out in the laboratory of Professor Zygmunt Gryczynski and Ryan Rich in TCU Physics Department. It was determined that for $\text{Ru}(\text{bpy})_3^{2+}$ loaded into Si NTs, the expected two decay regimes are observed with τ_1 of 10 ns and τ_2 450ns.⁵² Thin films of crystalline $\text{Ru}(\text{bpy})_3^{2+}$ ranging from 17 nm to 200 are reported to exhibit two

components: a relatively fast τ_1 of 80-99 ns and a longer τ_2 component of 329-400 ns, associated with two pathways for energy transfer associated with the excited state (molecule/surface and molecule/air).⁶³ The reduction that we observe in τ_1 in our system is presumably because electron transfer between the $\text{Ru}(\text{bpy})_3^{2+}$ and the native oxide of this semiconductor; it is also consistent with previous studies of adsorption of $\text{Ru}(\text{bpy})_3^{2+}$ onto oxide-terminated semiconducting surfaces.⁶² These results are also consistent with the absorption of $\text{Ru}(\text{bpy})_3^{2+}$ into the porous wall of the Si NTs. In Table 2, we compare lifetimes of $\text{Ru}(\text{bpy})_3^{2+}$ adsorbed onto SiNTs with previously reported values for this complex in crystalline thin film form as well as adsorbed onto types of surfaces. Accurate determination of the uncertainty in our measurements are not possible, but is assumed to be no more than 10%. Therefore the slight lengthening of the longer lifetime component (τ_2) is not assumed to be significant.

Table 2. τ_1 and τ_2 for films of $\text{Ru}(\text{bpy})_3^{2+}$, $\text{Ru}(\text{bpy})_3^{2+}$ adsorbed onto selected oxide surfaces, and $\text{Ru}(\text{bpy})_3^{2+}$ adsorbed onto SiNTs.

| Substrate | τ_1 (ns) | τ_2 (ns) |
|---|-----------------|------------------|
| $\text{Ru}(\text{bpy})_3^{2+}$ film ⁶³ | 80-99 | 329-400 |
| $\text{Ru}(\text{bpy})_3^{2+}$ adsorbed on SiO_2 ⁶² | 50 (\pm 10%) | 420 (\pm 10%) |
| $\text{Ru}(\text{bpy})_3^{2+}$ adsorbed on TiO_2 ⁶² | 18 (\pm 10%) | 64 (\pm 10%) |
| Si NTs on $\text{Ru}(\text{bpy})_3^{2+}$ | 10 (\pm 10%) | 450 (\pm 10%) |

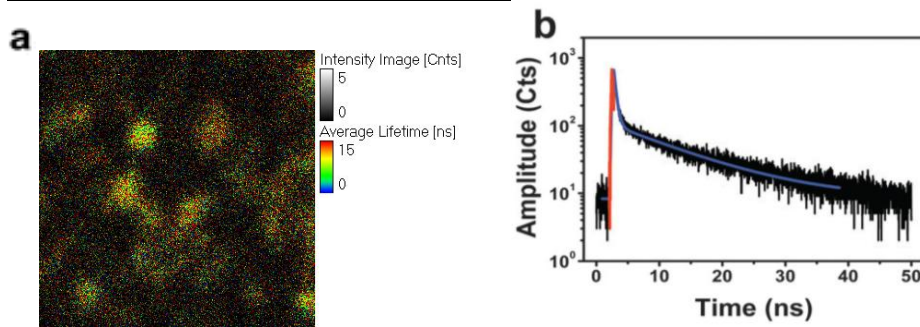


Figure 22. a) Confocal fluorescence microscopy image of a Si NT array infiltrated with $\text{Ru}(\text{bpy})_3^{2+}$; $\lambda_{\text{ex}} = 470$ nm; field of view = 5×5 μm . b) Corresponding fluorescence decay curve and associated residual analysis of the two exponential fit of the decay curve. The black trace is the collected data, the red trace is the instrument response function calculated by the software, and the blue trace is the exponential decay fit. Adapted from Ref. 52.

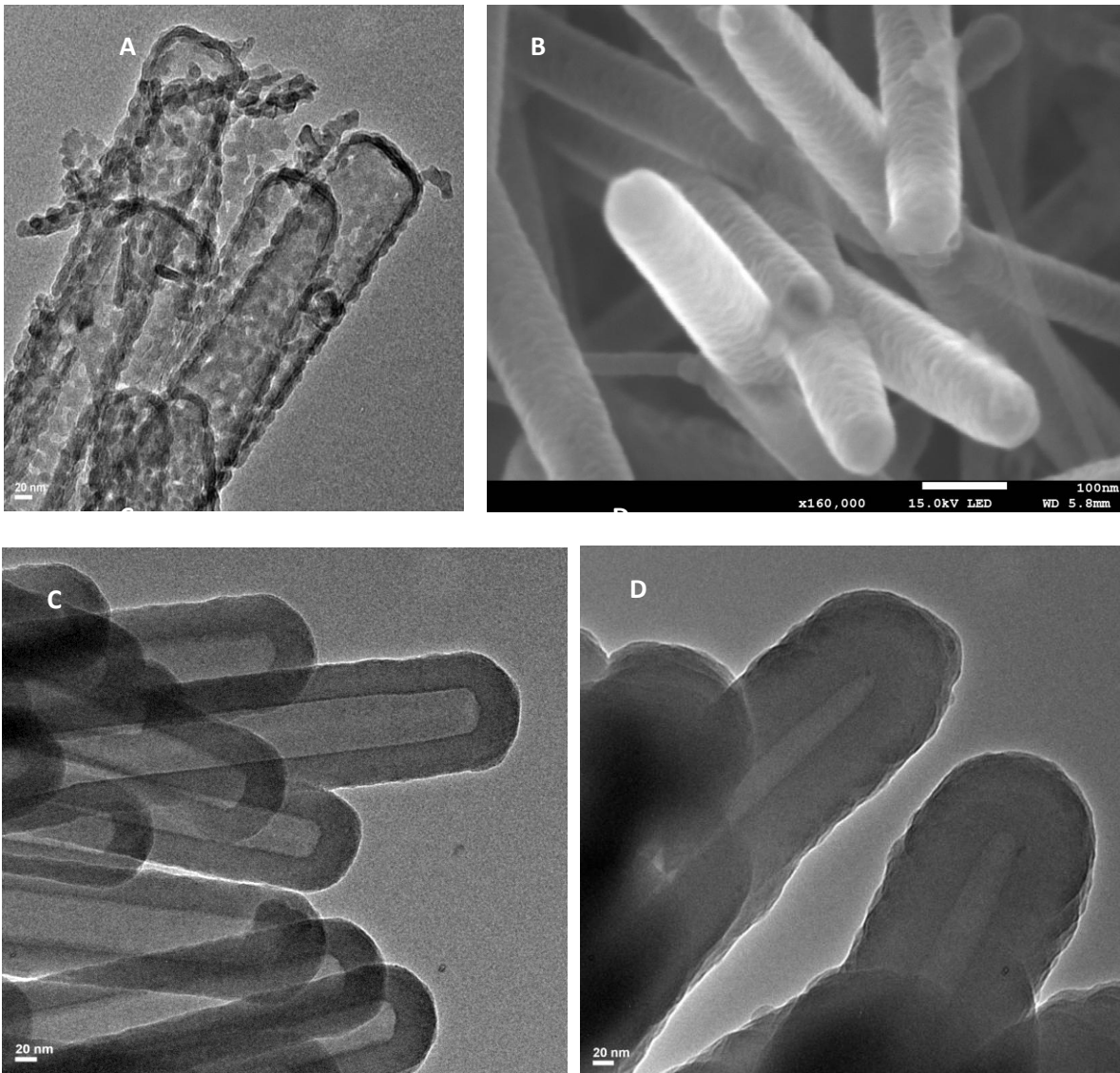


Figure 23. Different wall thickness of silicon nanotubes. a) TEM of 10 nm wall thickness. B) SEM of 10 nm wall thickness. c) TEM of 39 nm wall thickness. d) TEM of 79 nm wall thickness.

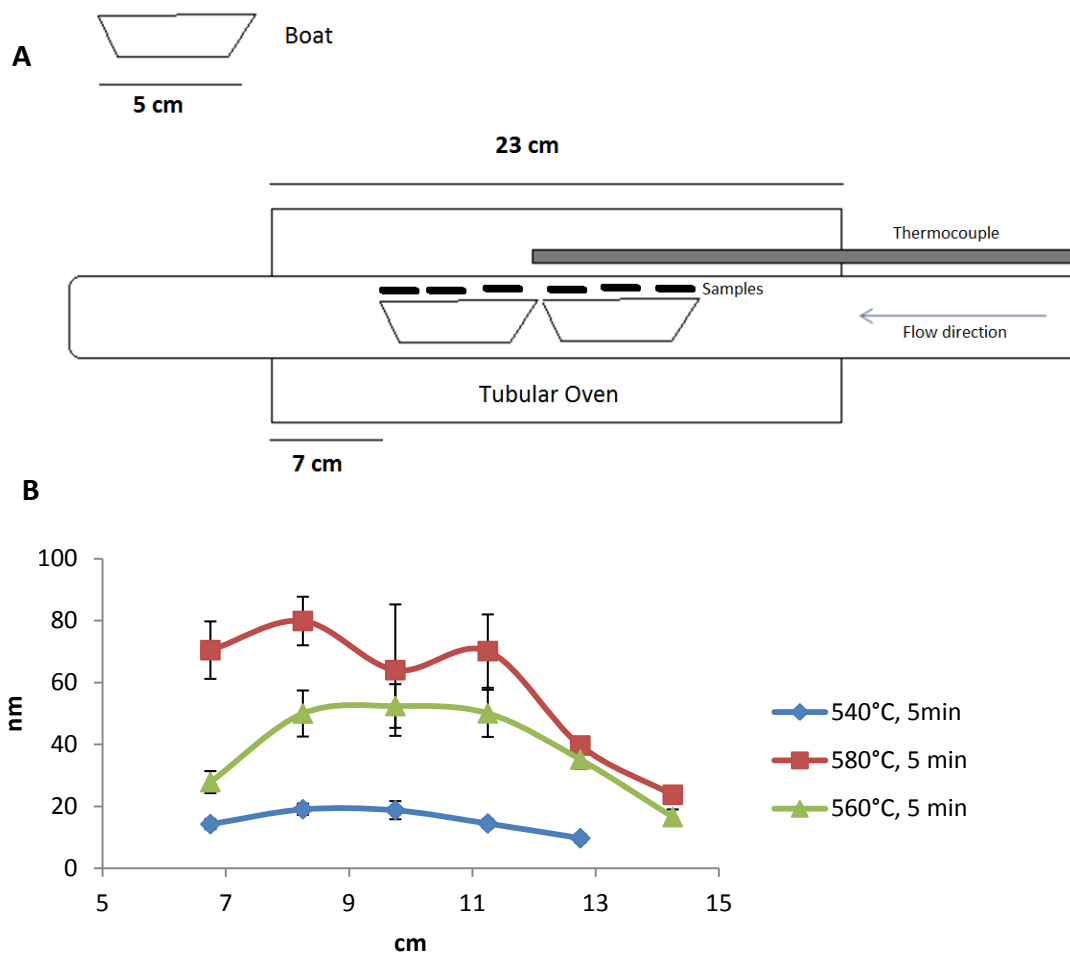


Figure 24. a) Silicon deposition system. b) Characterization of Si NTs wall thickness as a function of substrate location in the reactor. The measured distance is relative to the edge of the oven closest to the opening containing the He stream.

Structurally, after the Si deposition on ZnO and subsequent etching steps, the film is amorphous as observed in Fig 25a. A secondary annealing at 650°C for 30 min in a He atmosphere produces nanocrystalline domains of (111) orientation in the Si NTs with d spacing of 0.31nm. Figure 25b shows a typical HRTEM image of the crystal planes present in the Si NT; Fig 25b presents the Fast Fourier Transform (FFT) image, reflecting the electron diffraction pattern associated with this image.⁶⁴ Multiple spots indicative of a polycrystalline pattern are evident.

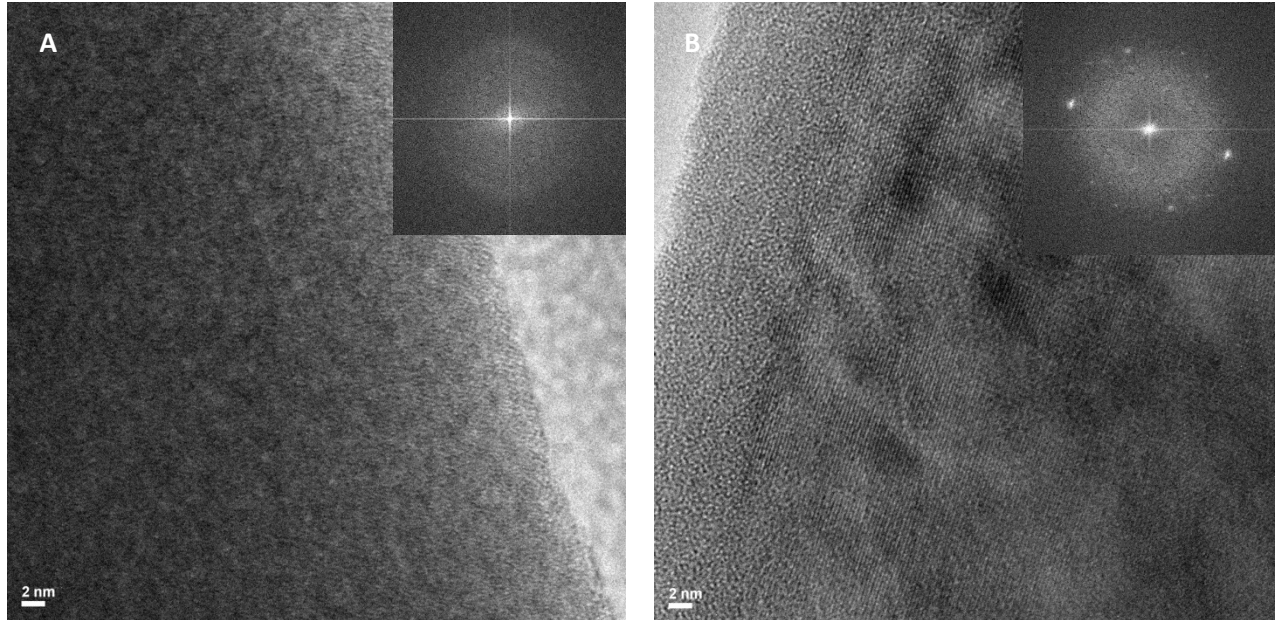


Figure 25. a) HR-TEM of unannealed SiNT and FFT associated with the HR-TEM image (inset). b) HR-TEM of Si NT after the annealing process and FFT associated with the HR-TEM image (inset).

2.3.3. Dissolution Assays of Si NTs

For applications in biomedicine such as drug delivery and tissue engineering, the degradability of these Si NTs is important. Figure 26 shows that annealed at 650°C in Helium, Si NTs dissolve very slowly, almost negligibly, compared with the non-annealed Si NTs under the same conditions (PBS at 37 °C). The behavior of the annealed sample is similar to the sample in water at room temperature. Si NTs with smaller shell thicknesses dissolve faster than the thicker ones; this is due presumably to the higher surface area and exposed curved reactive surfaces of the nanocrystalline domains of these SiNTs (Figure 27).

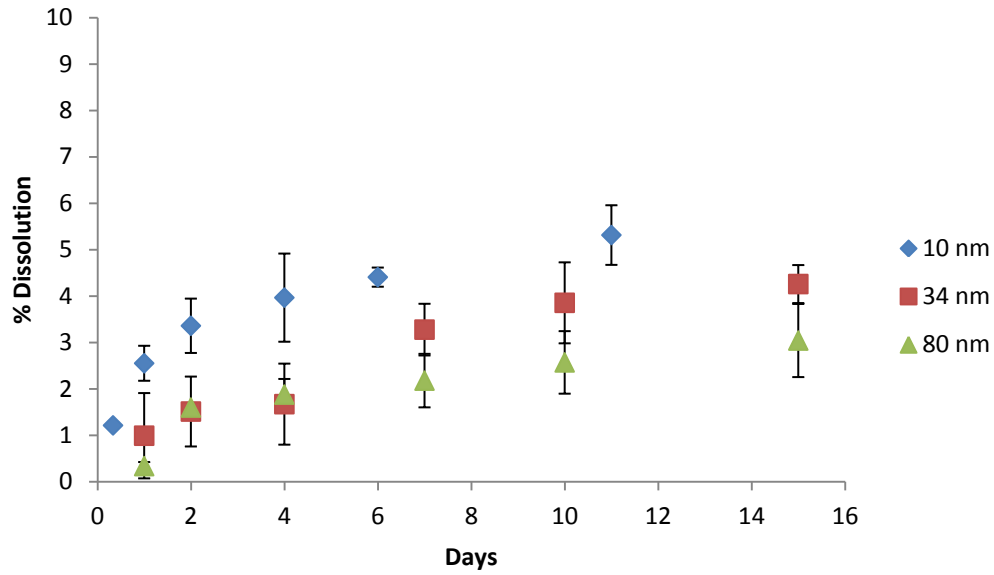


Figure 26. Dissolution of three different wall thickness Si NTs in PBS at 37 °C.

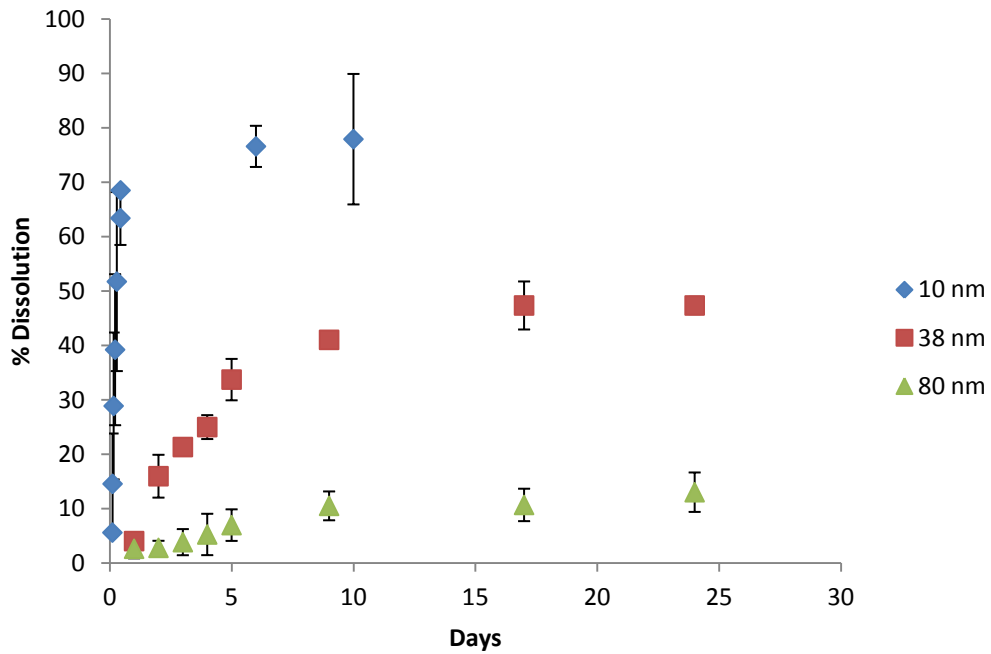


Figure 27. Dissolution of three different wall thickness Si NTs in PBS at 37 °C. Not annealed Samples.

This tunable dissolution behavior as a function of wall thickness, or alternatively, sample annealing, provides a window for possible therapeutic use as a drug carrier in future applications, depending on the ultimate therapeutic need.

2.4. Summary

In this section, details of the Si NTs fabrication process were presented, including a demonstration of the ability to control the wall thickness in Si NTs, inner diameter and length. Also, an ability to create different SINT morphology types, such as those possessing a porous sidewall in the case of 10 nm Si NTs, was presented. Such porous morphology can lead to the infiltration of selected small molecules such as dyes. In addition, a property with implications for biomedical applications, specifically dissolution behavior, was presented. In subsequent chapters, the applications of these different nanotubes will be addressed.

Chapter III

Silicon Nanotubes and Applications in Lithium Ion Batteries

3.1. Introduction

Batteries can store energy by a difference in chemical potential, with the energy in these electrochemical storage devices used when necessary.⁶⁵ Batteries have applications in electric vehicles, phones, computers, a number of home and healthcare-related devices. For these reasons, multiple battery systems have been developed: Lead-acid, Ni-Metal hydride, Ni-Cd, and Lithium Ion Batteries (LIB).⁶⁶ Lithium batteries are one of the most studied at present, due mainly to their excellent electrochemical performance in the form of low self-discharge, high energy density and long cycle life.⁶⁷ As observed in Figure 28 in a comparison of power and energy density for different battery systems, it appears that LIBs are superior to other present options.⁶⁸

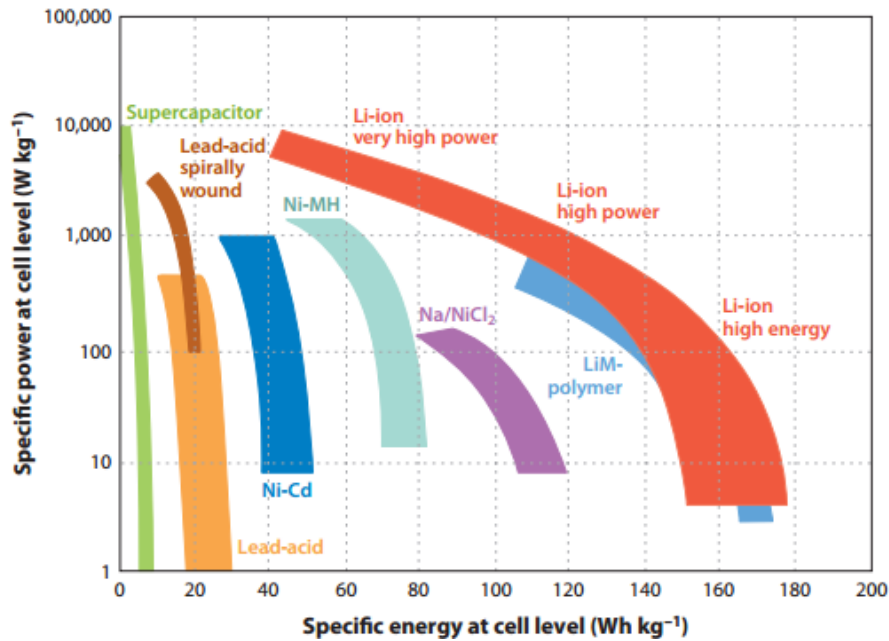


Figure 28: A comparison of energy and power densities of common rechargeable batteries. Adapted from Ref. 68.

The basic structure of a battery contains three elements: (a) cathode (positive), (b) anode (negative), and (c) electrolyte; these are illustrated in Figure 29.⁶⁹

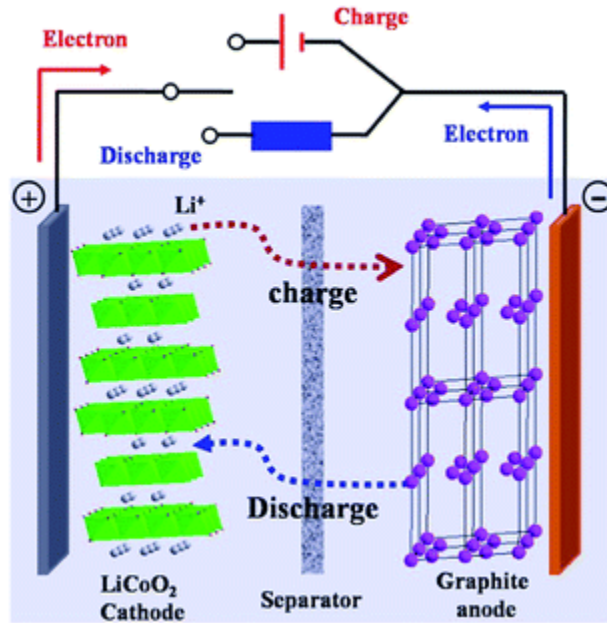


Figure 29: Basic structure of a Lithium Ion Battery. Adapted from Ref. 69.

The necessary redox reactions occurring in a battery can be expressed by the following series of reactions (for the case of a lithium cobalt oxide-based system):



where C is graphite, LiCoO₂ is the cathode, Li⁺ is the electrolyte.⁷⁰

In this chapter, a number of specialized terms relevant to electrochemical cells and batteries are mentioned frequently; therefore it is useful to provide some basic definitions at the outset:

Capacity - The capacity of a battery is a measure of the amount of energy that it can deliver in a single discharge. Battery capacity is normally listed as amp-hours (or milli amp-hours) or as watt-hours.⁷¹

C - Used to signify a charge or discharge rate equal to the capacity of a battery divided by 1 hour. Thus C for a 1600 mAh battery would be 1.6 A; C/5 for the same battery would be 320 mA and C/10 would be 160 mA. Because C is dependent on the capacity of a battery the C rate for batteries of different capacities must also be different.⁷¹

SEI – Solid Electrolyte Interfaces. SEI intrinsically consumes the anode and electrolyte, leading to a low efficiency.⁷¹

Galvanostatic - refers to an experimental technique whereby an electrode is maintained at a constant current in an electrolyte. This technique is used to measure corrosion rate and electrochemical reactions.⁷¹

Coulombic Efficiency: The ratio of the output of charge by a battery to the input of charge. Coulombic efficiency is determined by the internal resistance of a cell.⁷¹

3.1.1. Separator and Electrolyte

The electrodes are physically separated by an electrolyte and a separator. The separator is a membrane used to inhibit contact between the cathode and anode, with the most common membrane materials being fiberglass and polyethylene oxide.⁷² Common electrolyte selections include LiPF_6 , LiBF_4 , LiClO_4 , and LiBC_4O_8 .⁷³ These electrolytes are dissolved in solvents with high electronic and ionic conductivity, such as ethylene carbonate (EC), dimethyl carbonate (DMC), diethyl carbonate (DEC) and ethyl methyl carbonate (EMC).⁷⁴

3.1.2. Cathode Materials

There are three main materials used as cathodes for LIB; those materials are: layered structures such as LiMO_2 or Li_2MnO_3 ($\text{M} = \text{Ni}, \text{Co}, \text{Mn}$); spinel compounds LiM_2O_4 ($\text{M} = \text{Mn}$, etc.); and olivine compounds LiMPO_4 ($\text{M} = \text{Fe}, \text{Mn}, \text{Ni}, \text{Co}$).⁷⁵ The corresponding crystal structures are illustrated in Figure 30.⁷⁶ Figure 31 provides a comparison of cell potential versus gravimetric capacity for these materials; selection of a given material depends on the target application: olivine-type compounds are selected mainly for high voltage applications, while layered structures and spinels are chosen principally for low voltage uses but with very high capacity.⁷⁷

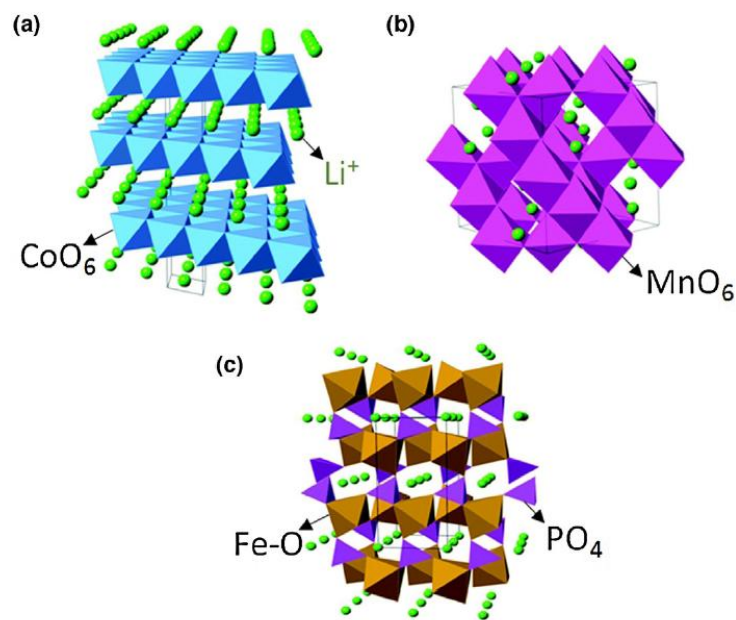


Figure 30: Crystal structures of representative intercalation cathodes: structure of (a) layered (LiCoO_2), (b) spinel (LiMn_2O_4), (c) olivine (LiFePO_4). Adapted from Ref. 76.

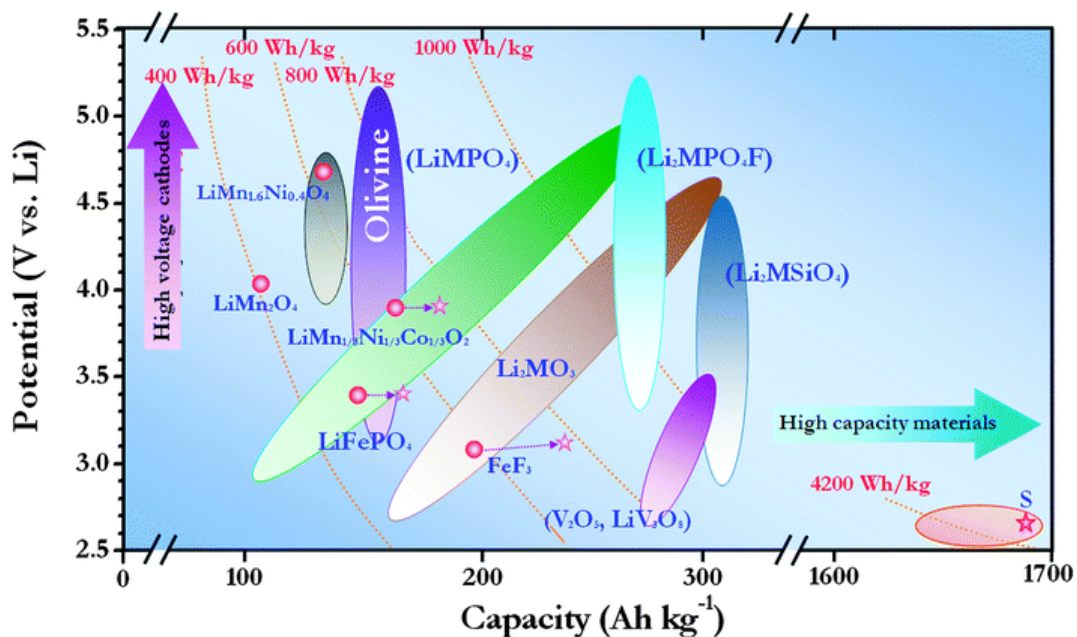


Figure 31: Schematic representation of the plot of Li-ion battery cathode material potentials vs. capacity. LiMPO_4 , Li_2MSiO_4 and $\text{Li}_2\text{MPO}_4\text{F}$, where $\text{M} = \text{Fe}, \text{Mn}, \text{Co}, \text{Ni}$, etc.; Li_2MO_3 , where $\text{M} = \text{Mn}, \text{Mo}, \text{Ir}, \text{Ru}$, etc. Adapted from Ref. 77.

3.1.3. Anode Materials

There are several materials that can be used as an anode. Figure 32 illustrates the most common classes of anode materials. These materials can be carbon, lithium titanium oxide (LTO), Germanium, Tin, Oxides (such as manganese oxide (Mn_3O_4) and cobalt oxide (Co_2O_3)), phosphides (FeP, CoF, CuP_2) and Silicon.^{78,79}

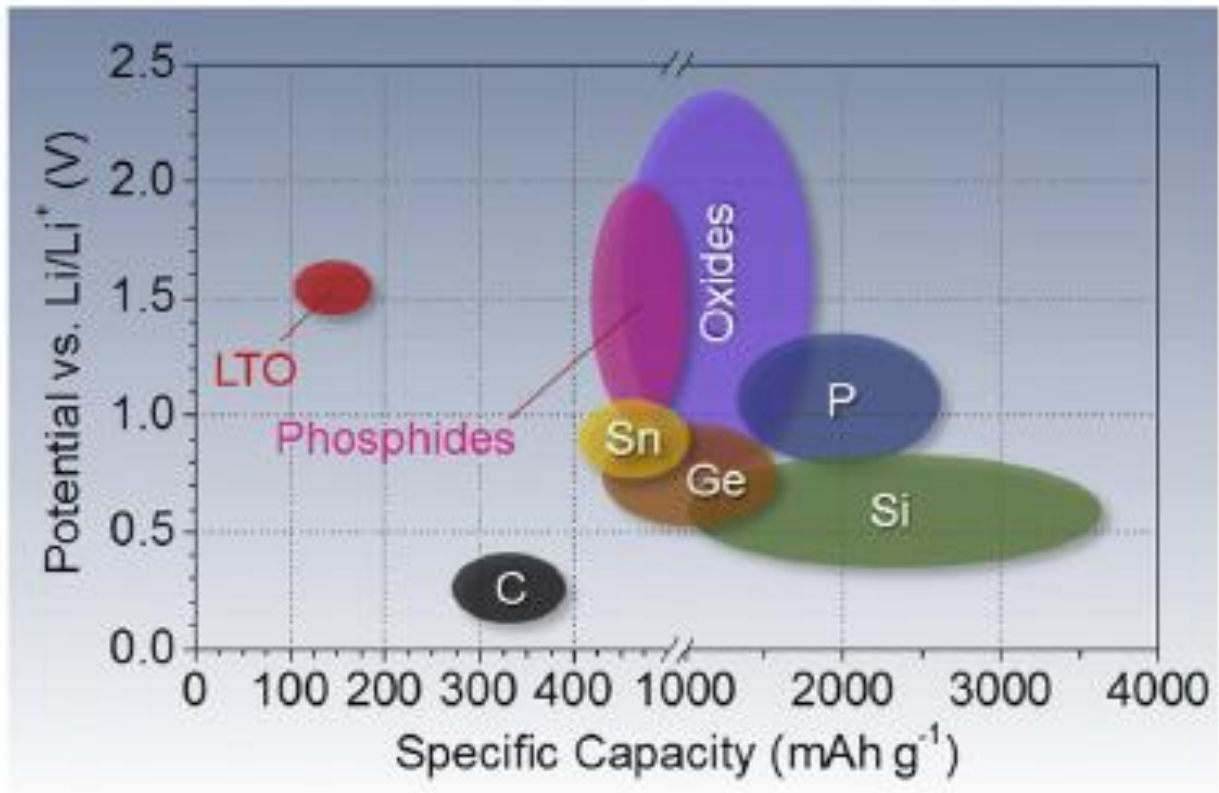


Figure 32: Conversion type anodes as a function of specific capacity. Adapted from Ref. 79.

According to the data presented In Figure 5, it is observed that during lithiation, silicon has a high specific capacity compared with Ge, C, and most of the materials shown. For this reason, Si is being extensively investigated as possible anode candidate.

3.1.3.1. Carbon

Carbon is one of the most used anodes in commercial applications. It has been in use for more than 20 years, for the reasons of abundance, low cost, along with good mechanical stability and conductivity.⁸⁰ Carbon can store 1 lithium ion for every 6 carbon atoms.⁸¹ Carbon has a very low volumetric capacity (around 330 mAh cm^{-3}) but the gravimetric capacity is higher than most cathode materials.⁸² Li^+ ions intercalate in the layered structure of the graphite type anode material (Figure 33a). This gives approximately 10% strain between the layers, and the strain can damage the SEI, reduce the battery life, and cause the graphite to be susceptible to exfoliation.⁸³

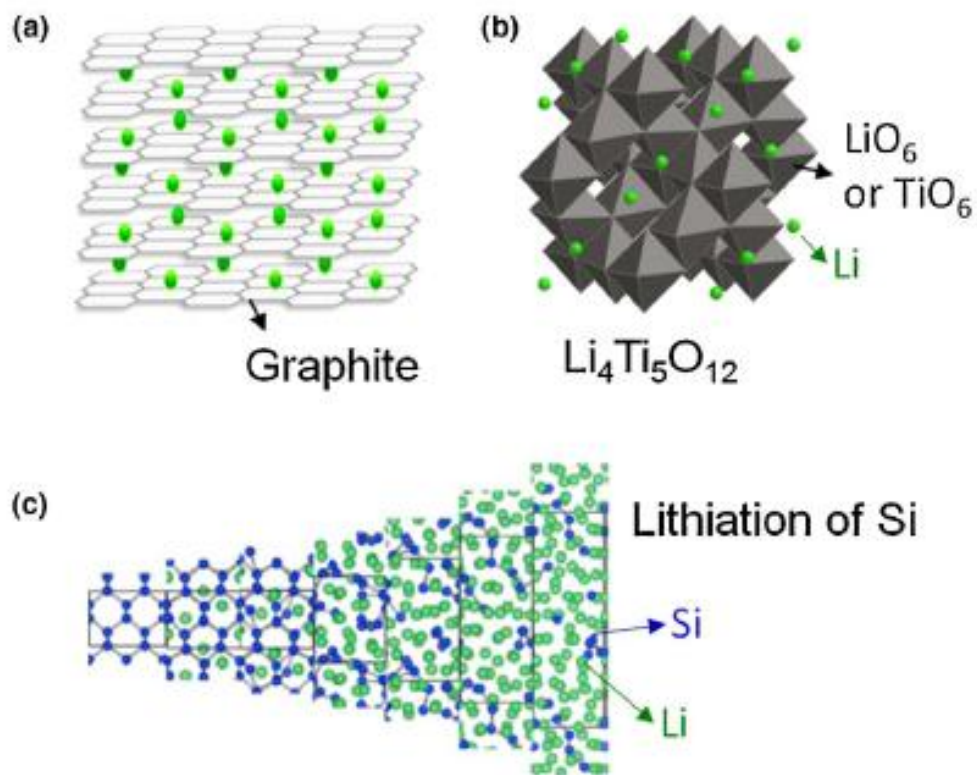


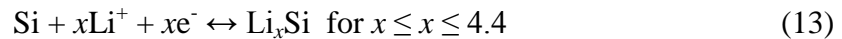
Figure 33: Crystal structures of (a) lithiated graphite, (b) lithium titanate (LTO), and (c) silicon during lithiation. Adapted from Ref. 79.

3.1.3.2. Lithium titanium Oxide

Although the cost of Lithium Titanium Oxide ($\text{Li}_4\text{Ti}_5\text{O}_{12}$ or LTO) is high, LTO-based electrodes have better stability in lithium intercalation processes, as the volume changes only 0.2%, compared with a 10% value for carbon.⁸⁴ Also, the cycle life is very long, up to thousands of cycles, but the disadvantages in the use of this material are the reactions between organic electrolytes and poor lithium diffusion.⁸⁵ In Figure 33b the structure of LTO with lithium intercalation is presented. Li ions are located between the empty spaces in the octahedra of LTO.

3.1.3.3. Silicon anodes

Silicon is a promising material for application in lithium batteries with a theoretical capacity of (4200 mA.h.g⁻¹).^{86,87} Importantly, silicon can form an alloy with lithium in a reversible reaction that can be written as follows:⁸⁸



The main problem in this alloy formed is the volume of expansion, around 400%; this expansion results in the pulverization of the anode and a cutoff of voltage during the first 10 cycles. For this purpose new morphologies of Si have to be investigated, such as nanowires, nanoparticles, and nanotubes.⁸⁹ Si films and NPs used in lithium ion batteries have a relatively short lifetime, as we can observe in Figure 34. After cycling pulverization occurs and the material loses contact with the electrodes, resulting in a poor transport of electrons.⁹⁰ On the other hand, Silicon NWs have the advantage that they are grown directly on the current collector or substrate. Since Si NWs have a small diameter, and this allows for accommodation of large volume changes avoiding fracture; in addition, Si NWs have a 1D structure, and as a result the electrons have only one direction to move. This is in contrast with films or particles, where

electrons have to move throughout interparticle contact areas.⁹¹ As illustrated in Figure 34, Si NWs keep the same morphology after cycling. However, it should be pointed out that these solid Si regions in a given nanowire can still fracture.

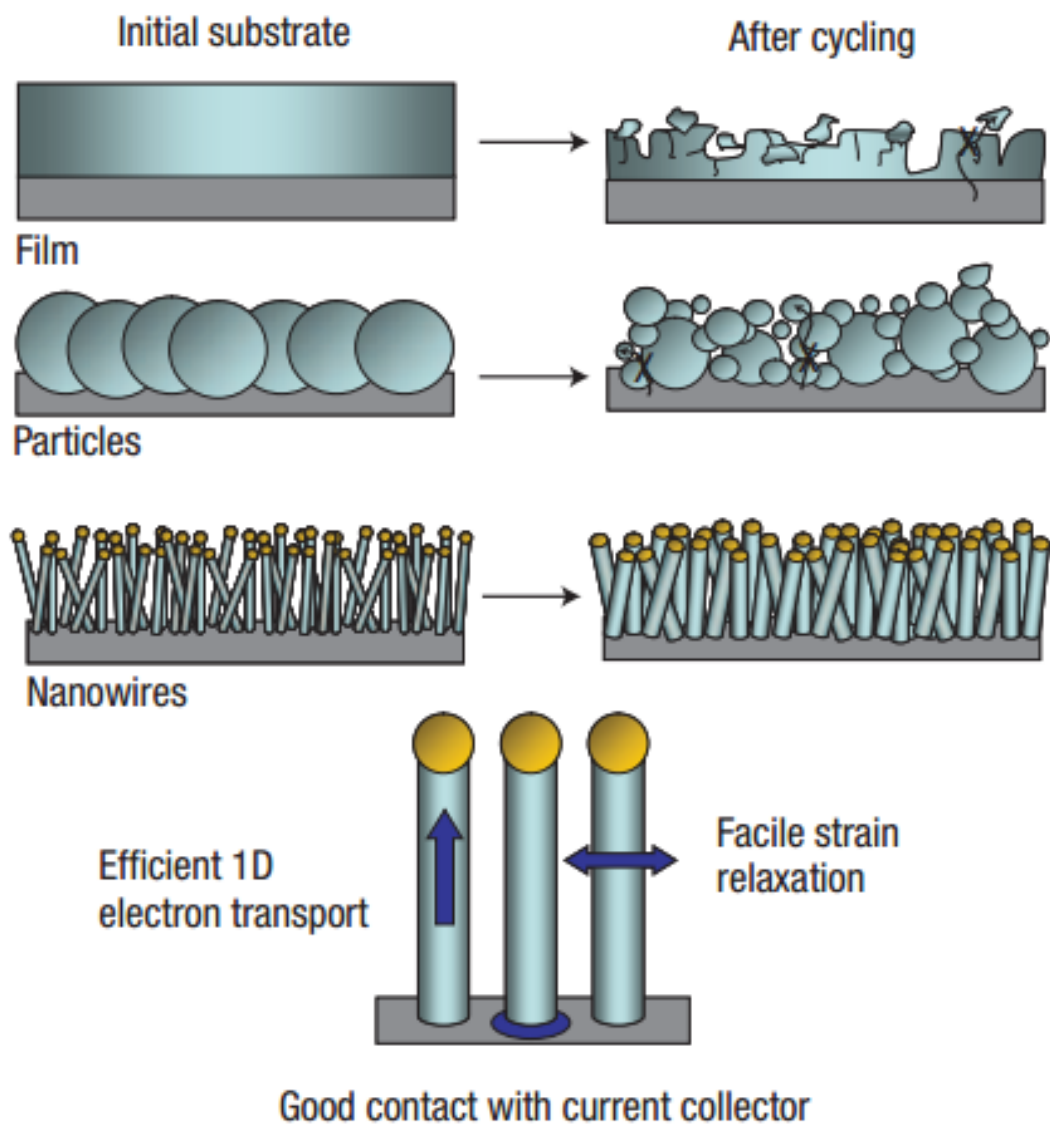


Figure 34: Schematic of morphological changes that occur in different morphologies of elemental Si during electrochemical cycling. Adapted from Ref. 87.

3.1.3.4. Silicon Nanotubes

Silicon NTs have the same dimensional advantages of Si NWs in LIB, but with the additional benefit of extra space for expansion brought about by the large interior surface and in the case of thin wall SiNTs, porous sidewalls. This space in the nanotubes gives rise to additional strain relaxation during the cycling process. Also, as more area is exposed to the electrolyte it enhances lithium diffusion, affected mainly by wall thickness in Si NTs and their length. The disadvantage is the fabrication cost compared with previous systems.⁹² In Figure 35 we can observe Si NTs tend to expand inwards during lithiation process, leaving a SEI layer in the outer surface.⁹³ Therefore, in SiNT design, wall thickness and length are the most important parameters.

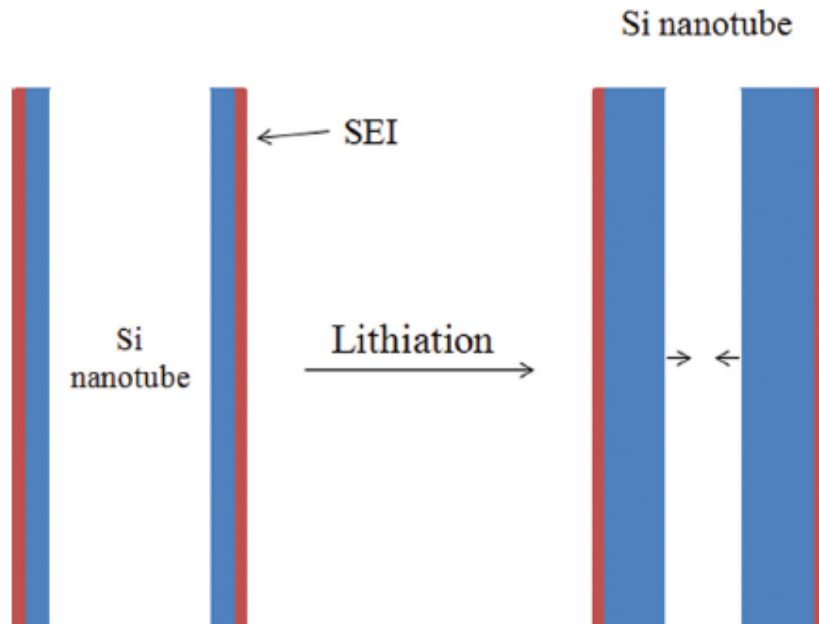


Figure 35: The schematic picture for the empty space in the silicon nanotube that allows for expansion during the discharging/charging processes. Adapted from Ref. 93.

3.2. Experimental

Silicon nanotubes are made by the process described in Chapter 2. For this application we used only stainless steel substrates 1 cm x 1 cm, with a mass of Si NTs approximately 50 μg . Details of these experiments have been published by our research group.⁹⁴

3.2.1. Assembly of lithium battery

These specific experiments were performed by Alexander T. Tesfaye and Thierry Djenizian at Aix-Marseille University, France. The electrochemical performance tests were carried out in two-electrode Swagelok-fitted cells assembled in a glovebox filled with purified argon in which moisture and oxygen content were less than 0.5 ppm. The half-cells consisted of as-formed self-standing SiNTs on stainless steel (0.55 cm^2) [slightly smaller than the as-prepared samples above] that were used as the working electrode and the current collector, respectively. A 9 mm diameter Li foil was used as the counter electrode and a Whatman glass microfiber separator soaked with lithium hexafluorophosphate in ethylene carbonate and diethylene carbonate (1 M LiPF_6 in (EC:DEC 1:1 w/w) was used as separator. The mass of the active material was $\sim 30 \mu\text{g}$. The cyclic voltammetry and galvanostatic tests were done using a VMP3 potentiostat (Bio Logic, France). Each cyclic voltammogram was performed in a potential window of 0.01–1.75 V vs Li/ Li^+ at a scan rate of $0.1 \text{ mV}\cdot\text{s}^{-1}$. The galvanostatic tests of the assembled cells were done at multiple C-rates; recall that C/n means the battery is fully charged or discharged up to its total storage capacity in n hours (for this work $1 \text{ C} = 4.2 \text{ A g}^{-1}$). The gravimetric capacity values were calculated on the basis of the weight of the active material. Gravimetric capacity in mAh/g is a measure of the total charge capacity stored by the cell or battery, per gram of the battery's weight.⁹⁵ For all electrochemical tests, additives and binders were not used.

3.3. Results and Discussion

3.3.1. SEM, TEM and EDX characterization

As in the SiNTs described in Chapter 2, all SiNTs samples in these experiments were characterized by SEM, EDX and TEM. In Figure 36 the characterization data for SiNTs prior to the electrochemical studies is shown. Figure 37a shows a very dense packing of Si NTs on stainless steel, with a vertical orientation for the nanotubes. TEM images (Fig 36b) reveal a porous wall, with a wall thickness of 10 nm, an inner diameter of 57 ± 11 nm, and a length of 2 μm . EDX provides information with regard to composition; typical EDX analysis (Figure 37c) reveals only the presence of silicon and oxygen. These Si NTs are highly crystalline, as HR TEM imaging shows crystalline regions with a lattice spacing of 0.31 nm, corresponding to the (111) index of cubic silicon (Figure 36d).

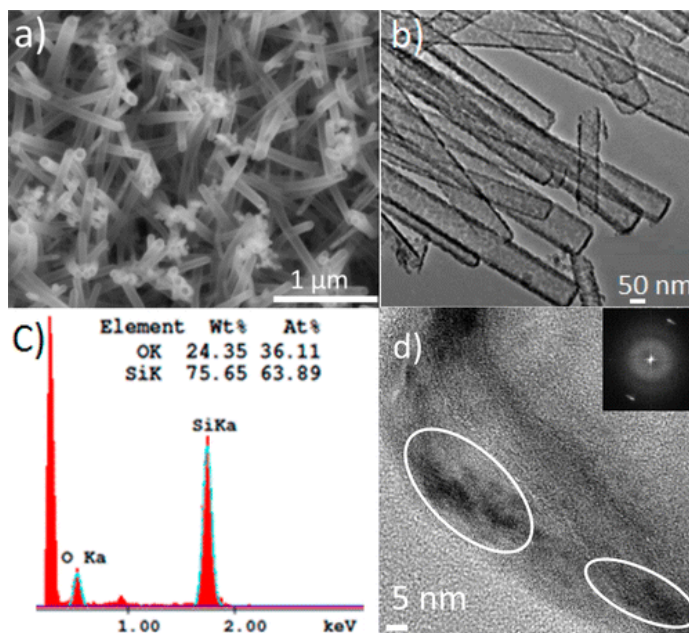


Figure 36. (a) Field-emission SEM image of SiNTs. (b) TEM of SiNTs. (c) EDX spectrum of SiNTs (from TEM analysis); small peak near 1.00 keV is associated with TEM sample grid. (d) HRTEM of SiNTs. White circles represent crystalline domains of $\langle 111 \rangle$ orientation; inset: FFT indicating sample crystallinity.

3.3.2. Electrochemical Characterization

To study the electrochemical performance of these silicon nanotube-based cells, our collaborators recorded cyclic voltammograms. The voltammograms were taken up to the 30th cycle as observed in Figure 37. Four characteristic peaks are observed. The peaks at 0.4 V and 0.1 V corresponds to an alloy formed, presumed to be Li_xSi .⁹⁶ Other peaks observed at 0.38 and 0.5 V are attributed to the reversible reaction(s) of the alloy to form $\text{Si} + x\text{Li}^+$.³² There is also one peak at 1.2 V; this peak corresponds to the formation of a SEI.³² Finally the peaks at 0.7 and 1.0 V are believed to be associated with the reaction between the iron oxide in the stainless steel and the lithium.⁹⁷

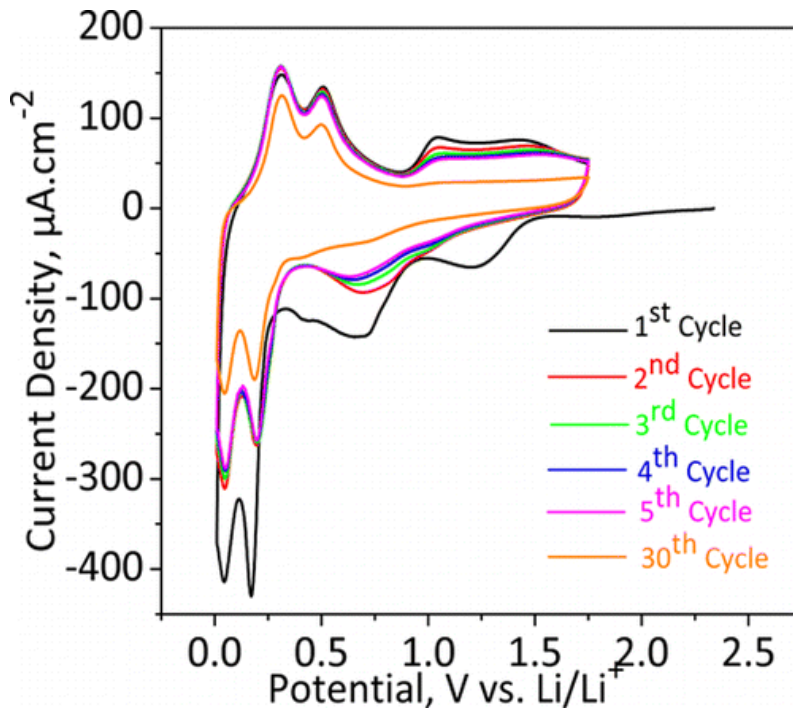


Figure 37. Cyclic voltammogram recorded for the SiNTs in the potential window of 0.01–1.75 V vs Li/Li^+ at the scan rate of 0.1 mV s^{-1} .

Charge-discharge curves are shown in Figure 39a; these curves were performed at C/20 for Si NTs. We can observe four plateaus at potentials of 0.1 V, 0.4 V and 1.2 V vs Li/Li^+ that

correspond to electrolyte decomposition and formation of Li_xSi .⁹⁸ The small broad peaks at potentials of 0.7 and 1.0 V versus Li/Li^+ can be attributed to the reaction of lithium with iron oxide present in the stainless steel substrate.⁹⁹ We observed a loss in discharge capacity around 63 % between the first and second cycles (Table 2). The likely explanation for this reduction is due to the formation of a SEI layer and the irreversible reaction of Li^+ of Iron (III) Oxide. Even when the huge capacity is lost, the values can be stable for more than 30 cycles, reaching $\sim 1670 \text{ mAhg}^{-1}$ and a 54% coulombic efficiency. In Table 2 we can observe that with regard to multiple parameters, our system is better than most 1-D nanoscale Si systems previously reported. For example, in the case of SiNRs, the nanorods are mesoporous with a diameter of 78 nm, and the pore size is 12 nm; however the coulombic efficiency and discharge capacity is not as good as our system.¹⁰⁰ Other Si NTs reported in the table are 15 nm in diameter, 50-200 nm in length; and a pore size of 3.9 nm. While the coulombic efficiency of these smaller width NTs is higher than that of our system, we report a higher discharge capacity.¹⁰¹ However, our porous SiNT system lacks the coulombic efficiency of previously reported double-walled Si NTs (DW SiNTs). These tubes are several microns long, diameters from 50 to 800 nm, and a two wall geometry: one made of Si and the second made of SiO_2 . The coulombic efficiency is reported to be 99.9 % with a very good performance in the long term (up to 6000 cycles).^{102,103}

Porous Si NTs prepared in our lab were studied at several C-rates to learn more about their performance, stability and cycling life (Figure 38b). At a high current density (1C), the gravimetric capacity was 450 mAhg^{-1} . However, when the C-rate is restored to C/10, the capacity value is 800 mAhg^{-1} and this value is retained more than 180 cycles. Also in the inset of Figure 38b we can observe a capacity retention of more than 97% and a coulombic efficiency more than 75% for the first 5 cycles.

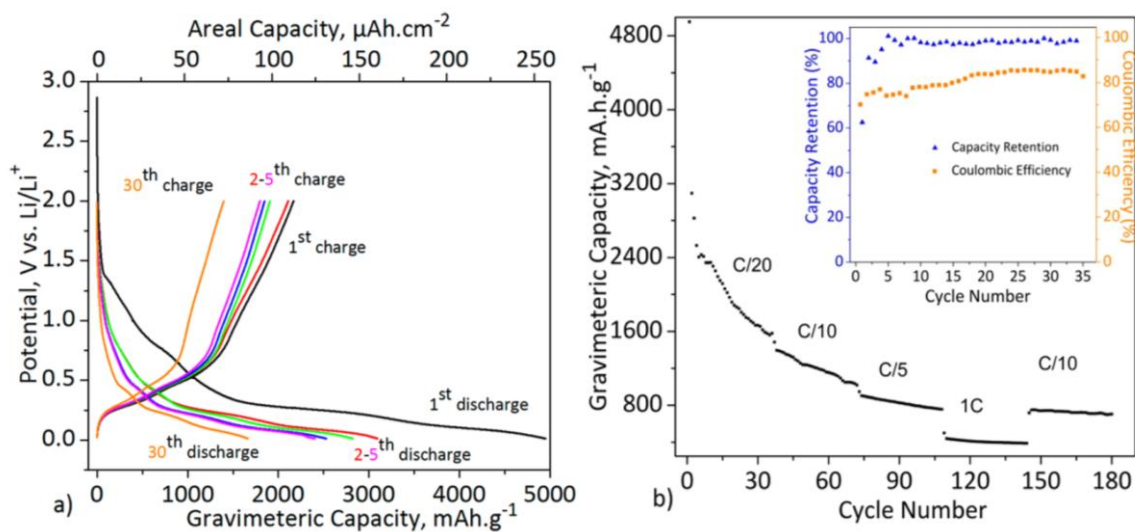


Figure 38. (a) Galvanostatic discharge–charge profile of SiNTs at C/20 and (b) their cycling performance at multiple C-rates. The inset shows the capacity retention and the Coulombic efficiency vs cycle number at C/20.

Table 3: Comparison of the electrochemical performance of various Si NTs with regard to lithium cycling.

| Working electrode | First discharge capacity (mAhg ⁻¹) at C-rate | First irreversible capacity loss (%) | Discharge capacity after (n) cycle (mAh g ⁻¹) | Capacity retention (%) after (n) cycles | Coulombic efficiency (%) after (n) cycles |
|---------------------------------|--|--------------------------------------|---|---|---|
| Porous SiNTs (this work) | 4950 (0.05C) | 63 | 1670 (30) | 99.26 (30) | 84.6 (30) |
| SiNTs ¹⁰¹ | 1924 (0.5C) | 80 | 1158 (10) | NA | 60 (10) |
| SiNRs ¹⁰⁰ | 3285 (0.05C) | 48.3 | 1398 (20) | NA | 98.6 (20) |
| DW Si NTs ¹⁰² | 1780 (0.2C) | 99.9 | 1566 (6000) | >99.9 (6000) | >99.9 (6000) |

One possible explanation of the high specific capacity retained after several cycles can be facilitated by an examination of the role of the porous Si NTs morphology. These Si NTs have an inner void space contributing to the expansion of around 400% when the alloy Li_xSi is

formed. In addition Si NTs have a very high surface area and a porous wall with even further reactive sites available for Li intercalation.

After the electrochemical studies were performed, the lithium cell was disassembled and characterized by SEM and EDX. In the SEM image of Figure 39 it is clear that Si NTs retain the tubular morphology during the entire process. The darker area is attributed to SEI formation; this SEI layer consists mainly of LiF, Li₂CO₃ and Li₂O. Composition of the SEI layer can be confirmed by EDX (Figure 40), which shows peaks for F, C and O in agreement with a typical SEI layer. Unfortunately, some of the Si NTs were detached from the substrate. Some of these problems can be addressed in future experiments by depositing chromium on the top of the Si NTs to avoid detachment during a given electrochemical cycling experiment. Use of a solid state electrolyte may also improve efficiency and stability in these cells as well.

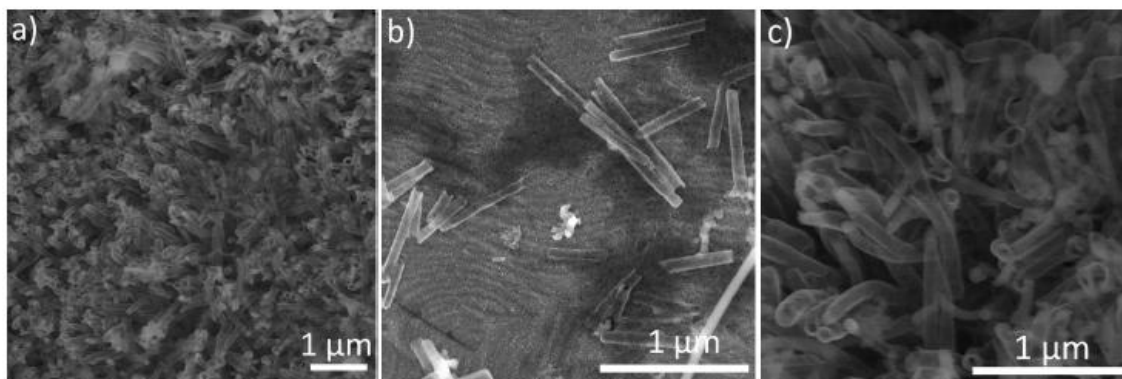
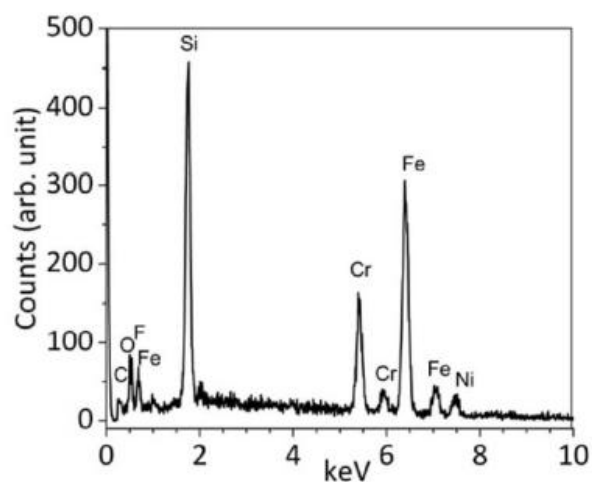


Figure 39: SEM of Si NTs after lithiation.



| Element | Si | Fe | Cr | Ni | C | O | F | Total |
|----------|-------|-------|-------|------|-------|-------|------|-------|
| Weight % | 17.03 | 44.64 | 13.22 | 5.46 | 11.78 | 5.83 | 2.04 | 100 |
| Atomic % | 18.92 | 24.94 | 7.93 | 2.9 | 30.6 | 11.36 | 3.35 | 100 |

Figure 40: EDX spectrum and atomic/weight percentages of Si NTs after lithiation.

3.4. Summary

In this chapter, the properties of Si NTs on stainless steel substrates possessing a porous wall with a thickness of 10 nm and a length around 2 μm are reported. In particular, Li ion electrochemical cycling studies carried out with our collaborators found that such systems have a capacity around 1670 mAhg^{-1} at the beginning; by the end of 30 cycles the capacity drops to 800 mAhg^{-1} and retention of this value for the next 180 cycles at $C/10$. While these values are encouraging, the SiNT system clearly requires additional improvement. We need to reduce the formation of SEI, ideally perhaps through the use of a solid state electrolyte and a Cr adhesion layer. These experiments are in progress with our collaborators.

Chapter IV

Silicon Nanotubes Loaded with Iron Oxide Nanoparticles

4.1. Introduction

Superparamagnetic iron oxide nanoparticles (Fe_3O_4 NPs) are receiving extensive attention in areas such as catalysis,¹⁰⁴ as well as in biomedical applications such as cell labelling,¹⁰⁵ biosensing,¹⁰⁶ drug delivery,¹⁰⁷ hyperthermia,¹⁰⁸ and magnetic resonance imaging (MRI).¹⁰⁹ In addition, Fe_3O_4 NPs have a very low toxicity and are considered to be biocompatible.^{110,111}

For the specific application of magnetic resonance imaging, the quality of an MRI contrast agent is often evaluated by the relaxivity parameters r_1 or r_2 , which describe the ability of a contrast agent to shorten the T_1 or T_2 relaxation time of water. To overcome existing disadvantages of Gd-complex based T_1 MRI contrast agents such as PrimovistTM (gadolinium (4S)-4-(4-ethoxybenzyl)-3,6,9-tris(carboxylatomethyl)-3,6,9-triazaundecanoic acid disodium salt),¹¹² the development of nanoparticulate T_1 contrast agents that contain Gd^{3+} or Mn^{2+} ions has been intensively pursued in recent years.¹¹³ However, toxicity problems still persist in Gd^{3+} nanoparticle-based T_1 contrast agents.¹¹⁴ Iron oxide is more biocompatible than gadolinium or manganese-based materials because iron species are relatively rich in human blood.¹¹⁵ Unlike the Gd-complexes, however, iron oxide MRI contrast agents are considered to be a negative contrast agent (or r_2 weighted). For a given material, the relative enhancement in relaxation time is determined by several factors, such as: 1) nanoparticle size; 2) nanoparticle composition and 3) nanoparticle surface coating.¹¹⁶

For MRI applications, Fe_3O_4 nanoparticles (NPs) have been reported with different surface functional groups to increase solubility,¹¹⁷ and also in the form of other geometries such as Fe_3O_4 nanorods and Fe_3O_4 clusters^{118,119} formed by aggregation of individual Fe_3O_4 NPs. However these clusters lack uniformity and a well-defined structure. There is one report of Fe_3O_4

NPs formed in carbon nanotubes.¹²⁰ As these NPs are formed *in situ*, they do not have an uniform particle size distribution.¹²¹ Until this work, there was no report of Si NTs loaded with Fe₃O₄ NPs - either in terms of fundamental properties or relevance for MRI applications.

In this chapter several concepts regarding fundamental magnetic properties need to be defined here:

ZFC/FC – Zero Field Cooling / Field Cooling . ZFC the magnetic particles is cooled below their blocking temperature in zero applied field. In FC, particles are cooled below their blocking temperature in an applied field.¹²²

Blocking temperature T_B - the magnetic moment in superparamagnetic NPs flips very rapidly and all that is observed is the resulting average moment which is near zero. Only for temperatures below T_B does the average moment stay fixed in one direction during the time of the magnetic measurements (ZFC/FC).¹²²

Coercitivity - the coercivity, also called the magnetic coercivity, coercive field or coercive force, is a measure of the ability of a ferromagnetic material to withstand an external magnetic field without becoming demagnetized.¹²²

4.2. Experimental – Fundamental Magnetization Measurements

4.2.1. Loading of iron oxide nanoparticles in thick walled Si NTs.

Loading of the Si NTs with Fe₃O₄ NPs is typically achieved by initial removal of the Si NTs film from the underlying substrate (such as FTO glass) (‘unzipping’) and placing it face down on top of a Nd magnet with a piece of filter paper in between. Fe₃O₄ NPs (hexane solution)

with a typical concentration of NPs of 5 $\mu\text{g/mL}$ are added dropwise, followed by an acetone rinse, and air drying. Fe_3O_4 NPs were supplied by Dr. Puerto Morales from the Institute of Material Science, CSIC Madrid, Spain. This process for loading Fe_3O_4 NPs into SiNTs is illustrated in Figure 41.

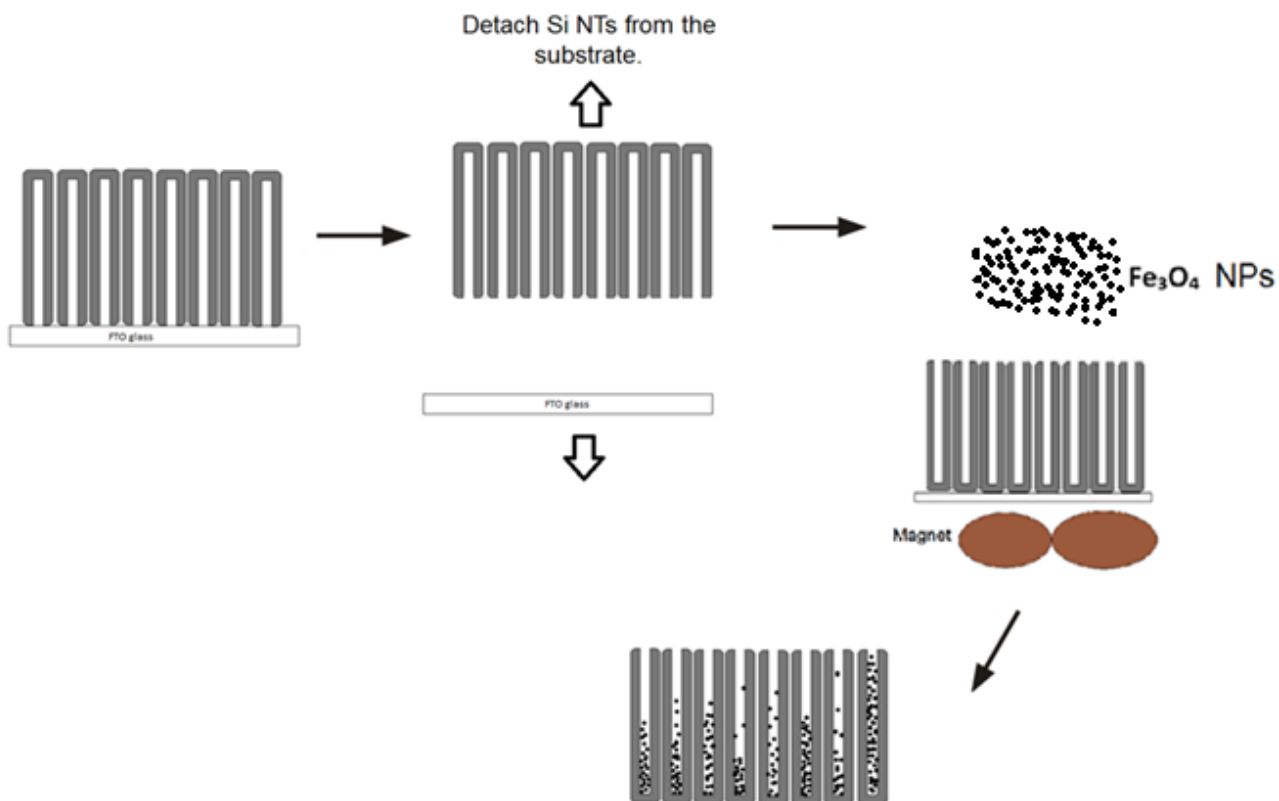


Figure 41: Process for loading Fe_3O_4 NPs in ‘uncapped’ Si NTs.

4.2.2. Procedure for loading 4 nm Fe_3O_4 NPs in 10 nm Shell thickness Si NTs

Si NTs with porous sidewalls (10 nm shell thickness) still on the substrate are placed face up on top of a Nd magnet with a piece of filter paper in between. Fe_3O_4 NPs (oleic acid terminated, hexane solution) are added dropwise, followed by rinsing the sample with

acetone several times, and allowed to air dry. The concentration of Fe_3O_4 NPs used for the experiment is $\sim 5 \mu\text{g/ml}$. Since the loading is achieved by diffusion of Fe_3O_4 NPs through the porous nanotube sidewalls, only 4 nm Fe_3O_4 NPs can be used for this loading technique. This loading process is illustrated below in Figure 42.

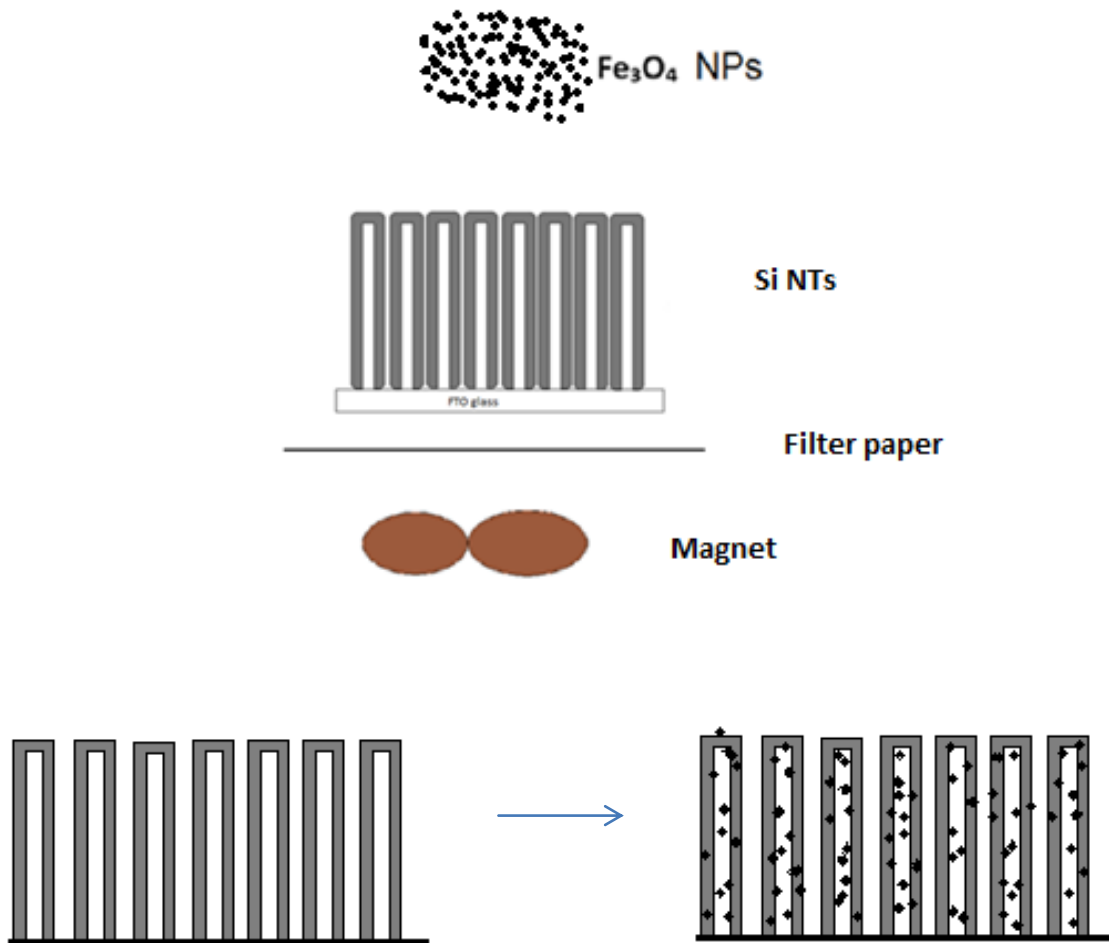


Figure 42: Process for loading Fe_3O_4 NPs in Si NTs by magnetic field-assisted diffusion.

4.3. Results and Discussion

4.3.1. Morphological characterization of Fe₃O₄ NPs and Fe₃O₄ NPs in Si NTs.

Transmission Electron Microscopy (TEM) analysis [JEOL JEM-2100] confirms that the Fe₃O₄ NPs used in these experiments are uniformly spherical and have a narrow size distribution of 4.52 (\pm 0.65) nm, 5.10 (\pm 0.98) nm, 8.15 (\pm 0.76) nm and 10.60 (\pm 2.84) nm. High Resolution TEM (HRTEM) analysis confirms that each particle possesses well-oriented single crystalline domains with the distance between two adjacent lattice fringes of 0.258 nm, corresponding to lattice spacing of (311) planes of magnetite phase Fe₃O₄ (with a reported value of 0.253 nm).¹²³ The Fe₃O₄ NPs are readily observed in the TEM images of Figure 43.

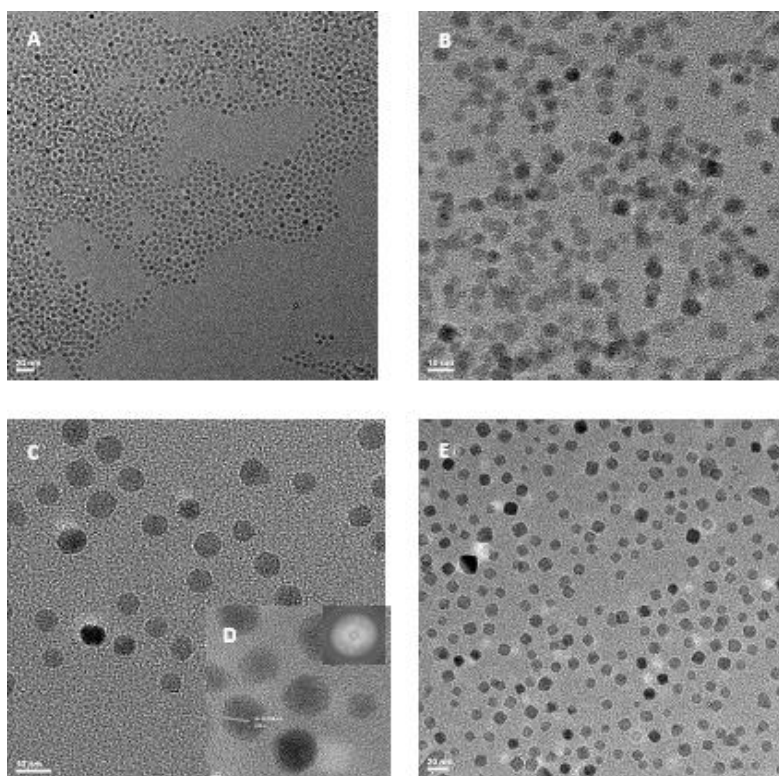


Figure 43: TEM images of Fe₃O₄ NPs of: a) 4 nm diameter; b) 5 nm diameter; c) 8 nm diameter; d) (HRTEM) 8 nm diameter; and e) 10 nm diameter.

Figure 45 shows selected TEM images of Si NTs with different wall thicknesses (10, 40, and 80 nm) loaded with Fe₃O₄ NPs of 4 nm diameter. Thus far Fe₃O₄ NPs of 4, 8, and 10 nm diameter have been successfully infiltrated into these nanotubes. Relatively dense packing of the magnetite nanoparticles is readily achieved. All infiltrated nanotubes can be manipulated with a simple Nd magnet (Fig 44d).

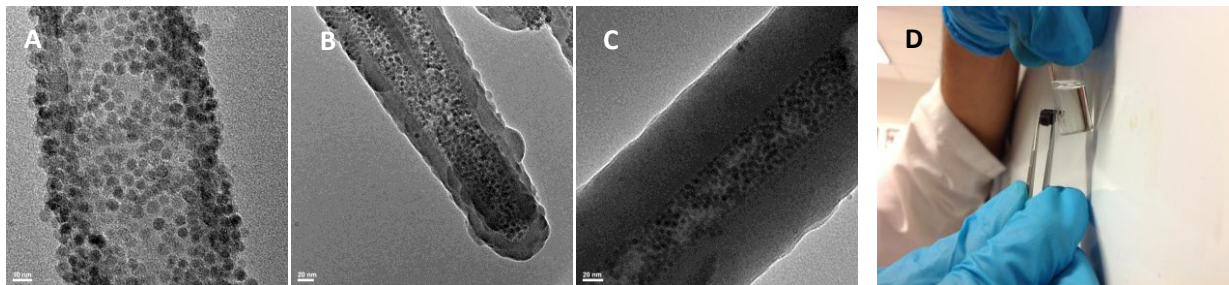


Figure 44: Si NTs loaded with 4 nm Fe₃O₄ NPs. a) 10 nm shell thickness. b) 40 nm shell thickness. c) 80 nm shell thickness. d) Si NTs loaded with Fe₃O₄ NPs and manipulated with a magnetic field.

4.3.2. Magnetic characterization of Fe₃O₄ NPs and Fe₃O₄ NPs in Si NTs.

Fundamental magnetization studies for these new Fe₃O₄ NP / Si NT structures were performed using a Vibrating Sample Magnetometer (VSM) with temperatures between 4 to 300 K and a field range between ± 1 T. These experiments were carried out by Petra Granitzer and Klemens Rumpf of the Institute of Physics at Karl Franzens University Graz. Blocking temperature was measured, because such values have an impact as the lower practical limit that the material can be used in a biological system. The observed blocking temperature T_B depends on the particle size and as well as the distance between neighboring particles filled within the tubes. Particle-particle distance inside the Si NTs is given only by the organic coating (approximately 4 nm) so magnetic exchange coupling is excluded.^{124,125} The thermal energy associated with this system can be expressed as:

$$25k_B T_B = K_1 V \left(1 - \frac{\mu_0 M_S H_C}{2K_1} \right)^2 \quad (14)$$

K_1 is the anisotropy constant, M_s the saturation magnetization, H_c the coercive field, V the volume of an individual particle. Anisotropy constant K_1 of bulk Fe_3O_4 is $K_1 = 1.35 \times 10^4 \text{ J m}^{-3}$.¹²⁶ One has to be aware that the anisotropy constant of a single particle changes with the reduction of its size and also magnetic inter-particle interactions lead to an enhancement of the magnetic anisotropy of the system.¹²⁷

We can use the experimental T_B values of our system Fe_3O_4 NPs loaded into Si NTs to calculate K_1 values (We have to assume Fe_3O_4 NPs don't interact). The possible orientation spin states that could be adopted by the magnetization in a given material are separated through an energy barrier imposed by the anisotropy constant, K_1 .¹²² K_1 values obtained were: for 10 nm particles ($T_B = 30 \text{ K}$) $K_1 = 1.98 \times 10^4 \text{ J m}^{-3}$, 8 nm particles ($T_B = 20 \text{ K}$) $K_1 = 2.5 \times 10^4 \text{ J m}^{-3}$, 5 nm particles ($T_B = 15 \text{ K}$) $K_1 = 7.9 \times 10^4 \text{ J m}^{-3}$ and for 4 nm particles ($T_B = 12 \text{ K}$) $K_1 = 1.2 \times 10^5 \text{ J m}^{-3}$. The K_1 values obtained are higher than the bulk. This can be explained with possible two reasons: 1) weak magnetic coupling; or 2) surface effects associated with the oleic acid coating of the particles. In Figure 45 we can observe the experimental values T_B in Si NTs loaded with Fe_3O_4 NPs. The measured blocking temperatures of dispersed Fe_3O_4 NPs are the same as our Fe_3O_4 NPs/ Si NT system, with the likely reason being that Fe_3O_4 NPs do not interact at relatively long range inside a Si NT.¹²⁸

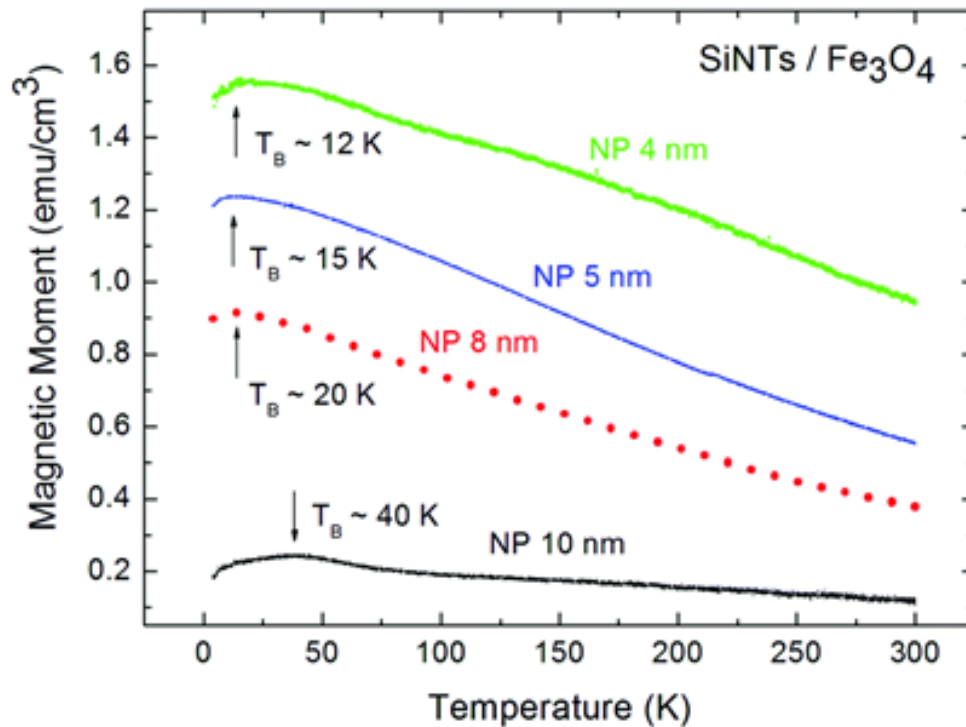


Figure 45: ZFC/FC measurements showing size dependent shift of T_B in the case of Si NTs filled with Fe_3O_4 NPs.

In another experiment, a commercially-available sample of Fe_3O_4 NP with a stated average diameter of 10 nm was obtained and loaded into SiNTs. Interestingly, in this sample three distinct peaks appear in the measurements of magnetic moment as a function of temperature as we can observe in Figure 46. The reason for multiple peaks in such a plot is attributed to the broad size distribution of this sample from Sigma-Aldrich. The three blocking temperatures are $T_B = 30$ K for 10 nm Fe_3O_4 NPs, $T_B = 110$ K for 17.5 nm Fe_3O_4 NPs and $T_B = 160$ K for 20 nm Fe_3O_4 NPs. These values were calculated by assuming the anisotropy constant of bulk magnetite and assuming that particles do not interact.

Thus in this case it is possible to distinguish the size distribution of 10 nm Fe_3O_4 NPs / Si NTs due to the very weak interaction behavior. The variation in T_B values for commercially obtained Fe_3O_4 NPs from Sigma Aldrich (Figure 47) ($T_B = 40$ K) and monodisperse 10 nm

obtained from collaborators ($T_B = 30$ K) is presumably because of subtle differences in their size distributions. This kind of measurement permits a characterization of the sample dispersity without the need of additional microscopy studies such as TEM.

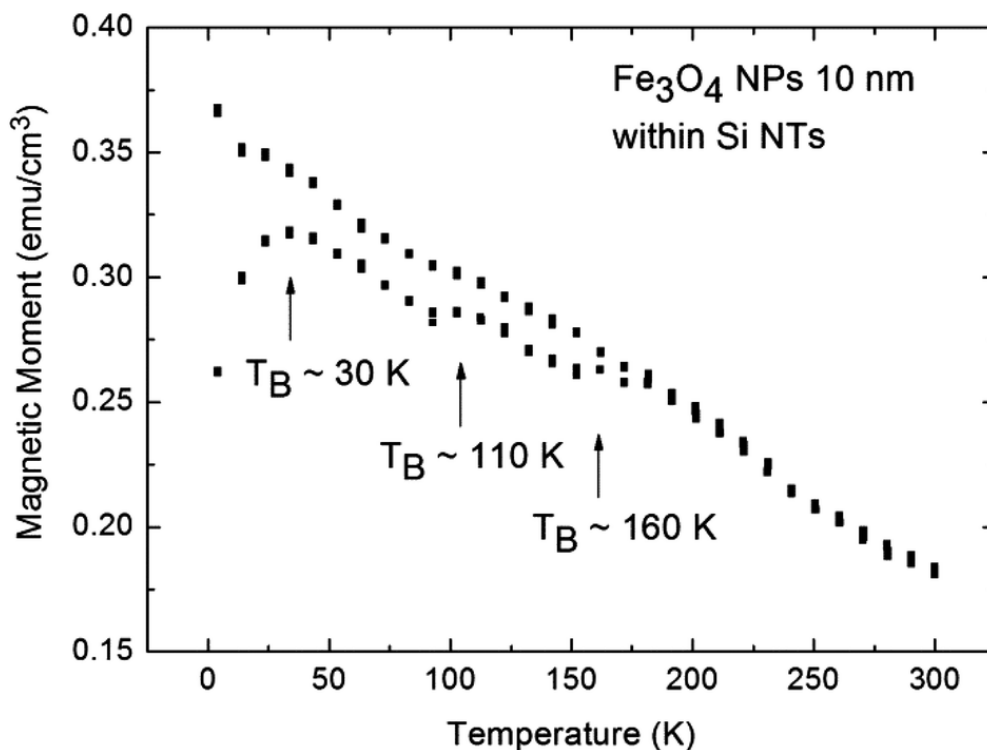


Figure 46: ZFC/FC measurements showing the effect of infiltrating a 10 nm Fe₃O₄ NP sample with a polydisperse size range into a SiNT template with a 70 nm wall thickness. Three distinct peaks of T_B appear due to this particle solution containing different particle sizes indicating that the particles do not magnetically interact.

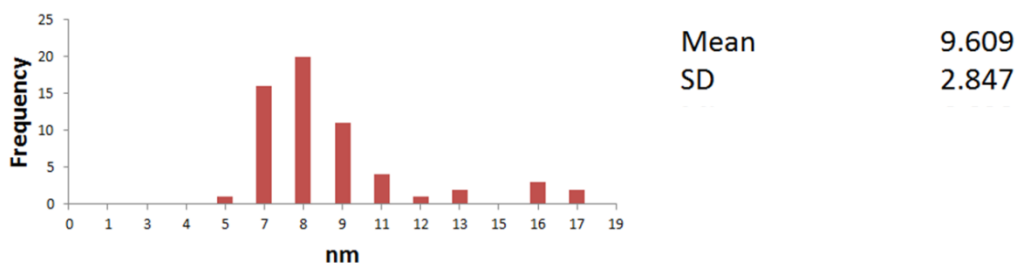


Figure 47: Size distribution for 10 nm Fe₃O₄ NPs from Sigma-Aldrich.

It should be emphasized here that all samples offer a negligible coercivity at $T = 300\text{K}$, very far away from T_B . This means that no magnetic remanence is present and thus magnetization of the samples vanishes if the applied magnetic field is turned off. This is important for future applications of this type of nanoconstruct in magnetically guided drug delivery. Biocompatible Si NTs can be used as a compartment to facilitate the movement of large numbers of Fe_3O_4 NP *in vivo*.

4.4 Experimental - Si NTs loaded with Iron Oxide Nanoparticles for Relaxometry Measurements

4.4.1 Loading of iron oxide nanoparticles in thick wall Si NTs.

The loading of Fe_3O_4 NPs in Si NTs used in this section was identical to that described in Section 4.2. T_1 and T_2 values were analyzed for containing Si NTs with 40 nm and 70 nm wall thickness Si NTs loaded with Fe_3O_4 NPs of 5 nm and 8 nm in diameter. T_1 and T_2 values were measured by preparing several concentrations of Si NTs loaded with Fe_3O_4 NPs then measured with a relaxometer (Bruker Minispec mq60) operating at 1.41 Tesla (T). The data is analyzed by plotting Fe concentration vs $1/T_1$ or $1/T_2$; the slope formed gives the value r_1 or r_2 . These values can be compared with literature values.

4.4.2. APTES and PEG-diacid (600) functionalization

PEG functionalization of the nanotube surface is made to avoid Si NTs precipitation. The Si NTs were immersed in 1% (3-aminopropyl)triethoxysilane (APTES) solution (4 hrs), followed by rinsing with DI water. Next, a solution of poly(ethylene glycol) diacid 600 (PEG-diacid 600)

from Sigma-Aldrich is prepared by adding PEG-diacid (600) (3.3 mmol), EDC (1 mmol) and NHS (1 mmol) to 2 mL of water. The mixture was stirred for 15 min. Then 200 μg APTES-functionalized Si NTs (APTES-Si NTs) were added to the mixture and stirred for 3 h. The product was dialyzed using SpectrumTM Dialysis Membrane tubing 12-14 kD, against DI water by changing DI water several times. The samples were stored in solution at room temperature for further use.

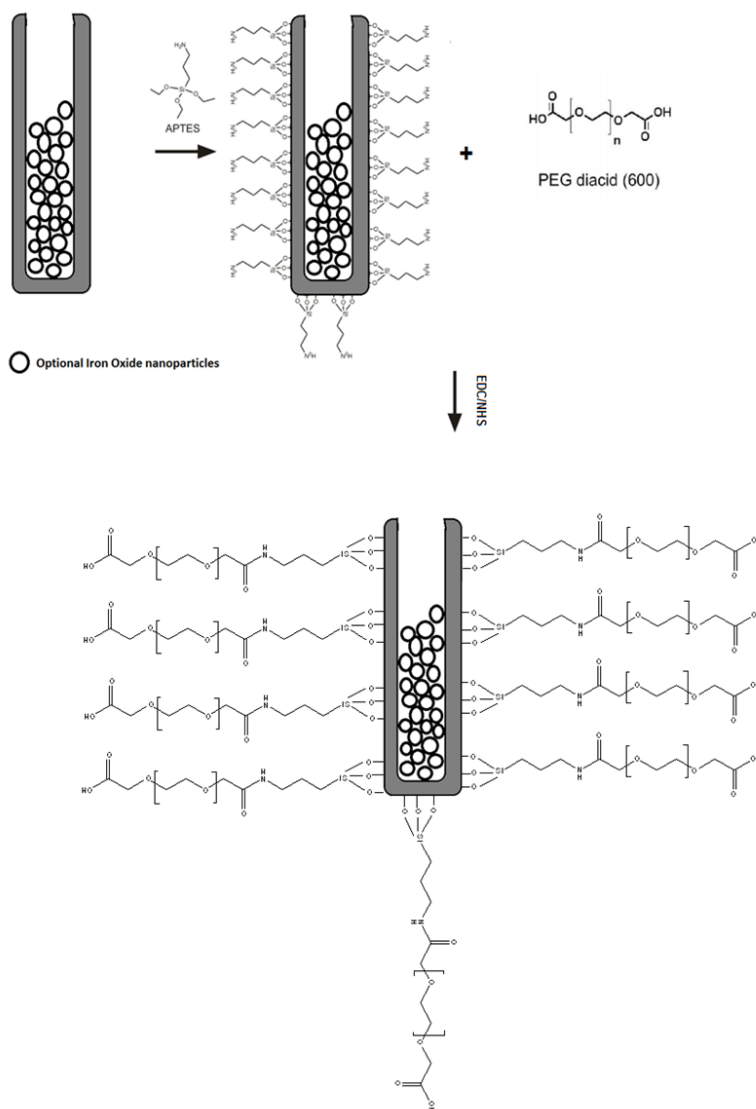


Figure 48: Diagram showing the process for Si NTs functionalized with APTES and PEG(diacid).

4.4.3. Ferrozine assay

A Ferrozine assay was used to determine the concentration of iron (necessary for relaxometry measurements). This assay consists of first preparing 400 μL of a solution containing a known amount of Si NTs loaded with Fe_3O_4 NPs. This solution is mixed with 400 μL of 12 M HCl and allowed to sit for 1 hr, Then 400 μL of 12 M NaOH is added to neutralize the solution, followed by addition of 96 μL of 2.8 M HONH_2 (in 4 M HCl) and again the total solution is allowed to sit for 1 hr. Finally, 40 μL of 10 M ammonium acetate and 240 μL 300 mM of Ferrozine (in 0.1 M of Ammonium acetate) is added. The solution is allowed to sit overnight and the absorbance at 562 nm is measured.¹²⁹ This assay is made base of 30% Fe_3O_4 NPs loading in Si NTs.



Figure 49: Gradient of colours obtained during the calibration curve for the Ferrozine assay. The darkest pink colour represents the high concentration of iron, while the clear one at right is the one with lowest concentration.

4.5. Results and Discussion

4.5.1. Si NTs loaded with Fe_3O_4 NP characterization.

Compared to the morphology of anodized porous silicon, Si NTs offer a more uniform wall structure with a separation distance of magnetic NPs between tube interiors that is effectively two times the wall thickness of a given type of Si NT. TEM confirms the successful loading of Fe_3O_4 NPS into the Si NTs. Fig 50a shows empty Si NTs with a wall thickness of 40 nm; Figs 50b,c show Si NTs loaded with 5 nm and 8 nm sized Fe_3O_4 NPs with a 40 nm wall

thickness. In Fig 50b, a close packing structure for 5 nm Fe_3O_4 NPs loaded into Si NTs is observed. Fig 50d shows empty Si NTs with a wall thickness of 70 nm, with Fig 50,f showing these sized Si NTs loaded with 5 nm and 8 nm Fe_3O_4 NPs in 70 nm wall thickness Si NTs. A relatively uniform filling of Fe_3O_4 NPs inside Si NTs is observed for each case. No significant amounts of Fe_3O_4 NPs are observed outside the Si NTs, inferring that the washing process was successful with no Fe_3O_4 NPs removed from inside the nanotubes.

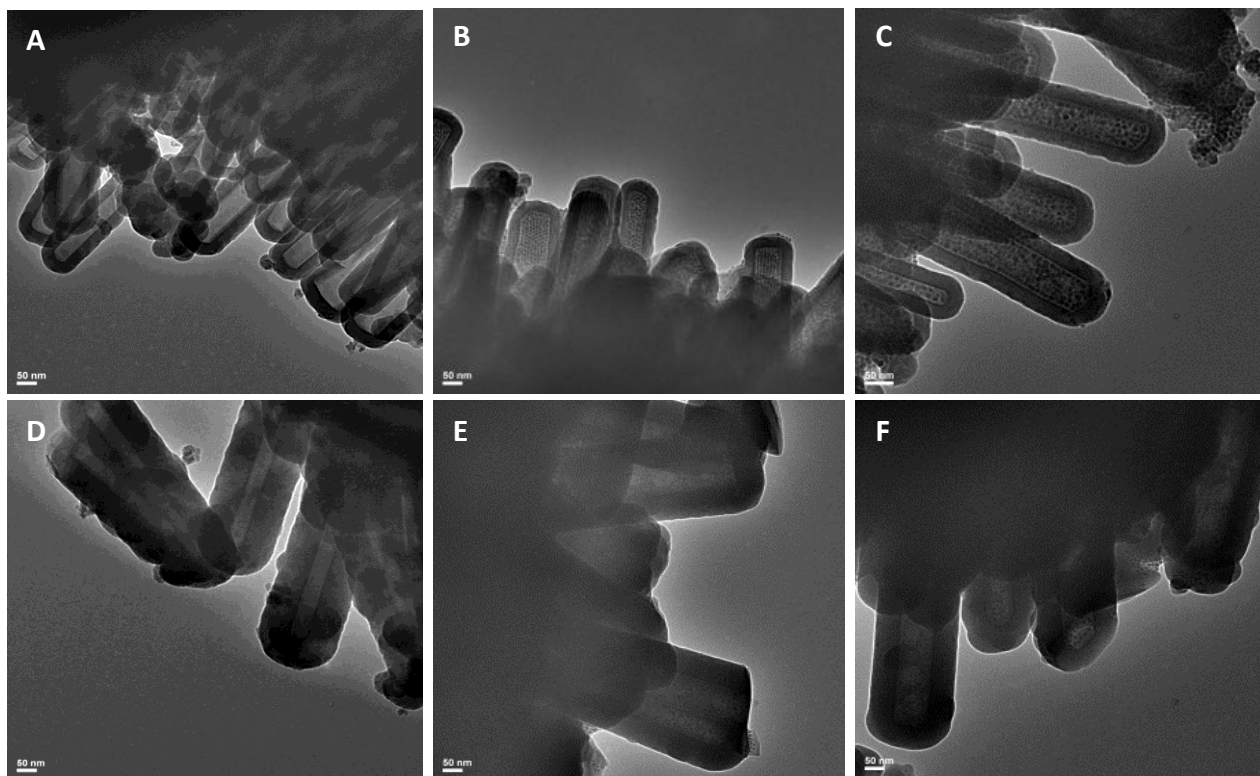


Figure 50: TEM of 40 nm Si NTs a) empty Si NTs, b) Si NTs loaded with 5nm Fe_3O_4 , c)) Si NTs loaded with 8 nm Fe_3O_4 TEM of 70 nm Si NTs a) empty Si NTs, b) Si NTs loaded with 5nm Fe_3O_4 , c)) Si NTs loaded with 8 nm Fe_3O_4 .

4.5.2. T₁ and T₂ measurements

To assess the potential use of these new nanotube-based materials as MRI contrast agents, their T₁ and T₂ values are evaluated using a relaxometer (Bruker Minispec mq60) at 1.41 Tesla (T). These values were measured in both DI water and PBS solutions at 37 °C. Data is analyzed for a possible linear dependence between the inverse proton relaxation times and the iron concentration according to the following equation:

$$\frac{1}{T_{i,obs}} = \frac{1}{T_{i,0}} + r_i [Fe] \quad (15)$$

where $1/T_{i,obs}$ ($i = 1, 2$) is the inverse relaxation time measured experimentally in the presence of the magnetic nanomaterial, $1/T_{i,0}$ is the inverse relaxation time of pure water in the absence of the contrast agent, $[Fe]$ is the iron concentration in the contrast agent and r_i is the longitudinal ($i = 1$) or transverse ($i = 2$) relaxivity (i.e. proton relaxation rate enhancement per mM Fe cation concentration).¹³⁰

Representative plots are shown in Figures 51 and 52 for $1/T_2$ vs iron concentration for all samples. Similar plots were undertaken for $1/T_1$, as illustrated in Figure 53.

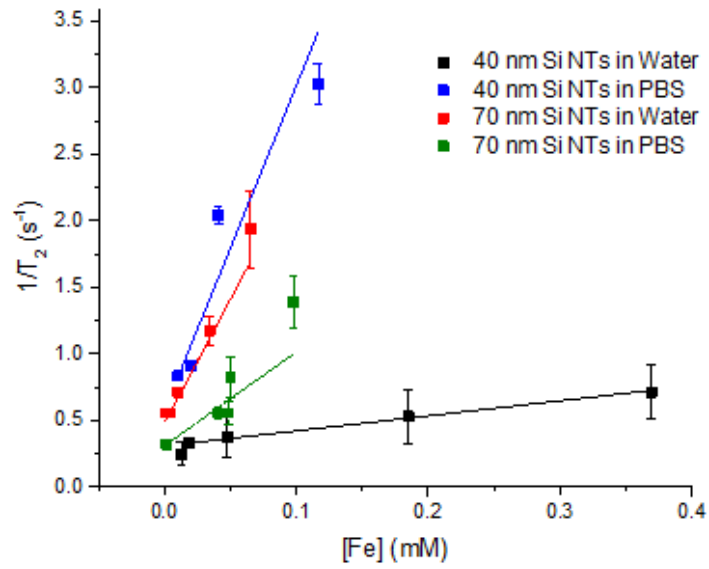


Figure 51: Plots of T_2 vs Fe concentration for 5 nm Fe_3O_4 NPs in 40 nm and 70 nm wall thickness Si NTs in PBS and water.

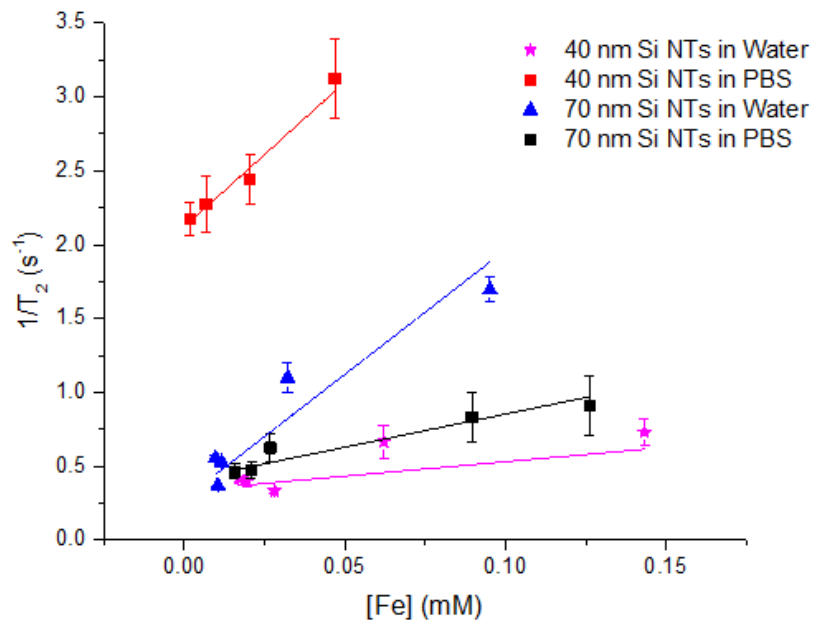


Figure 52: Plots of T_2 vs Fe concentration for 8 nm Fe_3O_4 NPs in 40 nm and 70 nm wall thickness Si NTs in PBS and water.

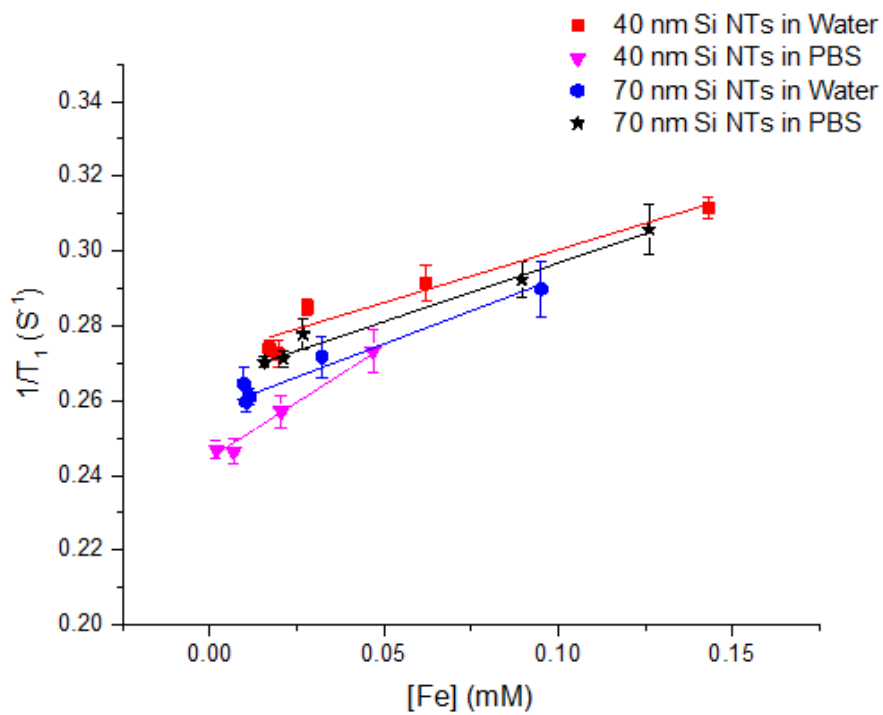
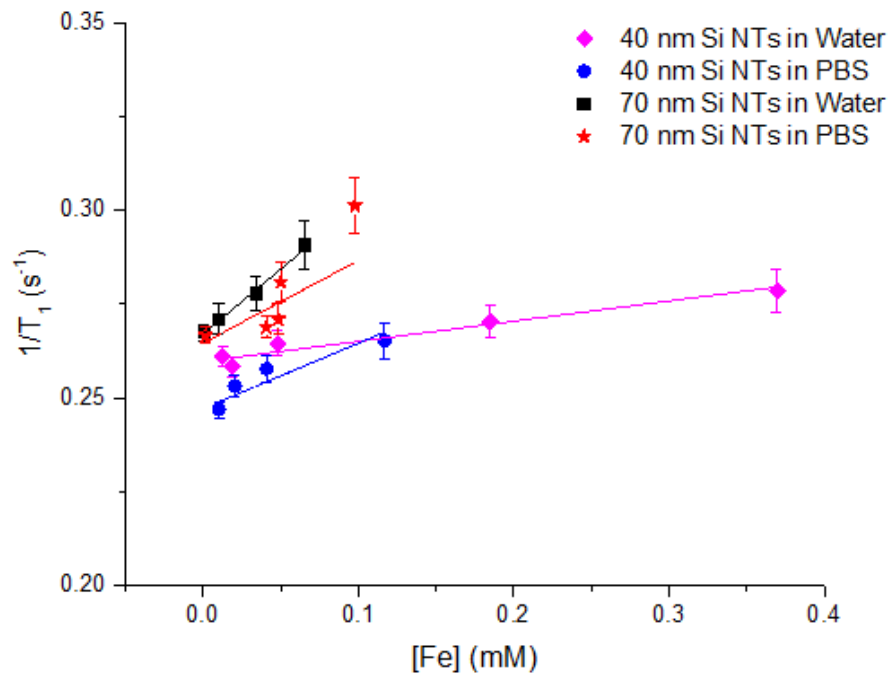


Figure 53: Plots of T_1 vs Fe concentration for 5 and 8 nm Fe_3O_4 NPs in 40 nm and 70 nm wall thickness Si NTs in PBS and water.

From linear fits of the above plots, we can calculate r_1 and r_2 from the slopes; these r_1 and r_2 values are shown in Table 4, as well as the corresponding r_2/r_1 ratios. r_1 is in the range of 0.05 – 0.35 $\text{mM}^{-1}\text{s}^{-1}$. Some trends are observed: r_2 is consistently larger in PBS samples versus those in DI water. For the Si NTs with a 40 nm wall thickness, r_2 for 5 nm Fe_3O_4 NPs = 1.18 $\text{mM}^{-1}\text{s}^{-1}$ in water and 50.59 $\text{mM}^{-1}\text{s}^{-1}$ in PBS; the same trend emerges for Si NTs loaded with 8 nm Fe_3O_4 , with a r_2 value of 2.90 $\text{mM}^{-1}\text{s}^{-1}$ in water and 21.05 $\text{mM}^{-1}\text{s}^{-1}$ in PBS. The opposite effect is observed for 70 nm wall Si NTs, as r_2 is bigger in water than in PBS: for example, nanotubes with 5 nm Fe_3O_4 NPs show a r_2 value of 21.74 $\text{mM}^{-1}\text{s}^{-1}$ in water and 11.31 $\text{mM}^{-1}\text{s}^{-1}$ in PBS. Again the same trend appears for 8 nm Fe_3O_4 NPs with a r_2 of 14.33 $\text{mM}^{-1}\text{s}^{-1}$ in water and 3.96 $\text{mM}^{-1}\text{s}^{-1}$ in PBS.

Table 4: r_1 , r_2 , and r_2/r_1 values associated with Fe_3O_4 NPs loaded in different Si NTs.

| 5 nm Fe_3O_4 in: | r_1 ($\text{mM}^{-1}\text{s}^{-1}$) | r_2 ($\text{mM}^{-1}\text{s}^{-1}$) | r_2/r_1 | 8 nm Fe_3O_4 in: | r_1 ($\text{mM}^{-1}\text{s}^{-1}$) | r_2 ($\text{mM}^{-1}\text{s}^{-1}$) | r_2/r_1 |
|--|--|--|-----------------------------|--|--|--|-----------------------------|
| 40 nm wall Si NTs (PBS) | 0.15 | 20.59 | 138 | 40 nm wall Si NTs (PBS) | 0.62 | 21.05 | 35 |
| 70 nm wall Si NTs (PBS) | 0.37 | 11.31 | 30 | 70 nm wall Si NTs (PBS) | 0.31 | 3.96 | 12 |
| 40 nm wall Si NTs (water) | 0.05 | 1.18 | 23 | 40 nm wall Si NTs (water) | 0.29 | 2.90 | 10 |
| 70 nm wall Si NTs (water) | 0.38 | 21.74 | 57 | 70 nm wall Si NTs (water) | 0.33 | 14.33 | 43 |

To interpret the above trends, it is useful to examine the following size dependent expression for

T_2 :¹³¹

$$\frac{1}{T_2} = \left(\frac{256\pi^2\gamma^2}{405} \right) \frac{V^*M_S^2a^2}{D\left(1+\frac{L}{a}\right)} \quad (16)$$

Where:

γ = gyromagnetic ratio

V^* = volume fraction

a = radius of iron oxide core

D = diffusivity of water molecules

L = thickness of an impermeable surface coating

In looking at the above results, it appears that for samples in PBS, the changes in T_2 values are dictated by thickness of surface coating. T_2 relaxivity decreases as the Si NTs becomes thicker, and thicker Si NTs are less permeable. For samples in water, it appears that T_2 changes are dominated by the diffusivity term. In this case r_2 relaxivity increases as the diffusivity of the water molecules are relatively less in a thicker walled nanotube. It is difficult to imagine, however, a scenario whereby thickness of surface coating does not influence diffusivity, and vice versa. Resolution of this dichotomy will likely require further analysis and/or investigation.

It is useful to compare those values with representative data from the existing literature. For example, for samples reported in water, Zhou obtained a r_1 value for 5 nm Fe_3O_4 coated with dimercaptosuccinic acid (DMSA) of $6.21 \text{ mM}^{-1}\text{s}^{-1}$, an r_2 of $39.53 \text{ mM}^{-1}\text{s}^{-1}$ and r_2/r_1 of 6.58 at 1.5 T).¹³² Huang et al reported that 5 nm Fe_3O_4 coated with sodium tartrate show a r_1 of $4.3 \text{ mM}^{-1}\text{s}^{-1}$, an r_2 of $23 \text{ mM}^{-1}\text{s}^{-1}$ and r_2/r_1 of 5.3.¹³³ Mamorufor and co-workers report that 8 nm Fe_3O_4 , coated with citric acid possesses a r_1 of $28.8 \text{ mM}^{-1}\text{s}^{-1}$, an r_2 of $54.4 \text{ mM}^{-1}\text{s}^{-1}$ and r_2/r_1 of 1.89.¹³⁴ It is important to consider that in our system, Fe_3O_4 NPs are not dispersed in the medium, Rather,

all Fe₃O₄ NPs are concentrated inside a given Si NT, but these Si NTs are well dispersed in the medium as a result of PEG (diacid) surface functionalization. Based on the data presented here, the very low values obtained for r_1 (in general $< 1 \text{ mM}^{-1}\text{s}^{-1}$) suggests that protons in a given medium do not have facile access to the surface of Fe₃O₄ NPs.

For this reason it is perhaps more appropriate to compare our system with clusters with similar sizes of Fe₃O₄ NPs previously reported.¹³⁵ Resovist®, commercially-available Fe₃O₄ NPs clusters coated with carboxydextran, have an overall diameter of 60 nm with an individual particle size of 4.6 nm; this cluster has a r_1 of $10.9 \text{ mM}^{-1}\text{s}^{-1}$, an r_2 of $190 \text{ mM}^{-1}\text{s}^{-1}$ and r_2/r_1 of 17.4.¹³⁶ Qin reported data for a cluster size of 71 nm with an individual particle size of 10.1 nm; this cluster is coated with Pluronic F127. These workers obtained a r_1 of $0.31 \text{ mM}^{-1}\text{s}^{-1}$, r_2 of $71 \text{ mM}^{-1}\text{s}^{-1}$ and r_2/r_1 of 229.¹³⁷ Tilborg and co-workers reported a cluster size of 62.4 nm coated with PEG2000 and individual particle size of 9 nm. A r_1 of $0.62 \text{ mM}^{-1}\text{s}^{-1}$, r_2 of $402.48 \text{ mM}^{-1}\text{s}^{-1}$ and r_2/r_1 of 647 was obtained for this system.¹³⁸ However the extremely high value of the latter system is probably due to the fact that the experiments were made at 9 T versus the 1.5 T used in our experiments. It should also be noted that those clusters are spherically-shaped aggregates of small spherical particles, in contrast to the rod-like structure of our nanotubes. However, in general the r_2/r_1 values we obtained are in the range of clusters previously reported.

4.6. Summary

In this chapter we show it is possible to load different sized iron oxide nanoparticles into Si NTs of varying wall thickness. TEM measurements show an effective loading of the NPs into the nanotubes. A negligible coercivity at room temperature (meaning that magnetization of the

samples vanishes if the applied magnetic field is turned off.), coupled with very low blocking temperatures in these materials, suggests suitability for magnetic field-assisted drug delivery in biological environments. Silicon nanotubes filled with superparamagnetic iron oxide NPs were investigated with respect to use these materials as a possible MRI contrast agent. All Fe₃O₄ NP samples loaded into SiNTs showed a relaxivity ratio $r_2/r_1 > 2$, putting them in the category of negative contrast agent.

Chapter V

Perovksite Formation Dictated by Silicon Nanotube Templates

5.1. Introduction

Solar energy is one of the most abundant and clean sources of energy on our planet. In order to use solar energy, efficient devices using the photovoltaic effect must be created.¹³⁹ Extensive research has been done on solar cells comprised of silicon, Cadmium Telluride (CdTe), and Copper Indium Gallium Arsenide ($\text{CuIn}_x\text{Ga}_{1-x}\text{Se}_2$, or CIGS), with the invention of the first modern solar cell made of silicon by Russel Ohl in 1946.¹⁴⁰ Later Michael Gratzel introduced the concept of a dye-sensitized solar cell (DSSC); this type of solar cell uses a strongly absorbing dye molecule between two electrodes usually TiO_2 and NiO. Photons striking the dye with enough energy to be absorbed create an excited state of the dye, from which an electron can be "injected" directly into the conduction band of the TiO_2 .¹⁴¹

With subsequent extensive research to find new dye molecules for DSSCs, a new hybrid organic-inorganic was investigated, in this case using perovskites. Perovskites are classified by unit cell type, being the same family of materials as those possessing a calcium titanate crystal structure. Organometal Perovskites have the formula ABX_3 where X is the halide anion and A and B are the cations ($X = \text{Cl, Br, I}$; $B = \text{Pb, Sn}$; and $A = \text{Methyl ammonium (MA) or Formamidinium (FA)}$). For photovoltaic applications, the advantages of these materials are: 1) a favorable band gap (1.5-1.65 eV);¹⁴² 2) high electron and hole mobilities and associated diffusion lengths;¹⁴³ 3) chemical tunability;¹⁴⁴ and 4) relatively easy processing.¹⁴⁵ These properties make this type of material an ideal candidate for applications in photovoltaics,¹⁴⁶ lasers,¹⁴⁷ LEDs¹⁴⁹ and photodetectors.¹⁵⁰

Miyasaka and coworkers reported the first perovskite based solar cell in 2006 in a conference paper; the first peer-reviewed article appeared in 2009.¹⁵⁰ As we can see in Figure 54,

great progress has been achieved in perovskite-based solar cells in the last few years; in a short time span, perovskite-based solar cells are in a position to compete with silicon.¹⁵¹

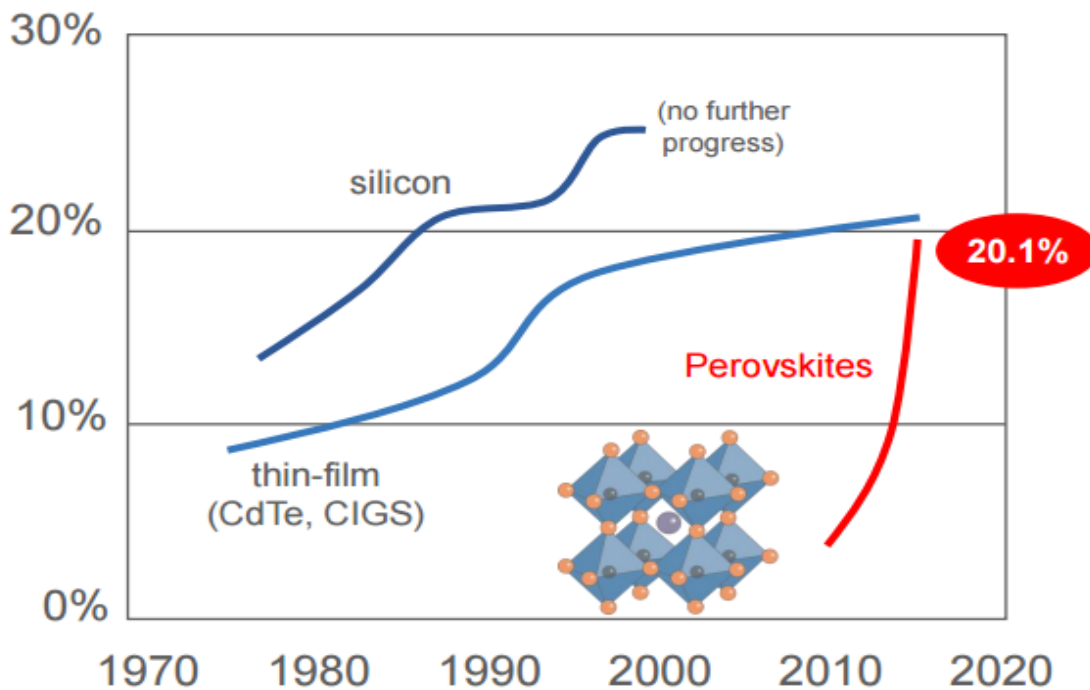


Figure 54: Solar cell efficiencies for different systems. Adapted from Ref. 151.

In photovoltaic applications, the most common morphologies are thin films,¹⁵⁰ nanowires¹⁵³ and nanoparticles,¹⁵⁴ but most of the reports are based on thin films, and problems with morphology control in such structures still persist. Si NTs are a good candidate to use as a template for perovskite formation, since as mentioned earlier, Si NTs dimensions can be controlled in terms of their inner diameter and length. In turn, these dimensions will ideally dictate the dimensions of the perovskite structure. In addition, it should be emphasized that Si NTs are compatible with the current processing steps of silicon device technology.

In this chapter I am going to discuss the formation of methyl ammonium lead halide perovskite structures inside Si NTs, along with bulk perovskite formation in the form of microwires and cubes, as well as their morphological and photoluminescent (PL) characterization. Some preliminary investigations with regard to mixed halide structures (Iodide-Bromide and Bromide-Chloride) of the above methyl ammonium lead perovskites will also be presented.

5.2. Experimental

Loading of the Si NTs with perovskite ($\text{CH}_3\text{NH}_3\text{PbI}_3$) is achieved by preparing a 1:1 solution of $\text{CH}_3\text{NH}_3\text{I}$ and PbI_2 at a concentration of 2.06×10^{-3} M in DMF. Si NTs arrays (on FTO glass or Si wafer pieces) are soaked into the solution for 2 h at 60 °C, then spun at 6000 for 40 s, followed by baking the sample for 30 min at 95 °C. This process is repeated three times for a uniform coating. Perovskite microwires (or microcubes, in the case of bromide/chloride containing species) are prepared by placing 1 drop of a solution 1:1 of $\text{CH}_3\text{NH}_3\text{I}$ and PbI_2 (6.18×10^{-3} M each) in DMF. After air drying, the sample is heated for 30 min at 95 °C. All samples are stored in a desiccator. In Figure 55, the procedures for perovskite nanostructure formation and perovskite microwires (uw) are shown. Table 5 presents the range of target mole ratios of reactants used in the perovskite nanostructure fabrication experiments carried out in this chapter using 30, 70, and 200 nm inner diameter (ID) Si NTs and microstructures as templates.

Table 5: Mole ratios of precursors used for perovskite formation.

| Mol ratio | | | | |
|------------------|-------------------|-----------------------------------|------------------------------------|--|
| PbI ₂ | PbBr ₂ | CH ₃ NH ₃ I | CH ₃ NH ₃ Br | |
| 1 | 0 | 1 | 0 | CH ₃ NH ₃ PbI ₃ |
| 1 | 0 | 0.75 | 0.25 | CH ₃ NH ₃ PbI _{2.75} Br _{0.25} |
| 1 | 0 | 0.5 | 0.5 | CH ₃ NH ₃ PbI _{2.5} Br _{0.5} |
| 1 | 0 | 0.25 | 0.75 | CH ₃ NH ₃ PbI _{2.25} Br _{0.75} |
| 1 | 0 | 0.1 | 0.9 | CH ₃ NH ₃ PbI _{2.10} Br _{0.90} |
| 1 | 0 | 0 | 1 | CH ₃ NH ₃ PbI ₂ Br ₁ |
| 0 | 1 | 0 | 1 | CH ₃ NH ₃ PbBr ₃ |
| 0 | 1 | 0.5 | 0.5 | CH ₃ NH ₃ PbI _{0.5} Br _{2.5} |
| 0 | 1 | 1 | 0 | CH ₃ NH ₃ PbI ₁ Br ₂ |
| 0.17 | 0.83 | 0.17 | 0.83 | CH ₃ NH ₃ PbI _{0.5} Br _{2.5} |
| 0.25 | 0.75 | 0.25 | 0.75 | CH ₃ NH ₃ PbI ₁ Br ₂ |
| 0.50 | 0.50 | 0.50 | 0.50 | CH ₃ NH ₃ PbI _{1.5} Br _{1.5} |
| 0.75 | 0.25 | 0.75 | 0.25 | CH ₃ NH ₃ PbI _{2.25} Br _{0.75} |

Photoluminescence (PL) measurements of these perovskite nanostructures were carried out by Neta Arad-Vosk, Naama Rozenfeld, and Professor Amir Sa'ar at the Racah Institute of Physics at the Hebrew University of Jerusalem. For such measurements, the samples were excited by an Ar⁺ ion laser operating at 488 nm, while the PL signal was dispersed with a 1/4-m monochromator and detected by a photomultiplier tube (PMT). During PL experiments, the samples were kept under vacuum in a continuous-flow liquid helium optical cryostat that allows temperature control over the 4.5 K to 300 K range. The samples were first cooled down to 4.5 K and then heated up gradually back to room temperature.

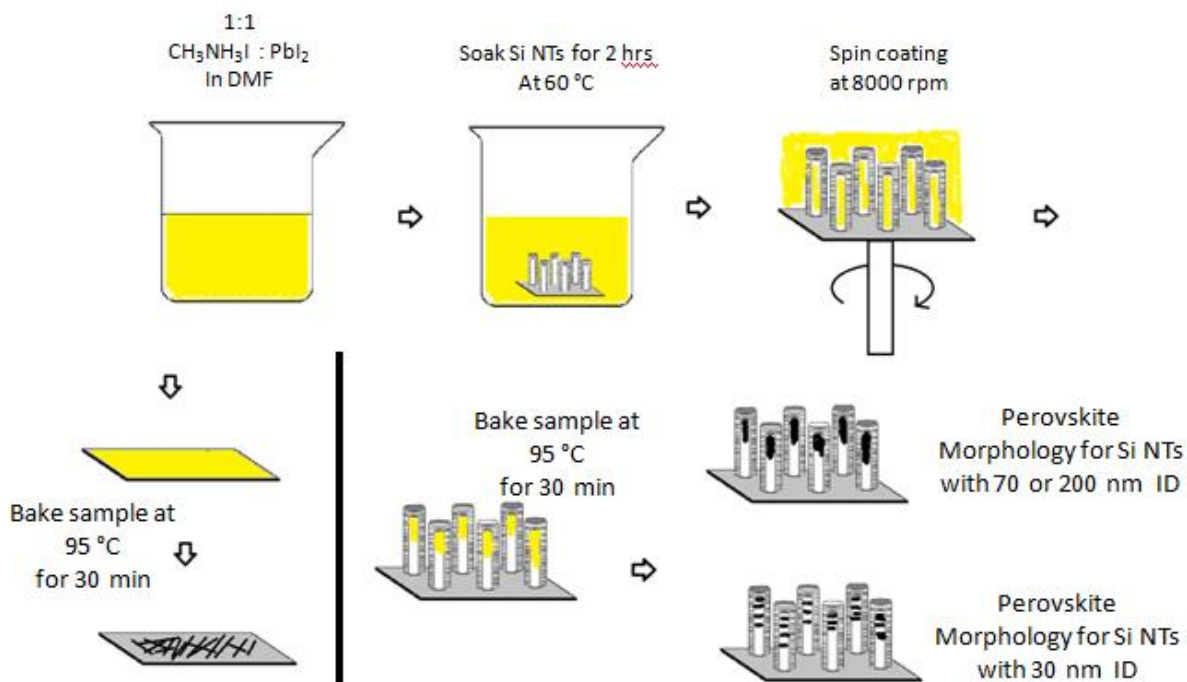


Figure 55: Procedure for perovskite formation inside Si NTs; on the left, the procedure for perovskite microwires/cubes formation.

5.3. Results and Discussion

5.3.1. Morphological characterization

In these experiments, it is necessary to have a ‘bulk-like’ one dimensional control perovskite structure of CH₃NH₃PbI₃ for proper structural and photophysical comparison. Use of relatively concentrated precursor solutions in conjunction with spin coating and thermal annealing produces large microwires. SEM characterization of these CH₃NH₃PbI₃ microwires reveal a diameter of approximately 8 μ m and lengths up to a few millimeters. Figure 56 shows a typical SEM image of these microwires formed on a Si wafer.

In Figure 57, typical SEM images are shown for 30, 70 and 200 nm ID Si NTs, both with and without the presence of CH₃NH₃PbI₃. There is a clear contrast change at the tip of Si NTs due to the presence of perovskite formed inside Si NTs.

In Figure 58, typical TEM images for 30, 70 and 200 nm ID Si NTs the images show empty and $\text{CH}_3\text{NH}_3\text{PbI}_3$ filled Si NTs, we observe a concentration of perovskite again at the tip of the Si NTs for all cases. Typical perovskites length is ~ 300 nm (± 250 nm) in the case of structures formed within 70 nm and 200 nm ID Si NTs. It should be pointed out that the $\text{CH}_3\text{NH}_3\text{PbI}_3$ formed within 30 nm ID Si NTs are relatively unstable in the focused electron beam (200 kV) of our TEM and thus preclude detailed analysis for this particular sample.

The presence of Pb and I associated with $\text{CH}_3\text{NH}_3\text{PbI}_3$ was also confirmed by EDX. EDX in line scan mode (Figure 59) shows a 70 nm inner diameter (ID) Si NT empty and one loaded with $\text{CH}_3\text{NH}_3\text{PbI}_3$. The empty Si NT shows the characteristic ‘double-hump’ Si peak that is expected for Si NTs. When $\text{CH}_3\text{NH}_3\text{PbI}_3$ is present in the Si NT, the line scan clearly shows Pb and I intensity in the middle of the ‘double-hump’ lineshape.

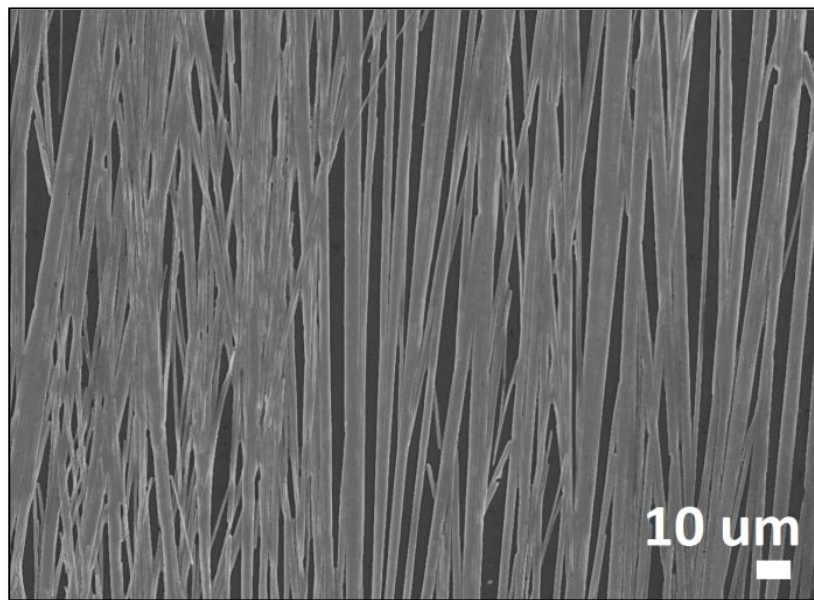


Figure 56: SEM image of $\text{CH}_3\text{NH}_3\text{PbI}_3$ microwires.

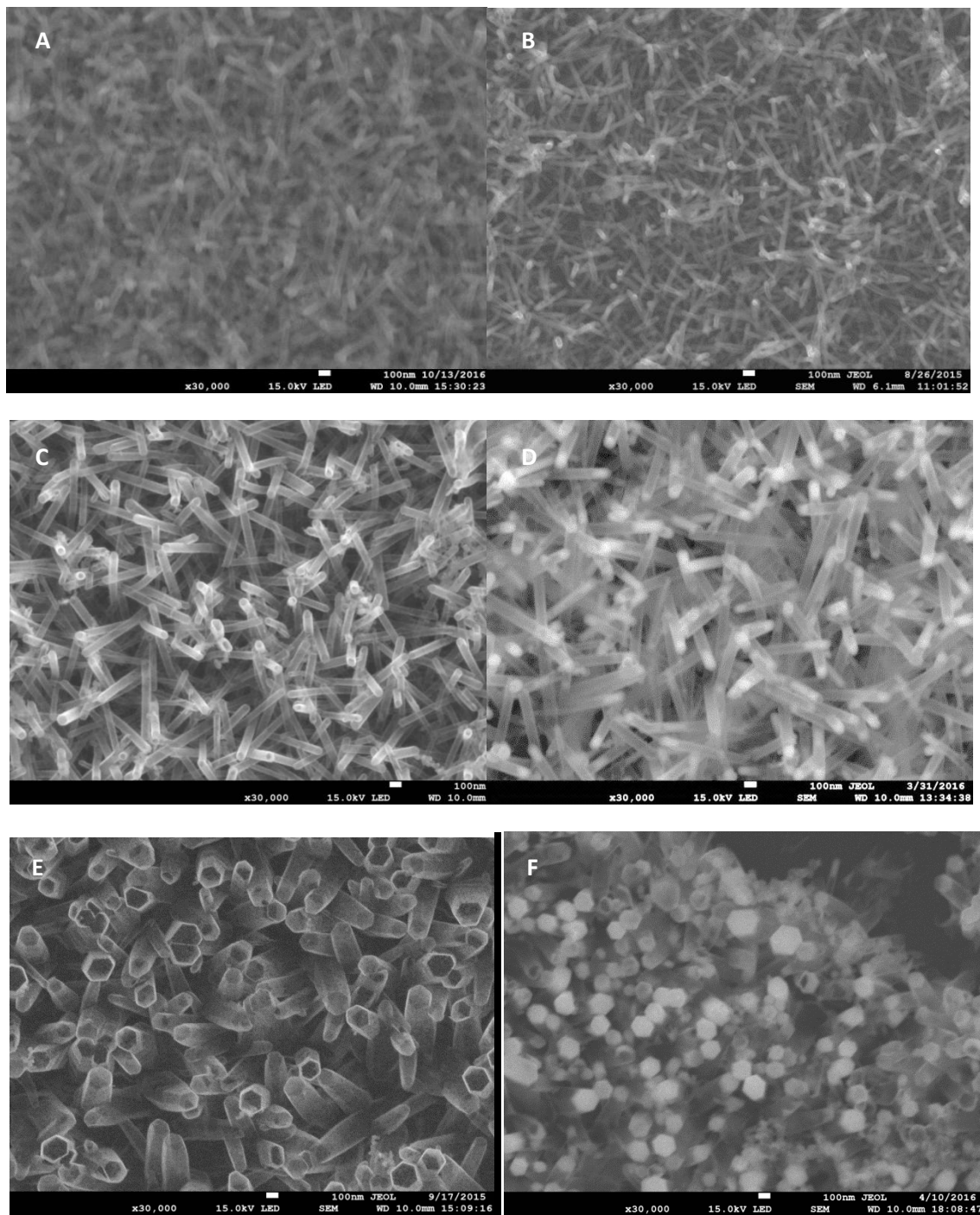


Figure 57: SEM for empty Si NTs in: a) 30 nm ID Si NTs, c) 70 nm ID Si NTs, e) 200 nm ID Si NTs. SEM of $\text{CH}_3\text{NH}_3\text{PbI}_3$ filled Si NTs in: b) 30 nm ID Si NTs, d) 70 nm ID Si NTs, f) 200 nm ID Si NTs.

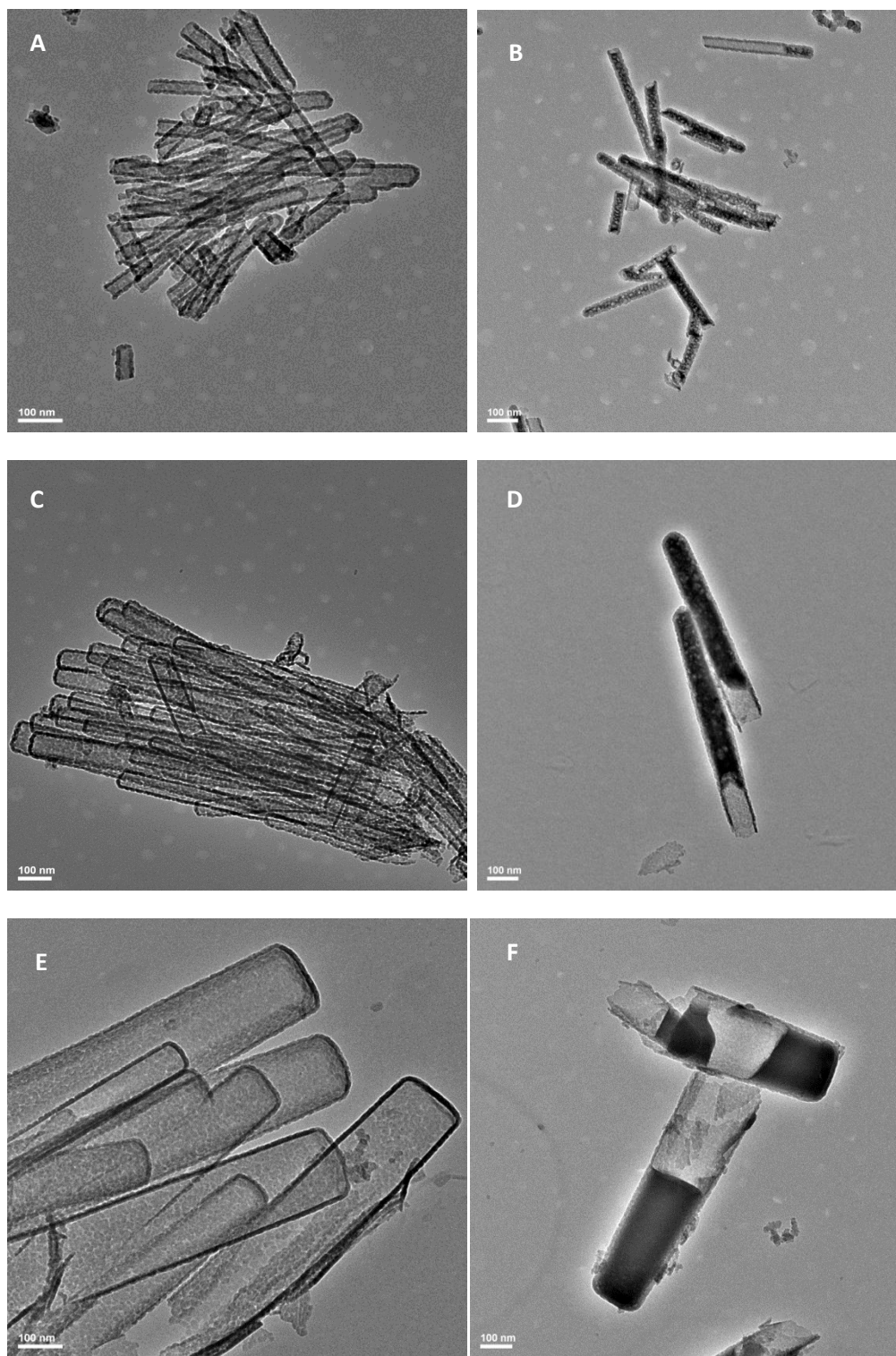


Figure 58: TEM for empty Si NTs in: a) 30 nm ID Si NTs, c) 70 nm ID Si NTs, e) 200 nm ID Si NTs. TEM of CH₃NH₃PbI₃ filled Si NTs in: b) 30 nm ID Si NTs, d) 70 nm ID Si NTs, f) 200 nm ID Si NTs.

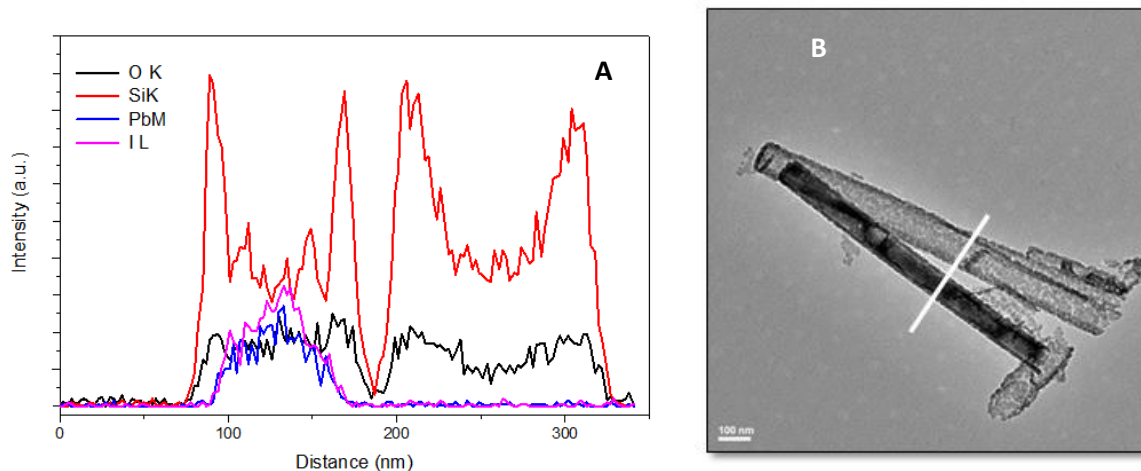


Figure 59: a) EDX-TEM line scan of 70 nm ID Si NTs, b) TEM image associated with the EDX-TEM line scan.

High resolution lattice imaging (HRTEM) of a typical sample of $\text{CH}_3\text{NH}_3\text{PbI}_3$ formed within the 70 nm Si NTs (Figure 60) shows a lattice spacing of 0.31 nm, consistent with the (220) orientation of tetragonal $\text{CH}_3\text{NH}_3\text{PbI}_3$; spacings of 0.63 nm associated with the (002) orientation are also evident. Selected area electron diffraction (in the form of a fast Fourier transform (FFT)) is consistent with polycrystalline character in this sample.

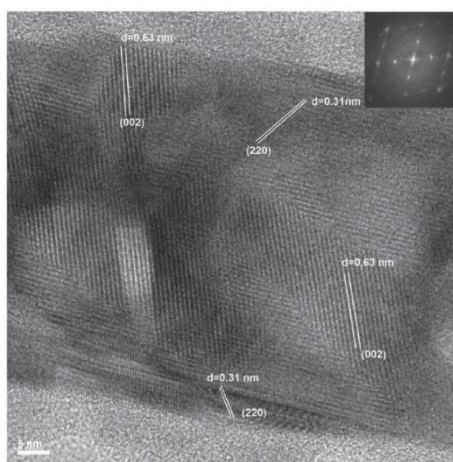


Figure 60: HRTEM for 70 nm ID SiNTs loaded with $\text{CH}_3\text{NH}_3\text{PbI}_3$. Lattice spacings associated with both the (002) and (220) directions are shown. Inset: FFT of selected area.

5.3.2. PL Characterization

Room temperature fluorescence imaging shows a relatively uniform visible red emission from these perovskite nanostructures confined within the SiNTs as well as the individual microwires (Figure 61).

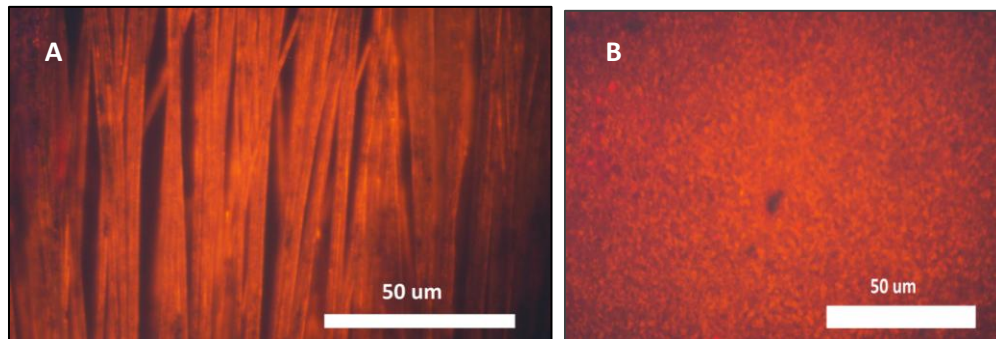


Figure 61: Large area fluorescence image of a) $\text{CH}_3\text{NH}_3\text{PbI}_3$ microwires, b) 70 nm ID Si NTs with $\text{CH}_3\text{NH}_3\text{PbI}_3$.

Room-temperature PL (solid lines in Figure 9a; $\lambda_{\text{ex}} = 488 \text{ nm}$), absorbance spectra (dashed lines in Figure 63a), and a first derivative of the absorbance (Figure 62b) are shown in Figure 9 for the 70 and 200 nm perovskite-loaded SiNTs together with larger perovskite microwires, grown on either Si (for PL) or FTO (for absorption measurements). The results clearly indicate a correlation between the emission spectra (PL) and the onset of the absorption as can also be appreciated from the correlation between the PL maximum and the absorption derivatives. The spectra (both PL and absorption) of the 200 nm perovskite-loaded Si NTs seem to be similar to that of the reference perovskite microwires, with a slight shift toward the blue of about 5–10 meV, and an additional blue shift of about 10–15 meV for the 70 nm perovskite-loaded Si NTs. This result might be attributed to quantum size effects in these 1D perovskite nanorods but can also be a consequence of the large stress at the silicon-perovskite interface and a larger surface-to-volume ratio for $\text{CH}_3\text{NH}_3\text{PbI}_3$ formed within the smaller Si NTs.

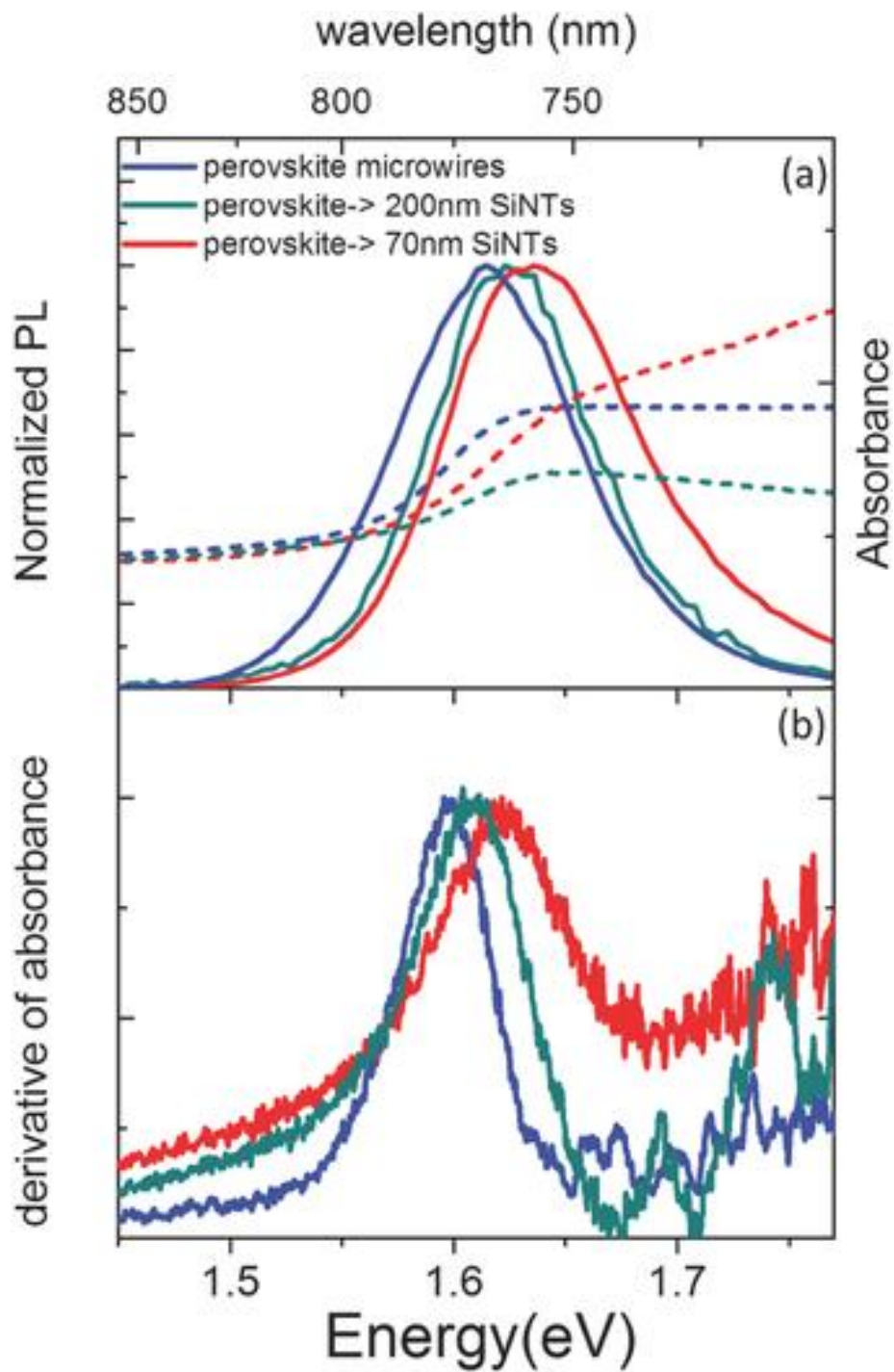


Figure 62: PL (solid lines) and absorption (dashed lines) spectra for 200 nm (in green), 70 nm (in red) diameter perovskites loaded into SiNTs, and perovskite microwires (in blue); b) the absolute value of the first derivative of the absorbance.

Figure 63 shows PL spectra for the 70 nm perovskite-loaded Si NTs and the bulk perovskite microwires at different temperatures from 295 K down to 4 K. Very similar spectra to those of the perovskite microwires have been measured for the 200 nm perovskite-loaded Si NTs.¹⁵³ In general, the PL spectra are redshifted to lower energies with the decreasing temperatures down to about 140 K. Below that temperature, an additional high-energy peak can be observed. This high-energy peak, in the range of 1.68–1.7 eV, has been observed and reported for thin films of perovskites and assigned to the orthorhombic phase of $\text{CH}_3\text{NH}_3\text{PbI}_3$.¹⁵⁶

The appearance of the high-energy peak below 140 K is a manifestation of structural phase transition (from the tetragonal to the orthorhombic phase), which emerges around that temperature. At these low temperatures, a much weaker high-energy peak seems to characterize the smaller diameter perovskite-loaded Si NTs, which could be an indication of the influence of the size and the dimensionality of the perovskite nanorods on the phase transition. Subsequent analysis and verification of this size dependent suppression of this phase transition in perovskite nanostructures formed within 30 nm ID SiNTs by the Saar group at the Hebrew University suggests that the significant c-axis distortion anticipated for the orthorhombic phase of this perovskite results in an energetic stabilization of the tetragonal structure in such small nanostructures.¹⁵⁷

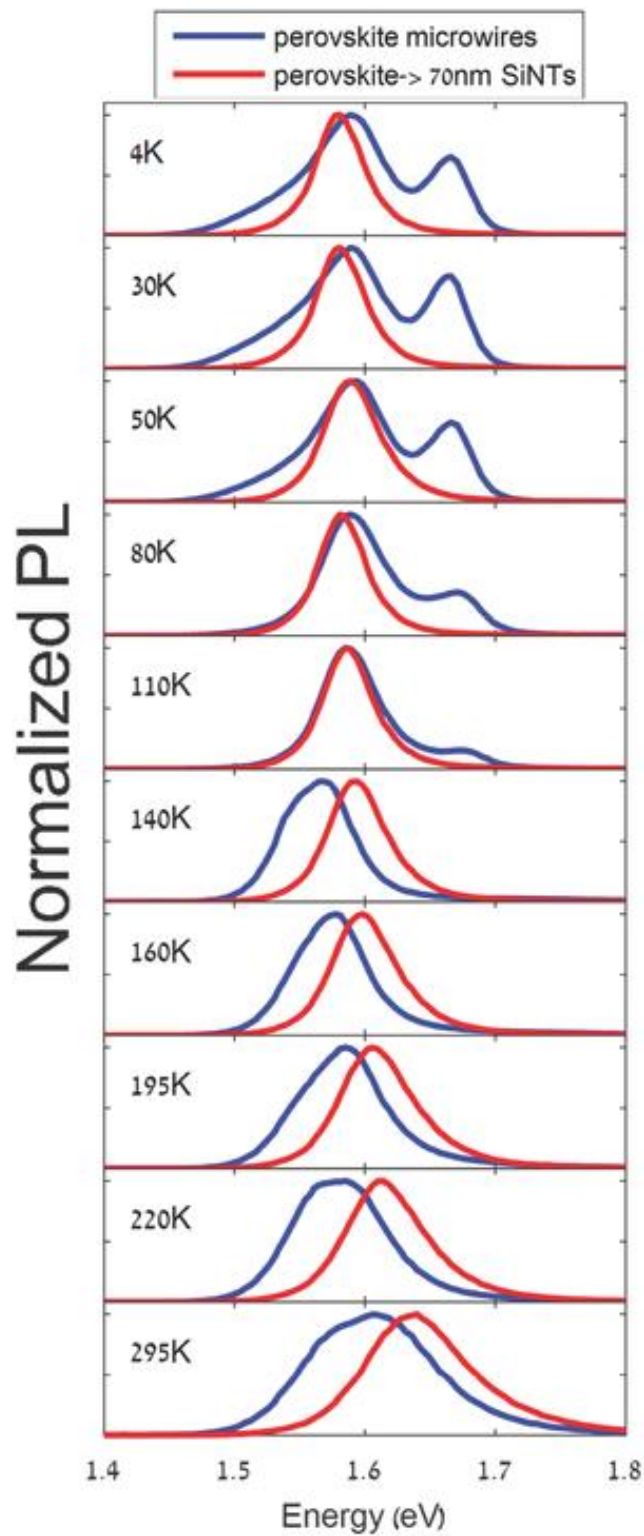


Figure 63: PL spectra from room temperature down to 4 K for the perovskite nanostructures 70 nm in diameter, along with perovskite microwires.

5.4. Bromide-Iodide systems

In order to investigate the optical properties of mixed Bromide-Iodide perovskite nanostructures, the necessary precursors (in this case PbBr_2 , PbI_2 , $\text{CH}_3\text{NH}_3\text{Br}$, and $\text{CH}_3\text{NH}_3\text{I}$) were combined at different ratios according to those listed in Table 4. We begin with the case of the pure bromide-containing perovskite structure in the bulk phase. Figure 64 shows a SEM image of $\text{CH}_3\text{NH}_3\text{PbBr}_3$ microcubes (uc). Unlike the pure iodide-containing microwires, use of the Br precursors under the same precursor concentrations, spin coating, and drying conditions leads to uc formation rather than microwires.

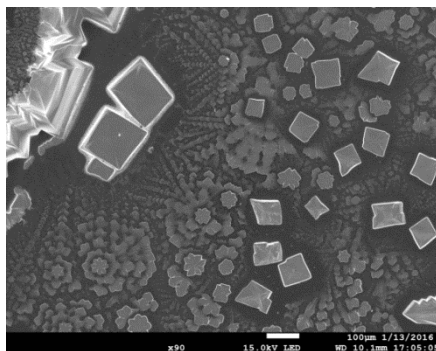


Figure 64: SEM image of $\text{CH}_3\text{NH}_3\text{PbBr}_3$ microcubes.

We now shift our attention to mixed bromide-iodide perovskites formed inside SiNTs of varying width. In Figure 65 EDX line scans of 70 nm ID Si NT loaded with $\text{CH}_3\text{NH}_3\text{PbI}_{2.5}\text{Br}_{0.5}$ and the TEM associated with the line scan are presented. As with previous linescans of SiNTs, the typical double hump peak of the silicon signal confirms a tubular structure, with the anticipated Pb, Br and I signals are present between the double humps of the silicon peak, consistent with perovskite formation inside the silicon nanotubes. The relatively constant oxygen signal for the NTs is characteristic of native SiO_2 on the nanotube surface.

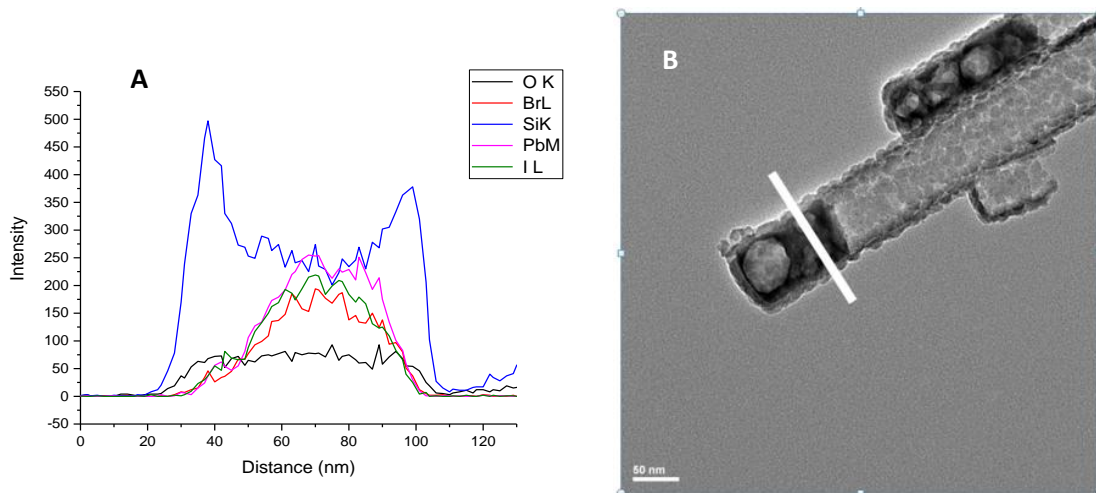


Figure 65: a) Line scan of $\text{CH}_3\text{NH}_3\text{PbI}_{2.5}\text{Br}_{0.5}$ and b) TEM image associated with the line scan.

Large area room temperature fluorescence imaging shows a relatively bright visible green emission of $\text{CH}_3\text{NH}_3\text{PbBr}_3$ microcube aggregates (Figure 66a). For the $\text{CH}_3\text{NH}_3\text{PbBr}_3$ nanostructures formed within 200 nm ID Si NTs (Figure 66b,c), confocal fluorescence imaging shows both a uniform green emission across the film, emanating from a three dimensional rod/wire type geometry.

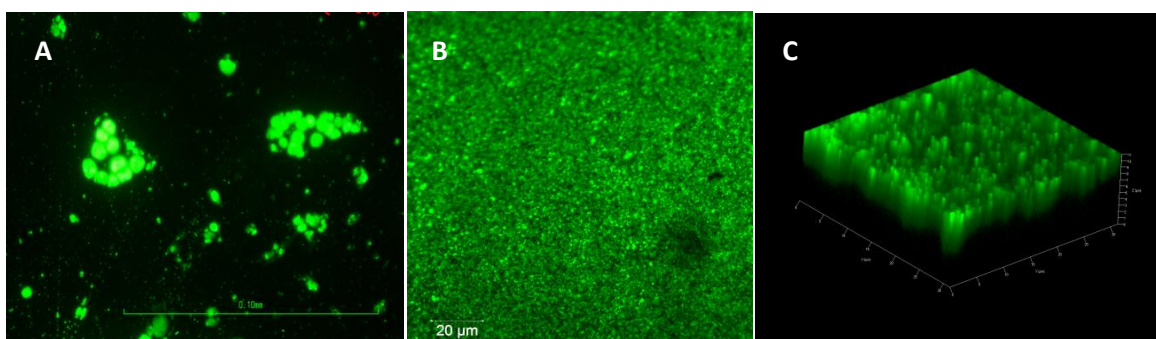
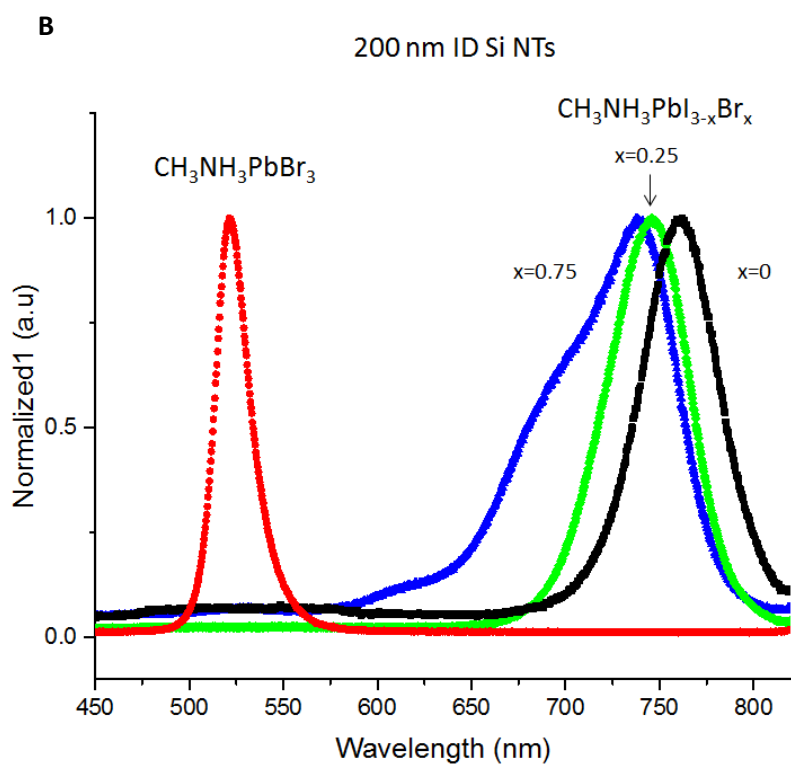
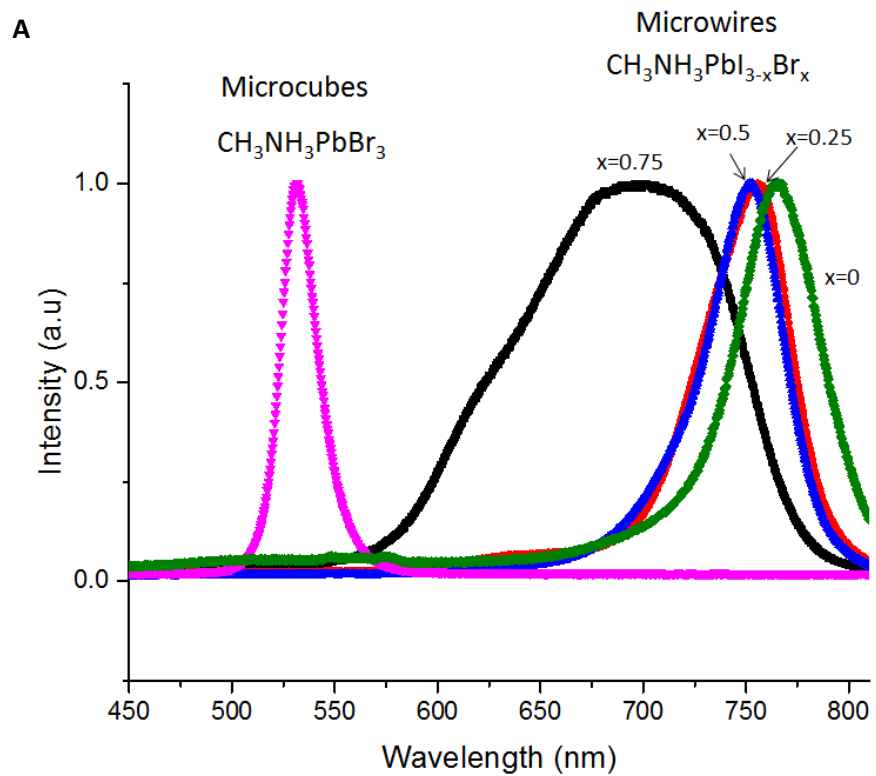


Figure 66: a) fluorescence image associated with $\text{CH}_3\text{NH}_3\text{PbBr}_3$ microcubes; b) confocal fluorescence image of $\text{CH}_3\text{NH}_3\text{Br}_3$ in 200 nm ID Si NTs. b) 3D scan taken by confocal fluorescence microscopy of $\text{CH}_3\text{NH}_3\text{Br}_3$ in 200 nm ID Si NTs.

In Figure 67, a series of PL spectra for the $\text{CH}_3\text{NH}_3\text{PbI}_{3-x}\text{Br}_x$ microcubes and Si NTs loaded with $\text{CH}_3\text{NH}_3\text{PbI}_{3-x}\text{Br}_x$ for inner diameters of 200, 70, and 30 nm are shown. In each type of template, it is clear that the overall PL maximum shifts to higher energy with increasing bromide content. Based on the literature, it is expected that the incorporation of increasing amounts of bromide in a $\text{CH}_3\text{NH}_3\text{PbI}_{3-x}\text{Br}_x$ system mainly affects the bandgap as a result of shifts of the valence band maximum (VBM) of this perovskite rather than the conduction band minimum (CBM).¹⁵⁸ This is a likely consequence of the fact that the CBM is comprised mainly of Pb-6p orbitals.¹⁵⁹

For the case of the perovskite microcubes and perovskites formed within the relatively large nanotubes (200 nm) when $x = 0.75$, the extreme broadness of the peak for these two materials leads to the likely conclusion that multiple perovskite structures are likely present in these particular samples.

Interestingly, when we analyze the spectral lineshape for the case of the mixed bromide-iodide perovskites formed within smaller ID SiNTs (70 nm and 30 nm), much narrower peaks - consistent with a more homogeneous nanoscale product - are observed (Fig 68c,d). This would suggest that the smaller SiNT reaction vessels kinetically trap a more homogeneous reaction product.



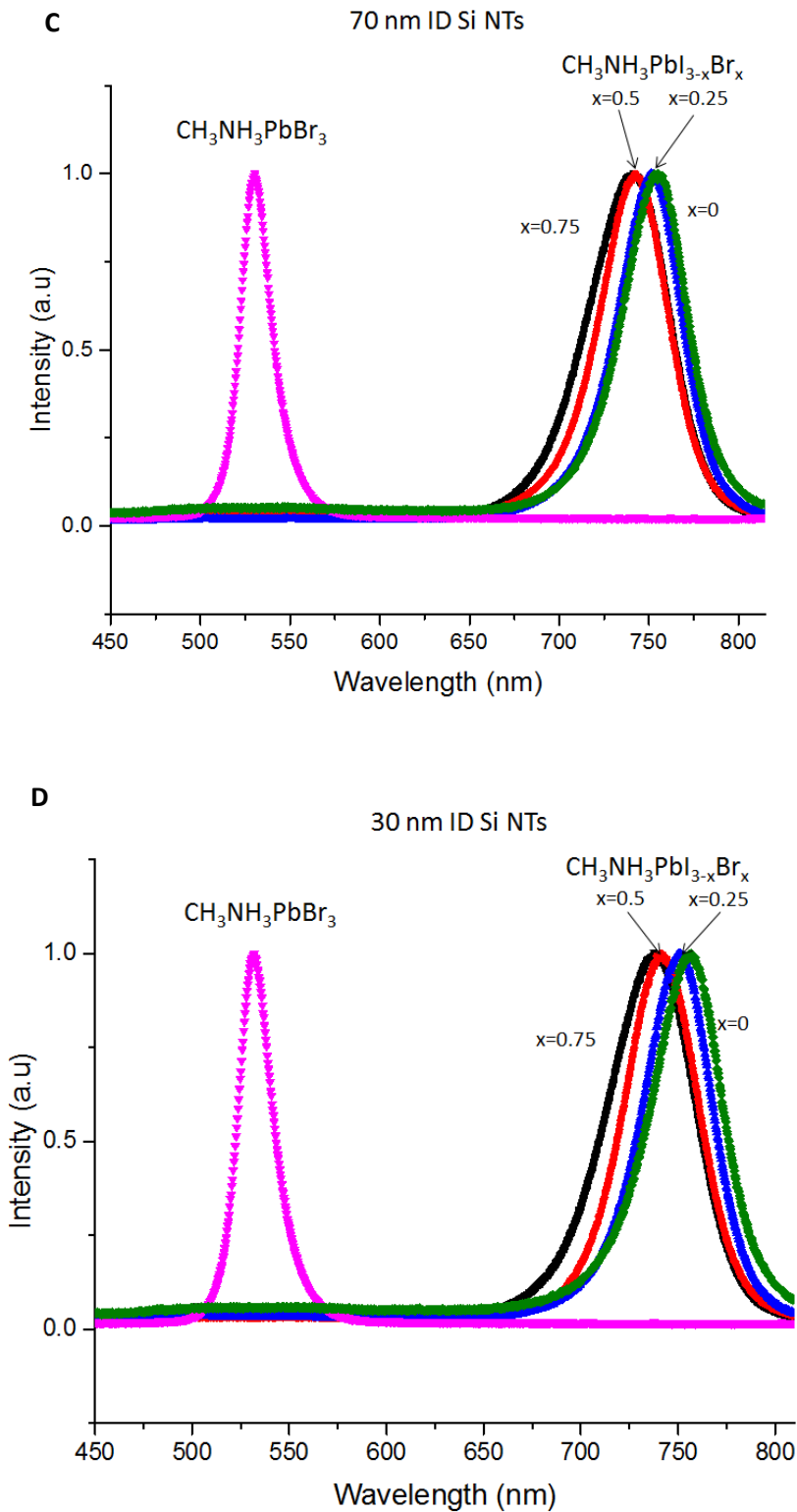


Figure 67: a) PL emission peaks of perovskite micro cubes/micro wires, b) PL of perovskite-loaded 200 nm ID Si NTs, c) PL of 70 nm ID Si NTs, c) PL of 30 nm ID Si NTs.

A complementary perspective of the above behavior occurs if we compare the PL max for the microcubes of $\text{CH}_3\text{NH}_3\text{PbI}_{2.25}\text{Br}_{0.75}$ with that of the $\text{CH}_3\text{NH}_3\text{PbI}_{2.25}\text{Br}_{0.75}$ formed in 200, 70, 30 nm ID Si NTs, the stoichiometry was (PbI_2 , $\text{CH}_3\text{NH}_3\text{I}$, $\text{CH}_3\text{NH}_3\text{Br}$ 1:0.25:0.75). There is a clear shift from the emission maximum of the microwires (bulk) of 689 nm to a PL of 725 nm for perovskite-loaded into 200 nm ID Si NTs, and a further blue shift to ca. 738 nm for these perovskites formed within Si NTs with 70 and 30 nm ID. Importantly, for each perovskite formed within a nanotube template, I to Br ratios closely match the predicted stoichiometry, again suggesting that the nanotubes facilitate kinetic entrapment of a more homogeneous composition for each; this is not the case for the non-templated microwire perovskite morphology, with the observed I/Br ratio presumably reflecting the broad distribution of reaction products in this case.

Table 6: SEM-EDX at % composition data for $\text{CH}_3\text{NH}_3\text{PbI}_{2.25}\text{Br}_{0.75}$ formed as microwires (\square_w) and inside Si NTs with 200 nm ID, 70 nm ID and 30 nm ID, as well as associated PL max in each case.

| X=0.75 | SEM-EDX (at%) | | | PL (nm) |
|---------------|----------------------|----------|-----------|----------------|
| | Pb | I | Br | Max |
| uw | 29.12 | 60.14 | 10.75 | 689 |
| 200 nm | 29.96 | 52.52 | 17.52 | 725 |
| 70 nm | 32.81 | 44.83 | 22.35 | 738 |
| 30 nm | 29.49 | 47.19 | 23.32 | 736 |

5.5. Bromide-Chloride systems

In a manner similar to I/Br perovskite structures, in order to investigate the optical properties of mixed Bromide-Chloride perovskite nanostructures, the necessary precursors (in

this case PbCl_2 , PbBr_2 , $\text{CH}_3\text{NH}_3\text{Br}$, and $\text{CH}_3\text{NH}_3\text{Cl}$) were combined at different ratios according to those listed in Table 6

Table 7: Mole ratios used for perovskite formation in Br-Cl systems.

| PbBr_2 | PbCl_2 | $\text{CH}_3\text{NH}_3\text{Br}$ | $\text{CH}_3\text{NH}_3\text{Cl}$ | |
|-----------------|-----------------|-----------------------------------|-----------------------------------|--|
| 0 | 1 | 1 | 0 | $\text{CH}_3\text{NH}_3\text{PbBr}_1\text{Cl}_2$ |
| 0 | 1 | 0 | 1 | $\text{CH}_3\text{NH}_3\text{PbCl}_3$ |
| 0 | 1 | 0.5 | 0.5 | $\text{CH}_3\text{NH}_3\text{PbBr}_{0.5}\text{Cl}_{2.5}$ |
| 1 | 0 | 0 | 2 | $\text{CH}_3\text{NH}_3\text{PbBr}_1\text{Cl}_1$ |
| 1 | 0 | 0 | 1.5 | $\text{CH}_3\text{NH}_3\text{PbBr}_1\text{Cl}_{0.75}$ |
| 0.5 | 0.5 | 0 | 1 | $\text{CH}_3\text{NH}_3\text{PbBr}_1\text{Cl}_2$ |

Figure 68 shows the characteristic SEM image of $\text{CH}_3\text{NH}_3\text{PbBr}_{0.5}\text{Cl}_{2.5}$ cubes (on a silicon wafer substrate) and 70 nm ID Si NTs loaded with $\text{CH}_3\text{NH}_3\text{PbBr}_{0.5}\text{Cl}_{2.5}$. The uniformity of perovskite loading in these Si NTs is comparable to that of those of the I and Br systems described above.

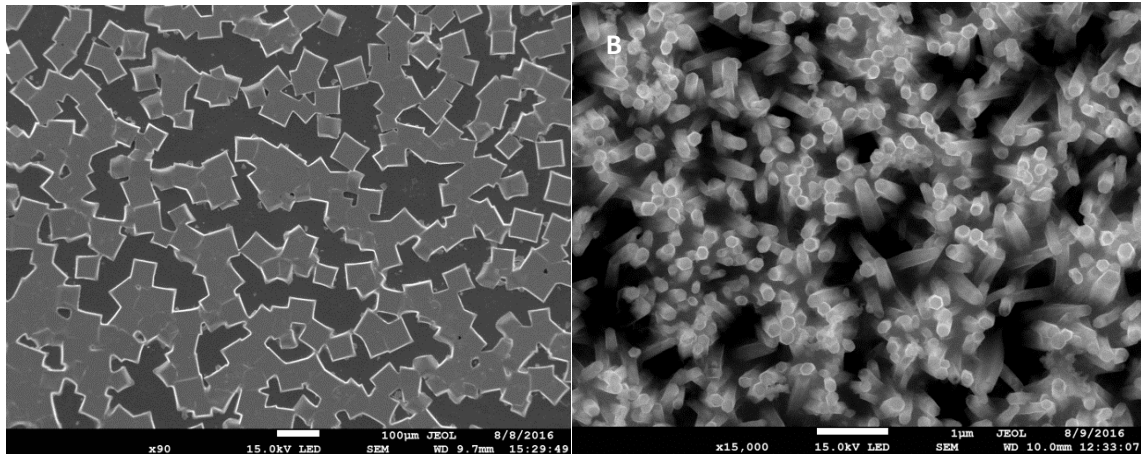


Figure 68: SEM Images of : a) $\text{CH}_3\text{NH}_3\text{PbBr}_{0.5}\text{Cl}_{2.5}$ cubes; and b) 70 nm ID Si NTs loaded with $\text{CH}_3\text{NH}_3\text{PbBr}_{0.5}\text{Cl}_{2.5}$

In order to evaluate the spatial distribution of Cl and Br in these nanostructures, a TEM-EDX map was recorded for 70 nm ID Si NTs loaded with $\text{CH}_3\text{NH}_3\text{PbBr}_{0.5}\text{Cl}_{2.5}$ (Figure 69). Cl,

Br and Pb each have a uniform distribution in the nanotube as well as relatively strong intensity in the EDX spectrum.

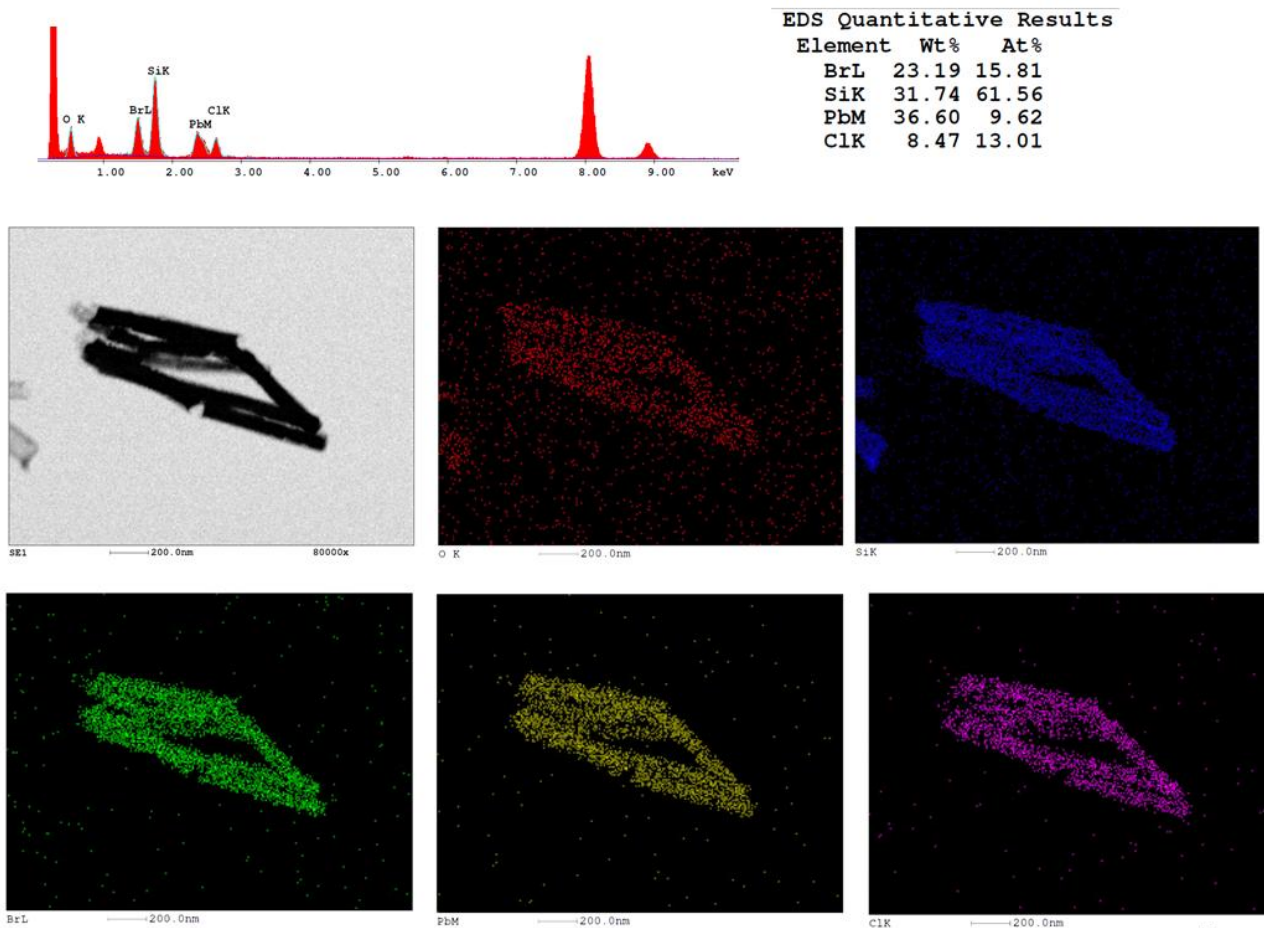


Figure 69: a) TEM-EDX map for 70 nm ID Si NTs loaded with perovskites.

In Figure 70 EDX line scans of 200 nm ID Si NT loaded with $\text{CH}_3\text{NH}_3\text{PbBr}_2\text{Cl}$ and the TEM associated with the line scan are presented. Peaks associated with Br and Cl are present in the middle of double-hump Si signal. In this system Cl appears as two peaks suggesting that Cl is present as two phases within the Si NTs or likely have a very high mobility under TEM conditions.

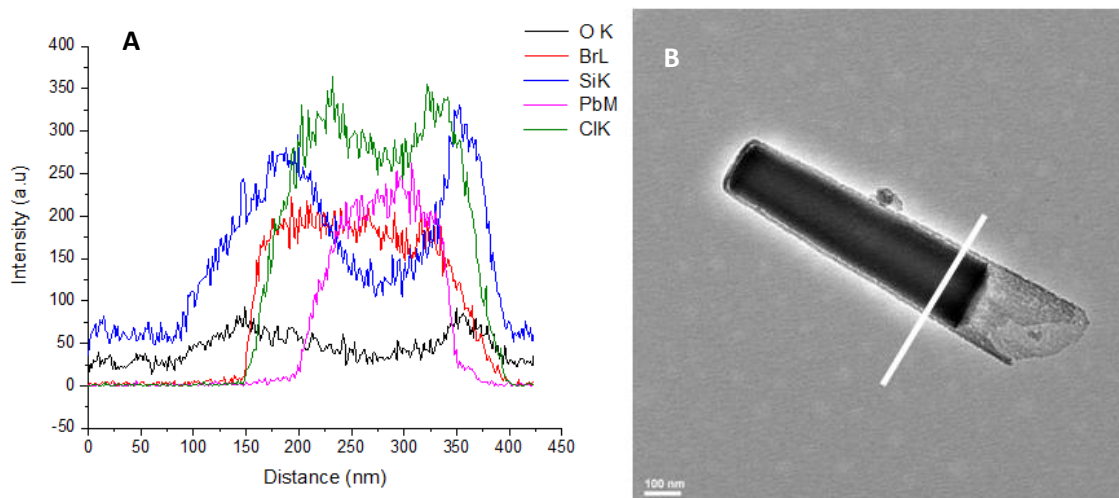


Figure 70: a) TEM-EDX lines scan of $\text{CH}_3\text{NH}_3\text{PbBr}_2\text{Cl}$ in 200 nm ID Si NT and b) TEM associate with line scan.

In terms of light emission for these mixed bromide-chloride perovskites, structures with high Cl content (e.g. $\text{CH}_3\text{NH}_3\text{PbBr}_{0.5}\text{Cl}_{2.5}$) demonstrate relatively blue emission, while that of pure bromide-containing phases is green. In Figure 71, fluorescence images of $\text{CH}_3\text{NH}_3\text{PbBr}_{0.5}\text{Cl}_{2.5}$ cubes are shown as well as 70 nm ID Si NTs loaded with $\text{CH}_3\text{NH}_3\text{PbBr}_{0.5}\text{Cl}_{2.5}$. The blue emission is uniform in both cases.

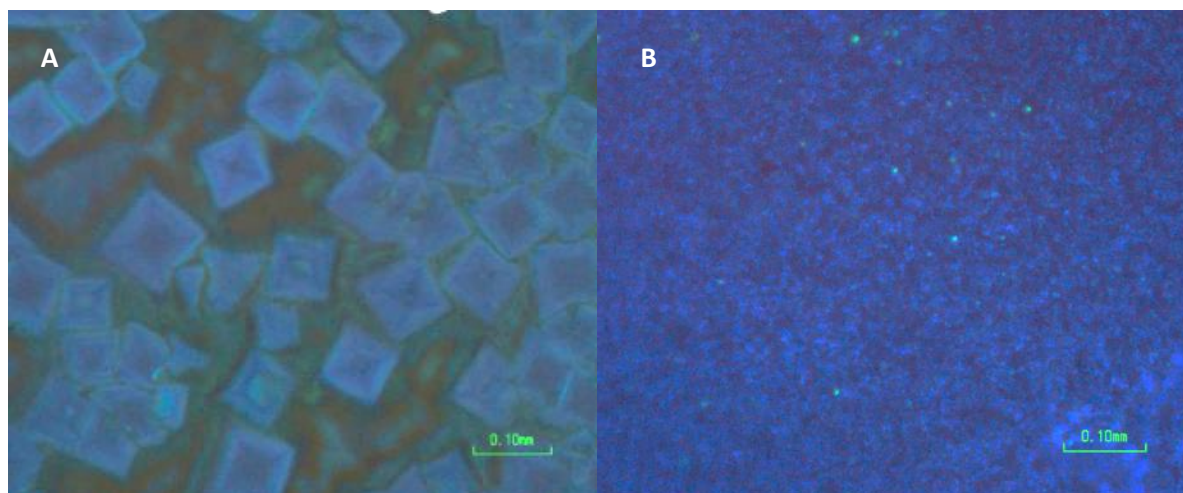
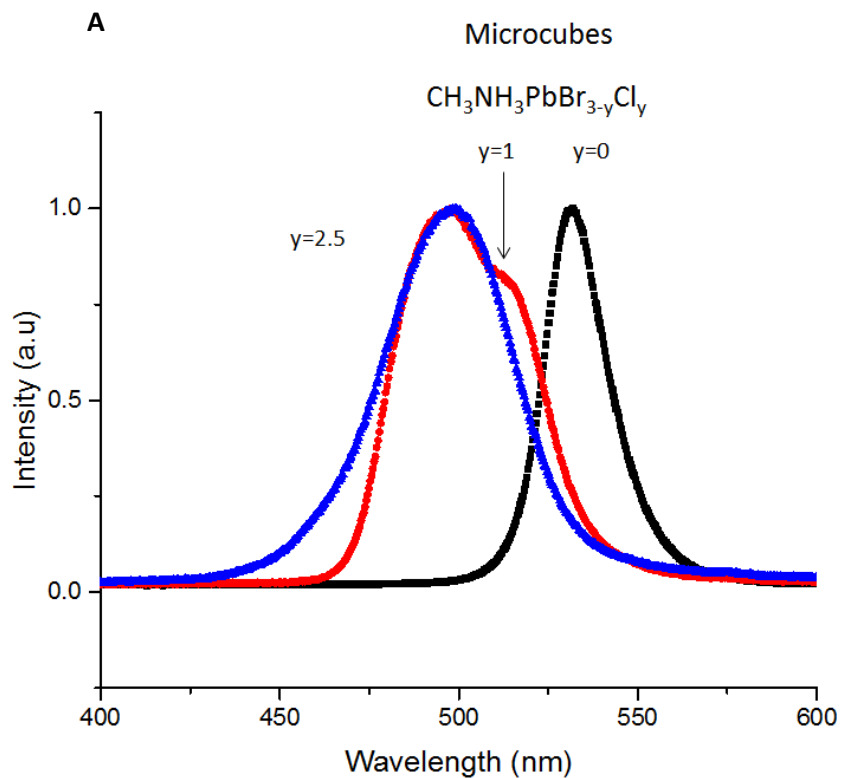
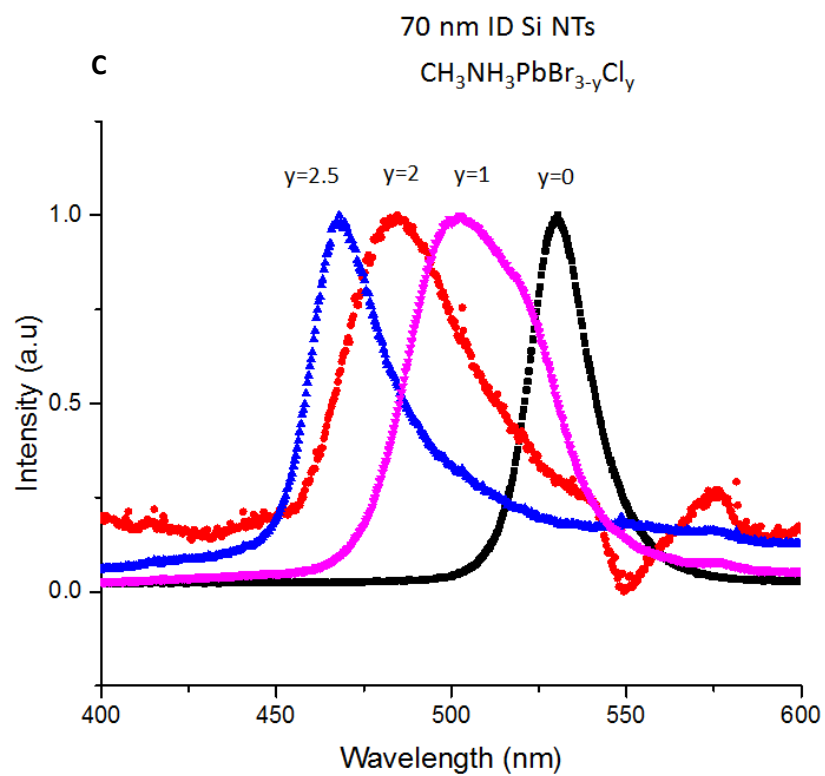
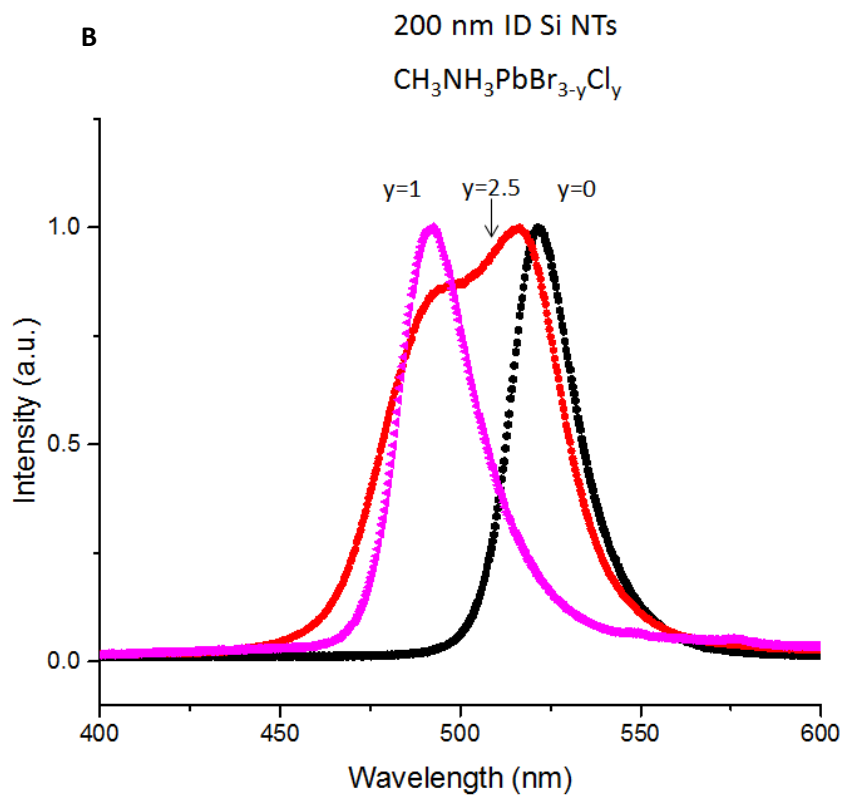


Figure 71: Fluorescence images of: a) $\text{CH}_3\text{NH}_3\text{PbBr}_{0.5}\text{Cl}_{2.5}$ cubes and b) 70 nm ID Si NTs loaded with $\text{CH}_3\text{NH}_3\text{PbBr}_{0.5}\text{Cl}_{2.5}$.

In Figure 72a, a series of PL spectra for the $\text{CH}_3\text{NH}_3\text{PbBr}_{3-y}\text{Cl}_y$ family with microcubes and Si NTs loaded with $\text{CH}_3\text{NH}_3\text{PbBr}_{3-y}\text{Cl}_y$ are shown. It is clear that the mixed Br-Cl perovskite systems are far more complicated than the analogous I-Br systems. For the $\text{CH}_3\text{NH}_3\text{PbBr}_{3-y}\text{Cl}_y$ microcube family and such structures formed within 200 nm and 30 nm Si NT templates, certain ratios produce emission spectra with multiple maxima, suggesting the formation of multiple reaction products. The only relatively 'clean' system for these $\text{CH}_3\text{NH}_3\text{PbBr}_{3-y}\text{Cl}_y$ structures emerges with the use of a 70 nm Si NT template, where there is a blue shift in PL maximum with increasing Cl content. Further investigations in this Br-Cl system are certainly necessary. It should also be pointed out that in this series of experiments, attempts to form $\text{CH}_3\text{NH}_3\text{PbBrCl}_3$ resulted in a non-luminescent material.





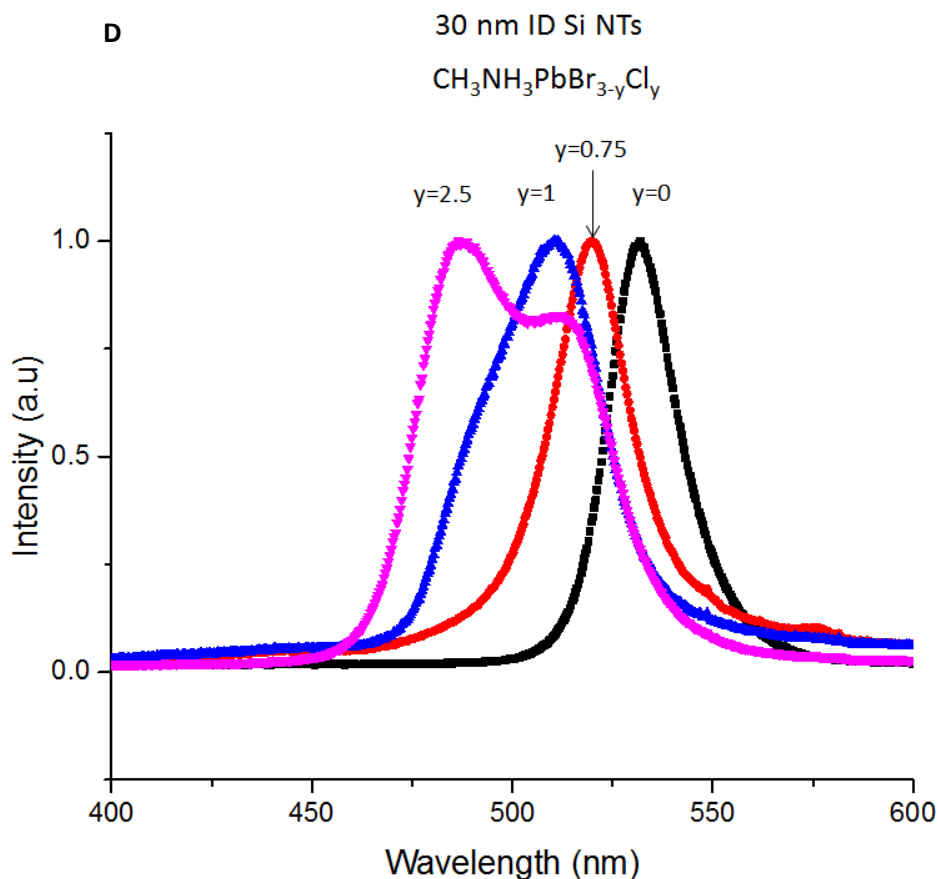


Figure 72: a) PL emission peaks of perovskite micro cubes, b) PL of 200 nm ID Si NTs, c) PL of 70 nm ID Si NTs and d) PL of 30 nm ID Si NTs.

5.6. Conclusions

In this chapter, precise control of perovskite formation using Si NTs as a template is demonstrated. For the case of methyl ammonium lead tri-iodide, while small measurable shifts in PL maximum are observed as a function of nanotube template inner diameter, more striking is the size-dependent suppression of a tetragonal to orthorhombic phase transition for the smallest diameter perovskites. Interestingly, tunability of visible light emission from nanoscale perovskites template by SiNTs is possible by altering halide content (for both I-Br as well as Br-Cl systems),

and in the case of the Bromide-Iodide system it appears that the nanotube template influences product composition homogeneity. The Br-Cl creates complex product mixtures that need further investigation.

Chapter VI

Fabrication of solar cells using perovskite microwires and perovskites loaded into silicon nanotubes

6.1. Introduction

Perovskites solar cells are relatively cheap and easy to manufacture. In the past 10 years perovskite-based solar cells have improved in reported power cell efficiency (PCE), from initial values of 2.2 % in 2006 to up to 22.1 % in 2016. In theory, this value could reach an optimal 31%.¹⁶⁰ Currently, commercially-available silicon solar panels have efficiencies ranging from 16 to 20 %. A combination of Silicon solar cells with perovskite phases (in a tandem solar cell design) efficiencies higher than 31% are envisioned.¹⁶⁰

Figure 73 shows the basic architecture of a perovskite-based solar cell. This structure consists of a conducting substrate such as FTO glass, then an electron transport layer (ETL) followed by perovskite active absorber, then a hole transport material (HTM) and finally a top metal contact (usually gold, silver, or aluminum) is deposited on the top of HTM for electrical measurements. Typical materials for the ETL are: Al_2O_3 , TiO_2 , and ZnO ;¹⁶¹ for the HTM, choices are: Poly(3-hexylthiophene-2,5-diyl) (P3HT), Carbon, poly(3,4-ethylenedioxythiophene) polystyrene sulfonate (PEDOT:PSS) and 2,2',7,7'-Tetrakis[N,N-di(4-methoxyphenyl)amino]-9,9'-spirobifluorene (Spiro-OMeTAD).^{161,162} Measured PCE values vary depending on the morphology in each layer in the solar cell and its identity.¹⁶³

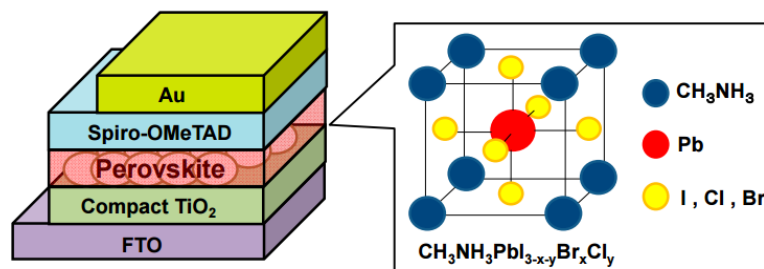


Figure 73: Basic architecture of a perovskite solar cell. Adapted from Ref. 163.

In terms of characterization of solar cells, electrical techniques are critical, centering on current-voltage (I-V) measurements. I-V characterization provides useful parameters such as J_{sc} , V_{oc} , P_{max} , I_{max} , Fill Factor (FF), and efficiency. These parameters will be defined later in this chapter. In order to understand the basis of these electrical measurements it is useful to construct a simple circuit diagram of a solar cell as defined in Figure 74:^{164,165}

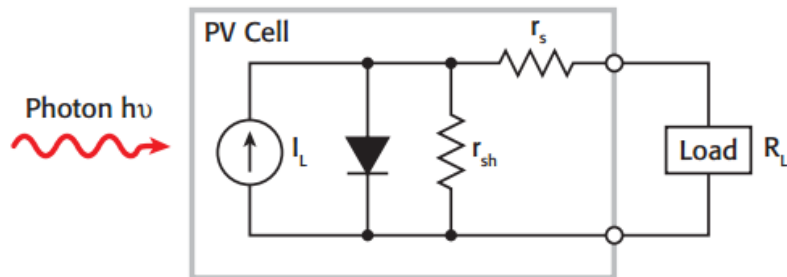


Figure 74: Idealized equivalent circuit of a photovoltaic cell. Adapted from Ref. 165.

In this idealized circuit, the following components are present: a light-induced current source (I_L), a diode that generates a saturation current I_S ; associated with this circuit is a series resistance r_s and shunt resistor r_{sh} . The series resistance is due to the resistance of the metal contacts, ohmic losses in the front surface of the cell, impurity concentrations, and junction depth.¹⁶⁶ The series resistance is an important parameter because it reduces both the cell's short circuit current and its maximum power output. Ideally, the series resistance should be 0Ω ($r_s = 0$). The shunt resistance represents the loss due to surface leakage along the edge of the cell or to crystal defects. The shunt resistance should ideally be infinite ($r_{sh} = \infty$). If a load resistor (R_L) is connected to an illuminated solar cell, then the total current becomes:^{166,165}

$$I = I_S(e^{qv/kT} - 1) - I_L \quad (17)$$

I_S = current due to diode saturation

I_L = current due to optical generation

In Figure 75, a typical I-V curve from this type of electrical measurement for a photovoltaic cell is illustrated. Some of the key terms associated with analysis of this type of plot include:^{165,166}

P_{\max} = Maximum power

FF= Fill factor = $I_{\max} V_{\max} / I_{sc} V_{oc}$

I_{\max} = Maximum cell current.

V_{\max} = Voltage where the power output is the greatest.

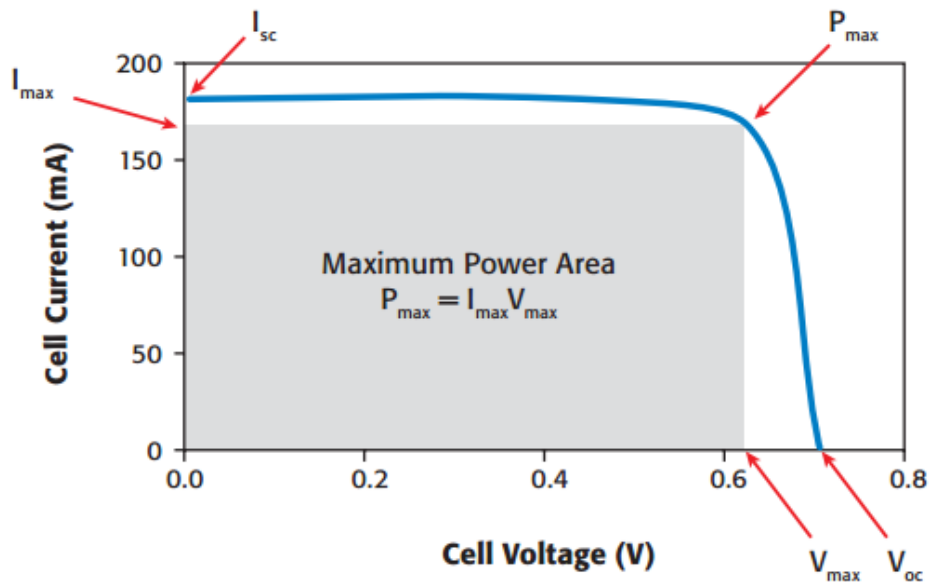


Figure 75: Typical forward bias I-V characteristics of a solar cell. Adapted from Ref. 162.

Finally, the efficiency of the solar cell is defined as:

$$\eta = P_{\max} / P_{in} \quad (18)$$

Here P_{in} = the power input to the cell, defined as the total radiant energy incident on the surface of the cell (in W).

6.2. Solar cell fabrication process

Initial studies of solar cell fabrication were made using some of the nanoscale perovskite Si NT templates described in the previous chapter, along with micrometer size perovskite wires serving as a bulk control. In Figure 76 the basic diagram of a solar cell based on a perovskite absorber is shown. The layout is as follows (from bottom to top): First the TiO₂ layer is deposited, then the perovskite microwires (or Si NTs loaded with perovskite) are prepared, then carbon black (used as a hole acceptor material) is deposited by hand and finally the etched FTO contact is physically placed on top.

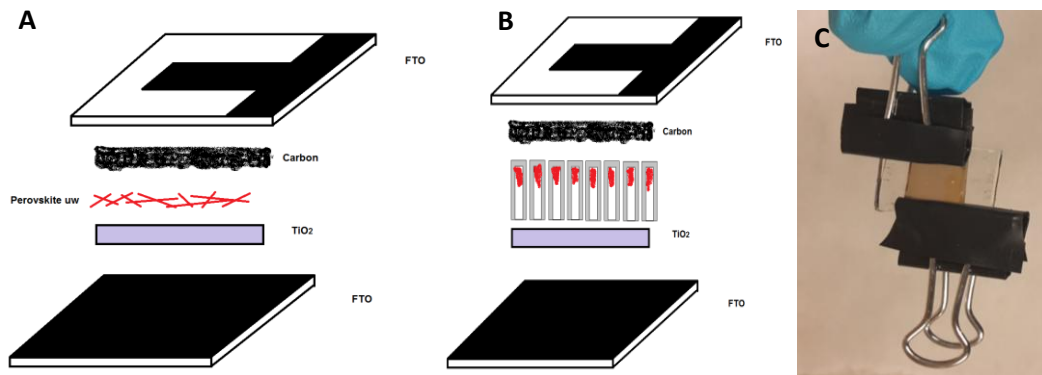


Figure 76: Solar cell structure. a) Using perovskite microwires, b) using Si NTs loaded with perovskite, c) Solar cell final product.

In Figure 77 the energy diagram associated with a solar cell is presented. The process begins with electron/hole pair generation in the perovskite absorber layer; at this point conduction band electrons are injected into the silicon layer (if the nanotube layer is present), followed by electron movement to the TiO₂ layer, which also acts as a hole barrier layer in this case. Holes, on the other hand, move energetically uphill into the carbon layer and ultimately to FTO layer and the external circuit. The photovoltaic performance of such a structure depends on

band gap, carrier mobility and carrier recombination around the interface between the perovskite layer and TiO_2 structure as the electron-transporting layer.

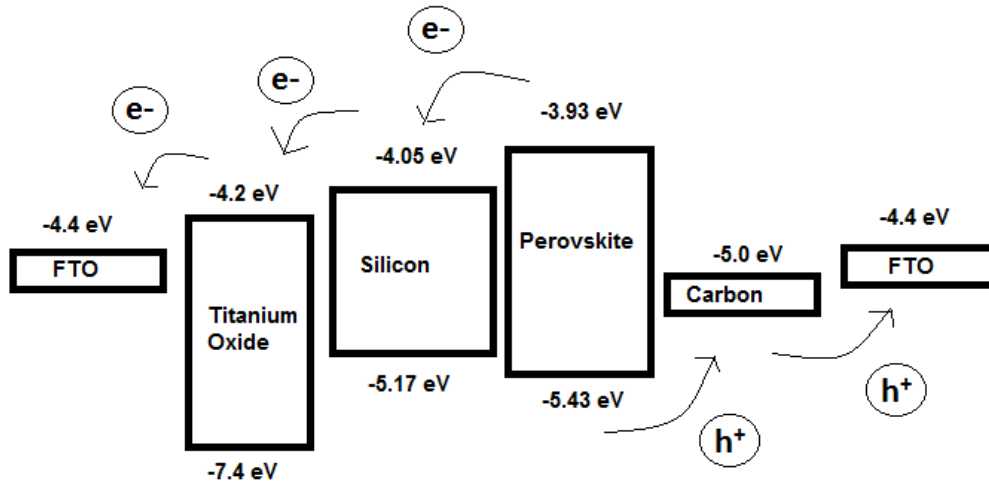


Figure 77: Solar cell energy diagram for the perovskite-based structures described in this chapter.

6.2.1. Experimental

6.2.1.1. Titanium dioxide / Si NT deposition and fabrication

A titanium precursor solution is made using 50 ml of ethanol, 5 ml of acetic acid and $\text{Ti}(\text{OCH}(\text{CH}_3)_2)_4$ (0.415 M). All reagents were obtained from Sigma-Aldrich. This solution is stirred for 5 hours, then 200 μL solution is spin coated on FTO glass at 3000 rpm for 30 seconds. The sample is then annealed at 500 $^\circ\text{C}$ in air for 2 hours. Using the processes described in Chapter 2, the ZnO seeds, ZnO nanowires, Si deposition, etching and perovskite precursor loading steps are then completed on the top of this TiO_2 layer. In order to protect the conductive area on the FTO, a small piece of Scotch[®] tape is placed in the protected area. This same area has to be protected during Si deposition, so on the top of the ZnO NWs a small amount of ZnO

paste is deposited with a spatula. The paste is prepared using 0.3g ZnO powder, mixed with 500 uL of ethanol (70%) and 1 drop of Triton x-100 surfactant.

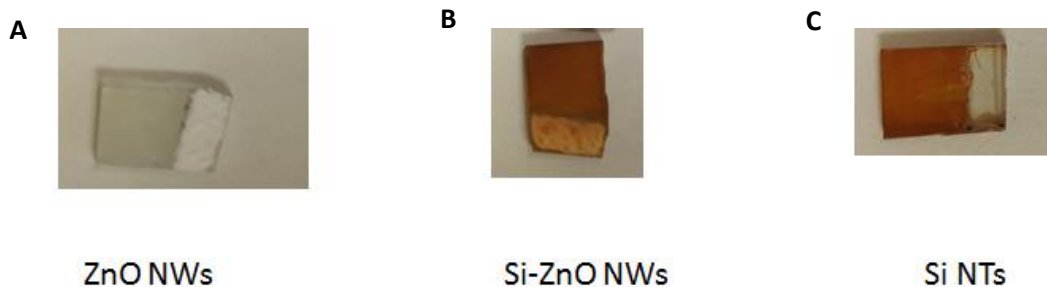


Figure 78: a) ZnO NWs on FTO glass with the ZnO paste, b) Si-ZnO NWs and c) Si NTs after the etching process.

6.2.1.2. Etching of FTO

First a mask is created with the desired pattern, and placed on the top of FTO glass. Nitrocellulose is then applied to the surface (in the form of commercial nail polish), allowed to dry, and the mask is removed from the FTO. Zn powder is dispersed on the FTO surface and the sample is covered with 2M HCl solution (1 ml). After waiting for 15 min, the FTO sample is washed with DI water, and then sonicated with acetone to remove the nitrocellulose. Following this step, the sample is soaked in concentrated HCl to remove remaining Zn on the surface, sonicated in acetone once again, and finally blown dry with nitrogen.

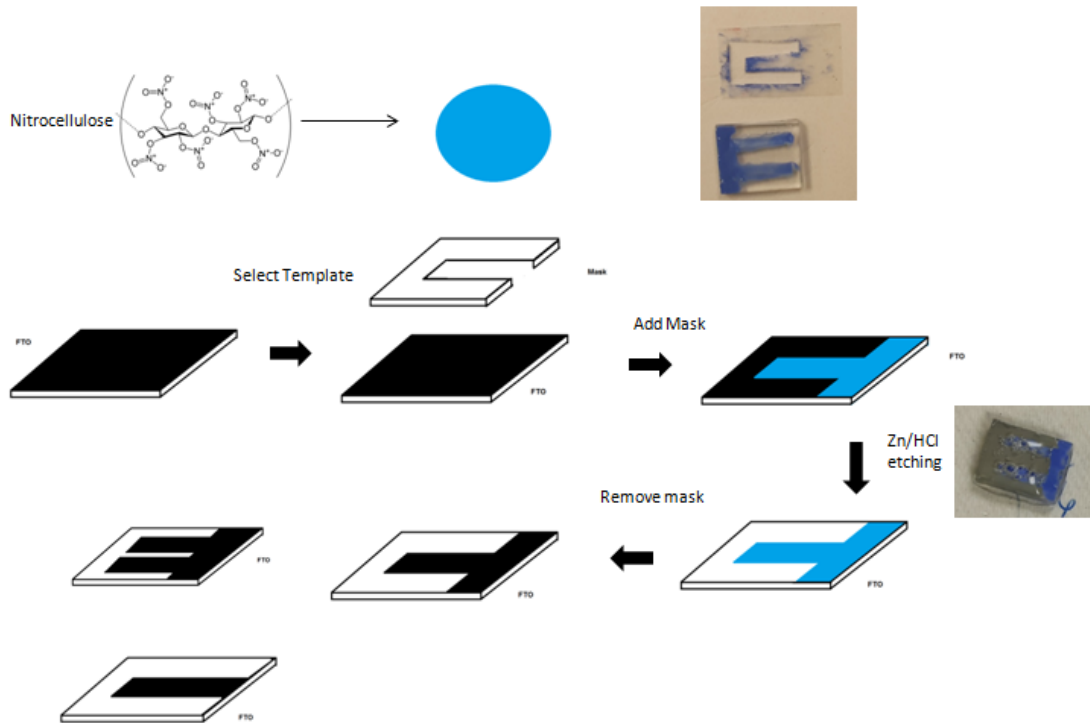


Figure 79: FTO etching process described in the section above.

6.3. Results and Discussion

6.3.1. Morphological characterization

Cross-sectional SEM images show the thickness of the different layers in a typical solar cell fabricated using the above procedure (Figure 80). In these films, Si NTs have a length of $\sim 1.8 \mu\text{m}$, while the TiO_2 layer is 160 nm, and the FTO thickness, approximately 370 nm. The carbon layer is very thick, more than $200 \mu\text{m}$ according with SEM data (Figure 81). This is not a surprising result, since the carbon layer is added by hand.

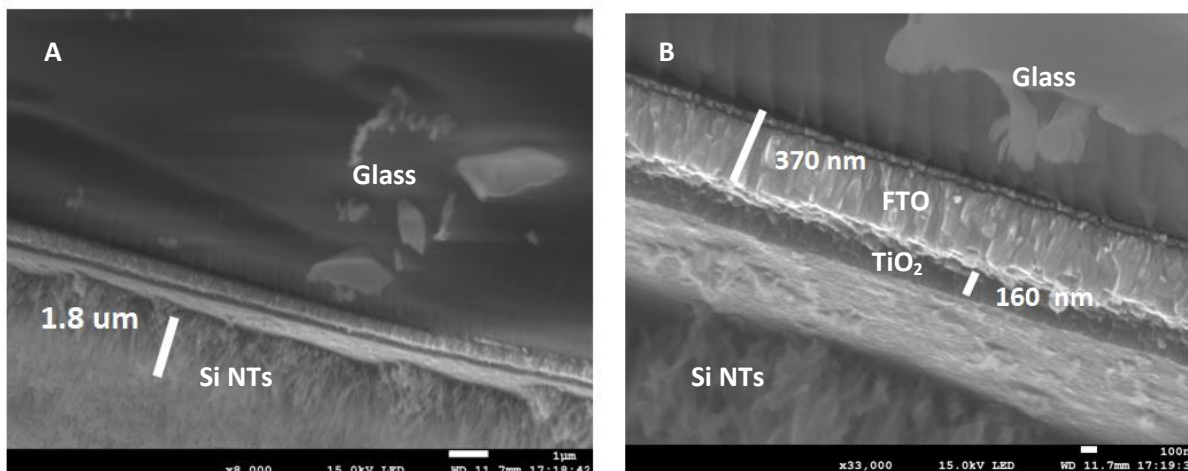


Figure 80: SEM of cross section showing the thickness of FTO, TiO₂ and Si NTs. a) low magnification, b) high magnification.

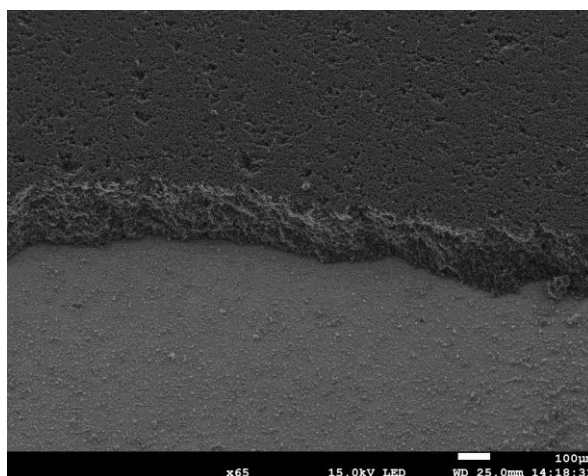


Figure 81: SEM of carbon on a FTO glass substrate (top layer).

6.3.2. Electrical characterization

Electrical characterization of the above solar cells was made using a Keithley 2420 sourcemeter. Alligator clips were used to connect the solar cell to the sourcemeter; a 450 W Xe lamp (SPEX Inc) was used as a solar simulator, with spectral irradiance confirmed with the use of a radiometer. The lamp to cell distance was varied until an intensity of 1000 W/m² was obtained. Figure 82 illustrates the impact of irradiation on current density in a typical perovskite

microwire solar cell fabricated using the above conditions. The difference in current between dark and illuminated conditions is readily apparent. Green Mountain IV-Stat 3.1 software was used to analyze the current-voltage data. This software plots voltage as a function of current density and automatically calculates important photovoltaic parameters such as solar cell efficiency, V_{oc} , and J_{sc} (based on the active area of a given structure).

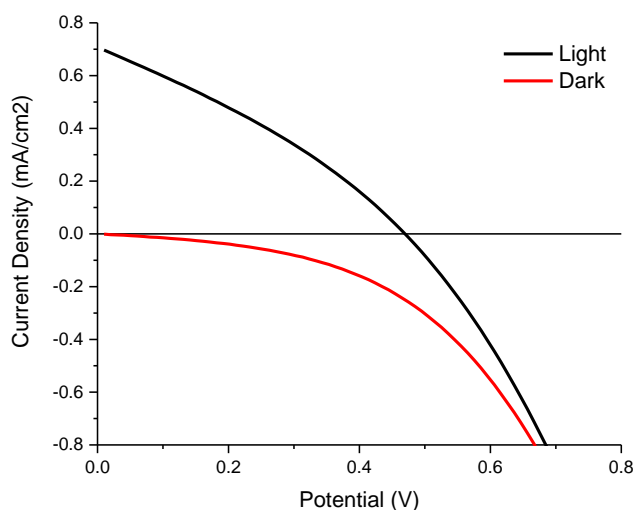


Figure 82: Voltage vs current density plot of a solar cell fabricated with perovskite microwires.

Si NTs were grown on FTO glass previously coated with 160 nm thick TiO_2 . In addition to $CH_3NH_3PbI_3$ microwires, solar cells fabricated with $CH_3NH_3PbI_3$ within 30 nm, 70 nm and 200 nm ID Si NTs as the active absorber were also evaluated. Figure 83 presents SEM and EDX data of $CH_3NH_3PbI_3$ in 200 nm ID Si NTs. In the EDX spectrum, peaks for Ti and Sn appear from the TiO_2 layer and FTO glass, respectively. The Pb and I signals are attributed to the presence of the $CH_3NH_3PbI_3$ inside Si NTs.

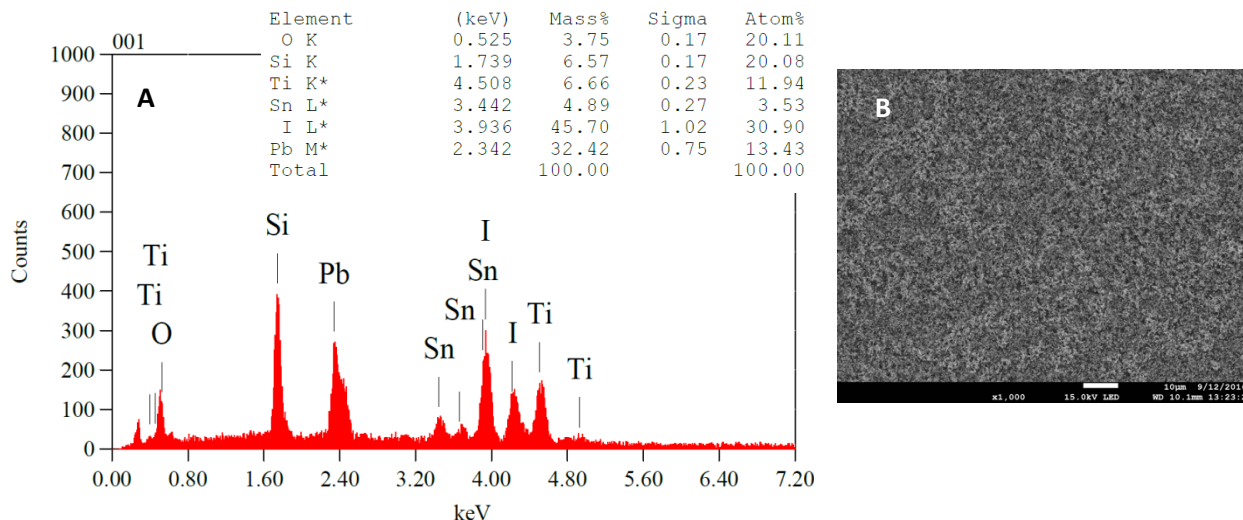


Figure 83: a) SEM-EDX of FTO-TiO₂- CH₃NH₃PbI₃ inside 200nm ID Si NTs. b) SEM image associated with the EDX spectrum.

Of the several solar cells constructed using the above composition, thus far the highest efficiency was obtained using CH₃NH₃PbI₃ microwires with an efficiency of 3.1%. Several types of cells were also fabricated using CH₃NH₃PbI₃ nanostructures prepared inside SiNTs of varying inner diameter (as described in the previous chapter). The highest efficiency in this type of structure was in the case of 30 nm ID SiNTs loaded with CH₃NH₃PbI₃, where a value of 0.15 % was obtained. The likely origin for the very low efficiencies for the CH₃NH₃PbI₃ / Si NTs-containing systems is a consequence of an incomplete filling of the perovskite in a given nanotube, with the charge carriers required to travel relatively long distances (through undoped Si layers) to reach the necessary FTO and metal contacts. Future designs will likely involve the incorporation of more complete perovskite loading of the SiNTs, along with facilitating charge carrier separation by doping the wall of the SiNT.

However, based on existing literature data, greater photovoltaic efficiencies will likely appear with the use of relatively more expensive hole acceptor materials such as PEDOT:PSS

and Spiro(OMeTad).¹⁶⁷ More careful exclusion of moisture and dust (through the use of a glove box) will likely also improve efficiency and stability here.

Table 8: Comparison of Solar cell parameter of controls, perovskite microwires and Si NTs loaded with perovskite.

| Controls | | Jsc (mA/cm²) | Voc (V) | PCE (%) |
|---|------|--------------------------------|----------------|----------------|
| FTO-FTO | 0-1V | --- | 0.1791 | --- |
| FTO-Carbon black-FTO | 0-1V | --- | 0.2708 | --- |
| FTO-70 nm Si NTs-FTO | 0-1V | 0 | 0 | 0 |
| FTO-Carbon black-70 nm Si NTs-FTO | 0-1V | 0 | 0 | 0 |
| FTO-uw-TiO ₂ -FTO | 0-1V | 6.14E-4 | 0.192 | 0.00029 |
| FTO-Carbon black-uw-FTO | 0-1V | 8.83E-4 | 0.1709 | 0.0003 |
| Solar Cells | | | | |
| FTO-Carbon black-uw-TiO ₂ -FTO | 0-1V | 5.056 | 0.4616 | 3.1 |
| FTO-Carbon black-30nm Si NTs-TiO ₂ -FTO | 0-1V | 0.8002 | 0.5667 | 0.152 |
| FTO-Carbon black-70nm Si NTs-TiO ₂ -FTO | 0-1V | 0.6444 | 0.1397 | 0.0226 |
| FTO-Carbon black-200nm Si NTs-TiO ₂ -FTO | 0-1V | 0.4229 | 0.07223 | 0.0076 |

In order to analyze these preliminary results, we compare the above values with those of some previously-reported work on the size-dependence of perovskite phases on resultant photovoltaic efficiency. Mohammadian et al reported CH₃NH₃PbI₃ perovskite solar cells with different grain size distributions.¹⁶⁷ The solar cell consists of 400 nm TiO₂ in nanoparticle form on FTO, followed by a perovskite thickness of 300 nm with grain sizes from 50 nm to 300 nm, then the HTL in this case Spiro-OMeTAD finally gold was deposited to make electrical contacts.¹⁶⁸ In Table 9 the solar cell parameters versus the grain size distribution data are presented. This data follows the same trend as the above perovskite /Si NT data since PCE is observed to increase when grain size is decreased. This increasing PCE with decreasing perovskite grain size is attributed to the presence of a larger surface area in contact with both

ETL and HTL. In our system the increased surface area is limited to the electron side (associated with the SiNT layer).

Table 9: Solar cell parameters based on grain size distribution in a $\text{CH}_3\text{NH}_3\text{PbI}_3$ perovskite based solar cell platform. Adapted from Ref. 168.

| grain size distribution (nm) | J_{SC} (mA/cm ²) | V_{OC} (V) | FF | PCE (%) |
|------------------------------|---------------------------------------|---------------------|----|---------|
| 300 | 17.05 | 0.8 | 44 | 6.01 |
| 200 | 17.65 | 0.85 | 46 | 6.90 |
| 100 | 17.91 | 0.87 | 54 | 8.41 |
| 50 | 17.97 | 0.88 | 46 | 7.27 |

6.4. Summary

These initial studies show proof-of-concept performance for a photovoltaic system based on a nanostructured $\text{CH}_3\text{NH}_3\text{PbI}_3$ -based active absorber. It is also clear that these initial structures are not competitive with known perovskite platforms and our designs have to be improved. However, these studies show a clear size dependence in photovoltaic efficiency for those perovskite-based structures housed in Si NTs, but again the system needs to be refined.

Chapter VII
Concluding Remarks

In this work, the fabrication of Si NTs was presented. Si NTs have interesting potential for the areas of drug delivery, MRI contrast agents, tissue engineering, photovoltaics, and battery technology. In Chapter I, different types of nanoscale size Si materials were described, as well as selected applications of those materials. Particular focus was given to the different available methods for the Si NTs fabrication process.

In Chapter II, the detailed fabrication process for Si NTs using ZnO as a template was presented. It was shown that by controlling certain parameters in each step, it is possible to control Si NTs morphology, include parameters such as wall thickness, inner diameter, length and crystallinity. Si NTs inner diameter is controlled by growth of the ZnO template, where the ZnO NW diameter is dependent on precursor concentration, time of reaction, and the addition of the surface additive PEI. In such structures the diameter can be varied from 20 nm up to 200 nm and length from 0.5 μm to 2 μm . Si NTs wall thickness is controlled by silicon deposition conditions such as temperature and position of the sample inside the tube furnace. In these nanotubes, wall thickness can be varied from 10 nm to 80 nm, with the Si NTs with 10 nm thickness are highly porous with interesting properties. These parameters are important for future applications; for example, dissolution behavior is affected by wall thickness and crystallinity, and by tuning the dissolution behavior of these Si NTs we can apply them in use in tissue engineering or drug delivery.

In Chapter II Si NTs are investigated with regard to electrochemical Li insertion experiments. These Si NTs possess porous sidewalls with a wall thickness of 10 nm, 57 nm in diameter and 2 μm in length, and were self-supported on stainless steel substrates. Electrochemical measurements were made in collaboration with scientists in France. The discharge capacity after 30th cycle was an impressive 1670 mAhg^{-1} . With regard to long term

performance the battery was tested up to 180 cycles, we obtained a capacity of 800 mAhg^{-1} with a capacity retention above 99% but an overall coulombic efficiency of 84 %. The performance of this system is better than several of those previously-reported SiNTs, but lags behind that of a double-wall Si NT design. Moving forward, several improvements are envisioned, including use of a Cr adhesion layer and reduction of SEI layer formation, ideally perhaps through the use of a solid state electrolyte. These experiments are in progress with our collaborators.

In Chapter III, the properties of superparamagnetic Fe_3O_4 NPs infiltrated into Si NTs with different wall thicknesses were investigated. These materials are of potential relevance to MRI contrast agents and magnetic-field assisted drug delivery. Fundamental studies of blocking temperature and coercivity were measured with our collaborators in Austria; they found that the blocking temperature (T_B) of Fe_3O_4 NPs inside Si NTs are similar to that of free-standing NPs. In order to evaluate this material as a potential contrast agent in MRI, the relaxation times T_1 and T_2 were measured. The values obtained in these experiments are in the range of Fe_3O_4 NP clusters previously reported in the literature. All Fe_3O_4 NP samples loaded into SiNTs showed a relaxivity ratio $r_2/r_1 > 2$, putting them in the category of negative contrast agent.

In Chapter IV, SiNTs were employed as a reaction vessel to produce nanoscale perovskites $\text{CH}_3\text{NH}_3\text{PbX}_3$ ($X = \text{I}, \text{Br}$) as well as a series of mixed halide phases containing I-Br and Br-Cl. Several different Si NTs inner diameters were selected for this purpose and PL maxima values were compared the bulk in the form of microwires and microcubes. Our collaborators in Israel measured the temperature-dependent PL from room temperature down to 4K for $\text{CH}_3\text{NH}_3\text{PbI}_3$ microwires and $\text{CH}_3\text{NH}_3\text{PbI}_3$ formed in Si NTs. A suppression of a tetragonal to orthorhombic phase transition was observed in perovskites formed within 70 nm ID Si NTs normally observed in the bulk. Perovskite compositions containing I-Br were studied

($\text{CH}_3\text{NH}_3\text{PbI}_{3-x}\text{Br}$), with demonstration of PL tenability as a function of the different ratios of the halide precursors. Attempts to form analogous nanostructures with Br-Cl create complex product mixtures that need further investigation.

In Chapter VI, initial attempts to fabricate photovoltaic devices based on these perovskite nanostructures in SiNTs are described. Our measured efficiencies are not as high as those reported in the literature, likely a consequence of the incomplete filling of the SiNT with perovskite and use of carbon as a hole transport layer. These issues can ideally improved with additional refinement. Interestingly our preliminary data suggests a clear perovskite size dependence with regard to solar cell efficiency with structures fabricated using smaller ID Si NTs having higher PCE values.

Overall, the experiments described in this dissertation suggest opportunities for further exploration in several technologically-relevant areas that will likely be pursued in the future by our group.

VIII References

1. Perepichka, D. F.; Rosei, F. *Small* **2006**, *2* (1), 22.
2. He, Y.; Fan, C.; Lee, S.-T. *Nano Today* **2010**, *5* (4), 282.
3. Singh, M. P.; Atkins, T. M.; Muthuswamy, E.; Kamali, S.; Tu, C.; Louie, A. Y.; Kauzlarich, S. M. *ACS Nano* **2012**, *6* (6), 5596.
4. Irrera, A.; Artoni, P.; Saija, R.; Gucciardi, P. G.; Iatì, M. A.; Borghese, F.; Denti, P.; Iacona, F.; Priolo, F.; Maragò, O. M. *Nano Letters* **2011**, *11* (11), 4879.
5. Xiao, L.; Gu, L.; Howell, S. B.; Sailor, M. J. *ACS Nano* **2011**, *5* (5), 3651.
6. Chen, B.; Meng, G.; Xu, Q.; Zhu, X.; Kong, M.; Chu, Z.; Han, F.; Zhang, Z. *ACS Nano* **2010**, *4* (12), 7105.
7. Delacour, C.; Blaize, S.; Grosse, P.; Fedeli, J. M.; Bruyant, A.; Salas-Montiel, R.; Lerondel, G.; Chelnokov, A. *Nano Letters* **2010**, *10* (8), 2922.
8. Zhang, H.; Braun, P. V. *Nano Letters* **2012**, *12* (6), 2778.
9. Gharghi, M.; Fathi, E.; Kante, B.; Sivoththaman, S.; Zhang, X. *Nano Letters* **2012**, *12* (12), 6278.
10. Peng, F.; Su, Y.; Zhong, Y.; Fan, C.; Lee, S.-T.; He, Y. *Accounts of Chemical Research* **2014**, *47* (2), 612.
11. Talapin, D. V.; Lee, J.-S.; Kovalenko, M. V.; Shevchenko, E. V. *Chemical Reviews* **2010**, *110* (1), 389.
12. O'Farrell, N.; Houlton, A.; Horrocks, B. R. *International Journal of Nanomedicine* **2006**, *1* (4), 451.
13. Strtak, A.; Sathiamoorthy, S.; Tang, P. S.; Tsoi, K. M.; Song, F.; Anderson, J. B.; Chan, W. C. W.; Shin, J. A. *Bioconjugate Chemistry* **2017**.

14. Laaksonen, T.; Santos, H.; Vihola, H.; Salonen, J.; Riikonen, J.; Heikkilä, T.; Peltonen, L.; Kumar, N.; Murzin, D. Y.; Lehto, V.-P.; Hirvonen, J. *Chemical Research in Toxicology* **2007**, *20* (12), 1913.
15. Kang, Z.; Tsang, C. H. A.; Zhang, Z.; Zhang, M.; Wong, N.; Zapien, J. A.; Shan, Y.; Lee, S.-T. *Journal of the American Chemical Society* **2007**, *129* (17), 5326.
16. Hata, K.; Yoshida, S.; Fujita, M.; Yasuda, S.; Makimura, T.; Murakami, K.; Shigekawa, H. *The Journal of Physical Chemistry B* **2001**, *105* (44), 10842.
17. Su, X.; Kuang, L.; Battle, C.; Shaner, T.; Mitchell, B. S.; Fink, M. J.; Jayawickramarajah, J. *Bioconjugate Chemistry* **2014**, *25* (10), 1739.
18. McMillan, P. F.; Gryko, J.; Bull, C.; Arledge, R.; Kenyon, A. J.; Cressey, B. A. *Journal of Solid State Chemistry* **2005**, *178* (3), 937.
19. Schfer, R.; Klemm, W. *Zeitschrift fr anorganische und allgemeine Chemie* **1961**, *312* (3-4), 214.
20. Yoshida, T.; Takeyama, S.; Yamada, Y.; Mutoh, K. *Applied Physics Letters* **1996**, *68* (13), 1772.
21. Lam, C.; Zhang, Y.; Tang, Y.; Lee, C.; Bello, I.; Lee, S. *Journal of Crystal Growth* **2000**, *220* (4), 466.
22. Treuting, R. G.; Arnold, S. M. *Acta Metallurgica* **1957**, *5* (10), 598.
23. Morales, A. M., Lieber, C. M. *Science* **1998**, *279* (5348), 208.
24. Schmidt, V.; Wittemann, J. V.; Senz, S.; Gösele, U. *Advanced Materials* **2009**, *21* (25-26), 2681.
25. Cui, Y.; Lauhon, L. J.; Gudiksen, M. S.; Wang, J.; Lieber, C. M. *Applied Physics Letters* **2001**, *78* (15), 2214.

26. *Semiconductor nanostructures for optoelectronic devices: Processing, characterization and applications*; Yi, G.-C., Ed.; Springer-Verlag Berlin and Heidelberg GmbH & Co. K: Berlin, 2012.
27. *Semiconducting silicon Nanowires for biomedical applications*; Coffey, J. L., Ed.; Woodhead Publishing: New York, NY, United States, 2014.
28. Picraux, S. T.; Dayeh, S. A.; Manandhar, P.; Perea, D. E.; Choi, S. G. *The Journal of The Minerals, Metals & Materials Society* **2010**, 62 (4), 35.
29. Heitsch, A. T.; Fanfair, D. D.; Tuan, H.-Y.; Korgel, B. A. *Journal of the American Chemical Society* **2008**, 130 (16), 5436.
30. Tuan, H.-Y.; Ghezelbash, A.; Korgel, B. A. *Chemistry of Materials* **2008**, 20 (6), 2306.
31. Chen, G. *SPIE Newsroom* **2008**. DOI: 10.1117/2.1200808.1087
32. Boehm, H.-P. *Angewandte Chemie* **1980**, 92 (4), 328.
33. Zhang, W.; Tong, L.; Yang, C. *Nano Letters* **2012**, 12 (2), 1002.
34. Niculescu-Duvaz, D.; Getaz, J.; Springer, C. J. *Bioconjugate Chemistry* **2008**, 19 (4), 973.
35. Uhlir, A. *Bell System Technical Journal* **1956**, 35 (2), 333.
36. Granitzer, P.; Rumpf, K. *Materials* **2010**, 3 (2), 943.
37. Canham, L. T. *Applied Physics Letters* **1990**, 57 (10), 1046.
38. Ning, H.; Krueger, N. A.; Sheng, X.; Keum, H.; Zhang, C.; Choquette, K. D.; Li, X.; Kim, S.; Rogers, J. A.; Braun, P. V. *ACS Photonics* **2014**, 1 (11), 1144.
39. Wang, M.; Hartman, P. S.; Loni, A.; Canham, L. T.; Bodiford, N.; Coffey, J. L. *Langmuir* **2015**, 31 (22), 6179.

40. Guerrero-Lemus, R.; Moreno, J. D.; Martínez-Duart, J. M.; Corral, J. L. *Review of Scientific Instruments* **1996**, 67 (10), 3627.
41. Sotgiu, G.; Schirone, L.; Rallo, F. *Thin Solid Films* **1997**, 297 (1-2), 18.
42. Kuhl, M.; O'Halloran, G. M.; Gennissen, P. T. J.; French, P. J. *Journal of Micromechanics and Microengineering* **1998**, 8 (4), 317
43. Shih, S.; Jung, K. H.; Hsieh, T. Y.; Sarathy, J.; Campbell, J. C.; Kwong, D. L. *Applied Physics Letters* **1992**, 60 (15), 1863.
44. Jenkins, M. W. *Journal of Electrochemical Society* **1977**, 124 (5), 757.
45. Brigger, I.; Dubernet, C.; Couvreur, P. *Advanced Drug Delivery Reviews* **2002**, 54 (5), 631.
46. Chin, V.; Collins, B. E.; Sailor, M. J.; Bhatia, S. N. *Advanced Materials* **2001**, 13 (24), 1877.
47. Collins, B. E.; Dancil, K.-P. S.; Abbi, G.; Sailor, M. J. *Advanced Functional Materials* **2002**, 12 (3), 187.
48. Anglin, E. J.; Schwartz, M. P.; Ng, V. P.; Perelman, L. A.; Sailor, M. J. *Langmuir* **2004**, 20 (25), 11264.
49. Park, M.-H.; Kim, M. G.; Joo, J.; Kim, K.; Kim, J.; Ahn, S.; Cui, Y.; Cho, J. *Nano Letters* **2009**, 9 (11), 3844.
50. Li, G. L.; Zheng, Z.; Möhwald, H.; Shchukin, D. G. *ACS Nano* **2013**, 7 (3), 2470.
51. Coffey, J. L. *Mesoporous Biomaterials* **2016**, 2 (1).
52. Huang, X.; Gonzalez-Rodriguez, R.; Rich, R.; Gryczynski, Z.; Coffey, J. L. *Chemical Communications* **2013**, 49 (51), 5760.

53. Sha, J.; Niu, J.; Ma, X.; Xu, J.; Zhang, X.; Yang, Q.; Yang, D. *Advanced Materials* **2002**, *14* (17), 1219.
54. De Crescenzi, M.; Castrucci, P.; Scarselli, M.; Diociaiuti, M.; Chaudhari, P. S.; Balasubramanian, C.; Bhave, T. M.; Bhoraskar, S. V. *Applied Physics Letters* **2005**, *86* (23), 231901.
55. Goldberger, J.; He, R.; Zhang, Y.; Lee, S.; Yan, H.; Choi, H.-J.; Yang, P. *Nature* **2003**, *422* (6932), 599.
56. Asoh, H.; Matsuo, M.; Yoshihama, M.; Ono, S. *Applied Physics Letters* **2003**, *83* (21), 4408.
57. Andersson, L. H.; Dalziel, K.; Viervoll, H.; Zackrisson, M.; Ernster, L.; Diczfalusy, E. *Acta Chemica Scandinavica* **1958**, *12*, 495.
58. Bunting, W. E. *Industrial & Engineering Chemistry Analytical Edition* **1944**, *16* (10), 612.
59. Kahler, H. *Industrial & Engineering Chemistry Analytical Edition* **1941**, *13* (8), 536.
60. Wu, W.; Hu, G.; Cui, S.; Zhou, Y.; Wu, H. *Crystal Growth & Design* **2008**, *8* (11), 4014.
61. Cubicciotti, D. *Inorganic Chemistry* **1964**, *3* (7), 1061.
62. Kajiwara, T.; Hashimoto, K.; Kawai, T.; Sakata, T. *The Journal of Physical Chemistry* **1982**, *86* (23), 4516.
63. Lee, K.; Slinker, J.; Gorodetsky, A.; Flores-Torres, S.; Abruña, H.; Houston, P.; Malliaras, G. *Phys. Chem. Chem. Phys.* **2003**, *5*, 2606.
64. Su, Z.; Dickinson, C.; Wan, Y.; Wang, Z.; Wang, Y.; Sha, J.; Zhou, W. *Crystal Engineering Communications* **2010**, *12* (10), 2793.
65. Andersson, A. ; Thomas, J. *Journal of Power Sources* **2001**, 97-98, 498.

66. Armand, M.; Tarascon, J.-M. *Nature* **2008**, *451* (7179), 652.
67. Scrosati, B.; Garche, J. *Journal of Power Sources* **2010**, *195* (9), 2419.
68. Hayner, C. M.; Zhao, X.; Kung, H. H. *Annual Review of Chemical and Biomolecular Engineering* **2012**, *3* (1), 445.
69. Xu, G.-L.; Wang, Q.; Fang, J.-C.; Xu, Y.-F.; Li, J.-T.; Huang, L.; Sun, S.-G. *Journal of Materials Chemistry A* **2014**, *2* (47), 19941.
70. Goriparti, S.; Miele, E.; De Angelis, F.; Di Fabrizio, E.; Zaccaria, R. P.; Capiglia, C. *Journal of Power Sources* **2014**, *257*, 421.
71. Linden, D.; Reddy, T. B. *Linden's handbook of batteries*; McGraw-Hill: New York, NY, 2011.
72. Yang, M.; Hou, J. *Membranes* **2012**, *2* (4), 367.
73. Yue, L.; Ma, J.; Zhang, J.; Zhao, J.; Dong, S.; Liu, Z.; Cui, G.; Chen, L. *Energy Storage Materials* **2016**, *5*, 139.
74. Williams, M. E.; Lyons, L. J.; Long, J. W.; Murray, R. W. *The Journal of Physical Chemistry B* **1997**, *101* (38), 7584.
75. Xu, B.; Qian, D.; Wang, Z.; Meng, Y. S. *Materials Science and Engineering: R: Reports* **2012**, *73* (5-6), 51.
76. Chen, R.; Zhao, T.; Zhang, X.; Li, L.; Wu, F. *Nanoscale Horizons*. **2016**, *1* (6), 423.
77. Aravindan, V.; Gnanaraj, J.; Lee, Y.-S.; Madhavi, S. *Journal of Materials Chemistry A* **2013**, *1* (11), 3518.
78. Xu, W.; Wang, J.; Ding, F.; Chen, X.; Nasybulin, E.; Zhang, Y.; Zhang, J.-G. *Energy Environmental Sciences* **2014**, *7* (2), 513.
79. Nitta, N.; Wu, F.; Lee, J. T.; Yushin, G. *Materials Today* **2015**, *18* (5), 252.

80. Endo, M.; Kim, C.; Nishimura, K.; Fujino, T.; Miyashita, K. *Carbon* **2000**, 38 (2), 183.
81. Kaskhedikar, N. A.; Maier, J. *Advanced Materials* **2009**, 21 (25-26), 2664.
82. Tokumitsu, K.; Fujimoto, H.; Mabuchi, A.; Kasuh, T. *Carbon* **1999**, 37 (10), 1599.
83. Aurbach, D.; Markovsky, B.; Weissman, I.; Levi, E.; Ein-Eli, Y. *Electrochimica Acta* **1999**, 45 (1-2), 67.
84. Orendorff, C. J.; Doughty, D. H. *Interface magazine* **2012**, 21 (2), 35.
85. He, Y.-B.; Liu, M.; Huang, Z.-D.; Zhang, B.; Yu, Y.; Li, B.; Kang, F.; Kim, J.-K. *Journal of Power Sources* **2013**, 239, 269.
86. Boukamp, B. A. *Journal of Electrochemical Society* **1981**, 128 (4), 725.
87. Chan, C. K.; Peng, H.; Liu, G.; McIlwrath, K.; Zhang, X. F.; Huggins, R. A.; Cui, Y. *Nature Nanotechnology* **2007**, 3 (1), 31.
88. Bogart, T. D.; Chockla, A. M.; Korgel, B. A. *Current Opinion in Chemical Engineering* **2013**, 2 (3), 286.
89. Beaulieu, L. Y.; Hatchard, T. D.; Bonakdarpour, A.; Fleischauer, M. D.; Dahn, J. R. *Journal of The Electrochemical Society* **2003**, 150 (11), A1457.
90. Kasavajjula, U.; Wang, C.; Appleby, A. J. *Journal of Power Sources* **2007**, 163 (2), 1003.
91. Hannon, J. B.; Kodambaka, S.; Ross, F. M.; Tromp, R. M. *Nature* **2006**, 440 (7080), 69.
92. Yoo, J.-K.; Kim, J.; Jung, Y. S.; Kang, K. *Advanced Materials* **2012**, 24 (40), 5452.
93. Su, X.; Wu, Q.; Li, J.; Xiao, X.; Lott, A.; Lu, W.; Sheldon, B. W.; Wu, J. *Advanced Energy Materials* **2013**, 4 (1), 1300882.
94. Song, T.; Xia, J.; Lee, J.-H.; Lee, D. H.; Kwon, M.-S.; Choi, J.-M.; Wu, J.; Doo, S. K.; Chang, H.; Park, W. I.; Za
95. Kim, H.; Huang, Y.; Hwang, K.-C.; Rogers, J. A.; Paik, U. *Nano Letters* **2012**, 14, 3.

96. Wang, B.; Li, X.; Qiu, T.; Luo, B.; Ning, J.; Li, J.; Zhang, X.; Liang, M.; Zhi, L. *Nano Letters* **2013**, *13* (11), 5578.
97. Laruelle, S.; Grugeon, S.; Dupont, L. *Nature* **2000**, *407* (6803), 496.
98. Mao, O. *Journal of Electrochemical Society* **1999**, *146* (2), 414.
99. Tarascon, J.; Poizot, P.; Laruelle, S.; Grugeon, S.; Dupont, L. *Nature* **2000**, *407*, 496.
100. Zhou, Y.; Jiang, X.; Chen, L.; Yue, J.; Xu, H.; Yang, J.; Qian, Y. *Electrochimica Acta* **2014**, *127*, 252.
101. Wen, Z.; Lu, G.; Mao, S.; Kim, H.; Cui, S.; Yu, K.; Huang, X.; Hurley, P. T.; Mao, O.; Chen, J. *Electrochemistry Communications* **2013**, *29*, 67.
102. Wu, H.; Chan, G.; Choi, J. W.; Ryu, I.; Yao, Y.; Mcdowell, M. T.; Lee, S. W.; Jackson, A.; Yang, Y.; Hu, L.; Cui, Y. *Nature Nanotechnology* **2012**, *7* (5), 310.
103. Song, T.; Xia, J.; Lee, J.-H.; Lee, D. H.; Kwon, M.-S.; Choi, J.-M.; Wu, J.; Doo, S. K.; Chang, H.; Park, W. I.; Zang, D. S.; Kim, H.; Huang, Y.; Hwang, K.-C.; Rogers, J. A.; Paik, U. *Nano Letters* **2010**, *10* (5), 1710.
104. Moghaddam, M. M.; Pieber, B.; Glasnov, T.; Kappe, C. O. *ChemSusChem* **2014**, *7* (11), 3122.
105. Wilhelm, C.; Gazeau, F. *Biomaterials* **2008**, *29*, 3161.
106. M. J. Perez, L. Josephson and R. Weissleder, *ChemBioChem.*, **2004**, *5*, 261.
107. Estelrich, J.; Escribano, E.; Queralt, J.; Busquets, M. *International Journal of Molecular Sciences* **2015**, *16* (4), 8070.
108. Bañobre-López, M.; Teijeiro, A.; Rivas, J. *Reports of Practical Oncology & Radiotherapy* **2013**, *18* (6), 397.

109. Li, L.; Jiang, W.; Luo, K.; Song, H.; Lan, F.; Wu, Y.; Gu, Z. *Theranostics* **2013**, *3* (8), 595.
110. Soenen, S. J.; De Cuyper, M.; De Smedt, S. C.; Braeckmans, K. *Methods in Enzymology* **2012**, *509*, 195.
111. Mahmoudi, M.; Simchi, A.; Milani, A. S.; Stroeve, P. *Journal of Colloid and Interface Science* **2009**, *336* (2), 510.
112. Jung, K.-H.; Kim, H.-K.; Park, J.-A.; Nam, K. S.; Lee, G. H.; Chang, Y.; Kim, T.-J. *ACS Medicinal Chemistry Letters* **2012**, *3* (12), 1003.
113. Hu, F.; Zhao, Y. S. *Nanoscale* **2012**, *4* (20), 6235.
114. Rogosnitzky, M.; Branch, S. *BioMetals* **2016**, *29* (3), 365.
115. Kim, B. H.; Lee, N.; Kim, H.; An, K.; Park, Y. I.; Choi, Y.; Shin, K.; Lee, Y.; Kwon, S. G.; Na, H. B.; Park, J.-G.; Ahn, T.-Y.; Kim, Y.-W.; Moon, W. K.; Choi, S. H.; Hyeon, T. *Journal of the American Chemical Society* **2011**, *133* (32), 12624.
116. Hurley, K. R.; Lin, Y.-S.; Zhang, J.; Egger, S. M.; Haynes, C. L. *Chemistry of Materials* **2013**, *25* (9), 1968.
117. Bae, H.; Ahmad, T.; Rhee, I.; Chang, Y.; Jin, S.-U.; Hong, S. *Nanoscale Research Letters* **2012**, *7* (1), 44.
118. Mou, X.; Wei, X.; Li, Y.; Shen, W. *CrystEngComm* **2012**, *14* (16), 5107.
119. Schmidtke, C.; Eggers, R.; Zierold, R.; Feld, A.; Kloust, H.; Wolter, C.; Ostermann, J.; Merkl, J.-P.; Schotten, T.; Nielsch, K.; Weller, H. *Langmuir* **2014**, *30* (37), 11190.

120. Liu, X.; Marangon, I.; Melinte, G.; Wilhelm, C.; Ménard-Moyon, C.; Pichon, B. P.; Ersen, O.; Aubertin, K.; Baaziz, W.; Pham-Huu, C.; Bégin-Colin, S.; Bianco, A.; Gazeau, F.; Bégin, D. *ACS Nano* **2014**, 8 (11), 11290.
121. Baaziz, W.; Liu, X.; Florea, I.; Begin-Colin, S.; Pichon, B. P.; Ulhaq, C.; Ersen, O.; Soria-Sánchez, M.; Zafeiratos, S.; Janowska, I.; Begin, D.; Pham-Huu, C. *Journal of Materials Chemistry A* **2013**, 1 (44), 13853.
122. Thanh, N. T. K. *Magnetic nanoparticles: from fabrication to clinical applications: theory to therapy, chemistry to clinic, bench to bedside*; CRC Press: Boca Raton, FL, 2012.
123. Gui, M.; Smuleac, V.; Ormsbee, L. E.; Sedlak, D. L.; Bhattacharyya, D. *Journal of Nanoparticle Research* **2012**, 14 (5).
124. Granitzer, P.; Rumpf, K.; Gonzalez-Rodriguez, R.; Coffey, J. L.; Reissner, M. *Nanoscale* **2015**, 7 (47), 20220.
125. Granitzer, P.; Rumpf, K.; Gonzalez, R.; Coffey, J.; Reissner, M. *Nanoscale Research Letters* **2014**, 9 (1), 413.
126. Coey, J. M. D. *Physical Review Letters* **1971**, 27 (17), 1140.
127. Petri-Fink, A.; Hofmann, H. *IEEE Transactions on NanoBioscience* **2007**, 6 (4), 289.
128. Rumpf, K.; Granitzer, P.; Morales, P. M.; Poelt, P.; Reissner, M. *Nanoscale Research Letters* **2012**, 7 (1), 445.
129. Riemer, J.; Hoepken, H. H.; Czerwinska, H.; Robinson, S. R.; Dringen, R. *Analytical Biochemistry* **2004**, 331 (2), 370.

130. Pereira, C.; Pereira, A. M.; Rocha, M.; Freire, C.; Geraldés, C. F. G. C. *Journal of Materials Chemistry B* **2015**, 3 (30), 6261.
131. Tong, S.; Hou, S.; Zheng, Z.; Zhou, J.; Bao, G. *Nano Letters* **2010**, 10 (11), 4607.
132. Zhou, Z.; Zhao, Z.; Zhang, H.; Wang, Z.; Chen, X.; Wang, R.; Chen, Z.; Gao, J. *ACS Nano* **2014**, 8 (8), 7976.
133. Huang, G.; Li, H.; Chen, J.; Zhao, Z.; Yang, L.; Chi, X.; Chen, Z.; Wang, X.; Gao, J. *Nanoscale* **2014**, 6 (17), 10404.
134. Hatakeyama, M.; Kishi, H.; Kita, Y.; Imai, K.; Nishio, K.; Karasawa, S.; Masaike, Y.; Sakamoto, S.; Sandhu, A.; Tanimoto, A.; Gomi, T.; Kohda, E.; Abe, M.; Handa, H. *Journal of Materials Chemistry* **2011**, 21 (16), 5959.
135. Paquet, C.; de Haan, H. W.; Leek, D. M.; Lin, H.-Y.; Xiang, B.; Tian, G.; Kell, A.; Simard, B. *ACS Nano* **2011**, 5 (4), 3104.
136. Allkemper, T.; Bremer, C.; Matuszewski, L.; Ebert, W.; Reimer, P. *Radiology* **2002**, 223 (2), 432.
137. Qin, J.; Laurent, S.; Jo, Y. S.; Roch, A.; Mikhaylova, M.; Bhujwalla, Z. M.; Muller, R. N.; Muhammed, M. *Advanced Materials* **2007**, 19 (14), 1874.
138. Tilborg, G. A. F. V.; Cormode, D. P.; Jarzyna, P. A.; Toorn, A. V. D.; Susanne M. A. Van Der Pol; Bloois, L. V.; Fayad, Z. A.; Storm, G.; Mulder, W. J. M.; Vries, H. E. D.; Dijkhuizen, R. M. *Bioconjugate Chemistry* **2012**, 23 (5), 941.
139. Ahmed, M. I.; Habib, A.; Javaid, S. S. *International Journal of Photoenergy* **2015**, 2015, 1.
140. Castellano, R. N. *Solar panel processing*; Old City Publishing, Inc.: Philadelphia, PA, 2010..

141. O'regan, B.; Grätzel, M. *Nature* **1991**, 353 (6346), 737.
142. Kulkarni, S. A.; Baikie, T.; Boix, P. P.; Yantara, N.; Mathews, N.; Mhaisalkar, S. *Journal Materials Chemistry A* **2014**, 2 (24), 9221.
143. Wehrenfennig, C.; Eperon, G. E.; Johnston, M. B.; Snaith, H. J.; Herz, L. M. *Advanced Materials* **2013**, 26 (10), 1584.
144. Eperon, G. E.; Stranks, S. D.; Menelaou, C.; Johnston, M. B.; Herz, L. M.; Snaith, H. J. *Energy & Environmental Science* **2014**, 7 (3), 982.
145. Troughton, J.; Charbonneau, C.; Carnie, M. J.; Davies, M. L.; Worsley, D. A.; Watson, T. M. *Journal of Materials Chemistry A* **2015**, 3 (17), 9123.
146. Kazim, S.; Nazeeruddin, M. K.; Grätzel, M.; Ahmad, S. *Angewandte Chemie International Edition* **2014**, 53 (11), 2812.
147. Zhu, H.; Fu, Y.; Meng, F.; Wu, X.; Gong, Z.; Ding, Q.; Gustafsson, M. V.; Trinh, M. T.; Jin, S.; Zhu, X.-Y. *Nature Materials* **2015**, 14 (6), 636.
148. Veldhuis, S. A.; Boix, P. P.; Yantara, N.; Li, M.; Sum, T. C.; Mathews, N.; Mhaisalkar, S. G. *Advanced Materials* **2016**, 28 (32), 6804.
149. Dou, L.; Yang, Y. (M.); You, J.; Hong, Z.; Chang, W.-H.; Li, G.; Yang, Y. *Nature Communications* **2014**, 5, 5404.
150. Kojima, A.; Teshima, K.; Shirai, Y.; Miyasaka, T. *Journal of the American Chemical Society* **2009**, 131 (17), 6050.
151. Oxford Photovoltaics <http://www.oxfordpv.com/> (accessed Mar 1, 2016).
152. Zheng, L.; Zhang, D.; Ma, Y.; Lu, Z.; Chen, Z.; Wang, S.; Xiao, L.; Gong, Q. *Dalton Transactions* **2015**, 44 (23), 10582.

153. Xing, J.; Liu, X. F.; Zhang, Q.; Ha, S. T.; Yuan, Y. W.; Shen, C.; Sum, T. C.; Xiong, Q. *Nano Letters* **2015**, *15* (7), 4571.
154. Schmidt, L. C.; Pertegás, A.; González-Carrero, S.; Malinkiewicz, O.; Agouram, S.; Espallargas, G. M.; Bolink, H. J.; Galian, R. E.; Pérez-Prieto, J. *Journal of the American Chemical Society* **2014**, *136* (3), 850.
155. Gonzalez-Rodriguez, R.; Arad-Vosk, N.; Rozenfeld, N.; Sa'ar, A.; Coffey, J. L. *Small* **2016**, *12* (33), 4477.
156. Ong, K. P.; Goh, T. W.; Xu, Q.; Huan, A. *The Journal of Physical Chemistry Letters* **2015**, *6* (4), 681.
157. Arad-Vosk, N.; Rozenfeld, N.; Gonzalez-Rodriguez, R.; Coffey, J. L.; Sa'Ar, A. *Physical Review B* **2017**, *95* (8).
158. Kim, J.; Lee, S.; Lee, J.; Hong, K. *The Journal of Physical Chemistry Letters* **2014**, *5*, 1312.
159. Kim, J.; Lee, S.-H.; Chung, C.-H.; Hong, K.-H. *Phys. Chem. Chem. Phys.* **2016**, *18* (6), 4423.
160. Yang, Y.; You, J. *Nature* **2017**, *544* (7649), 155.
161. Docampo, P.; Ball, J.; Darwich, M.; Eperon, G.; Snaith, H. *Nature Communications* **2013**, *4*, 2761.
162. Petrus, M. L.; Bein, T.; Dingemans, T. J.; Docampo, P. *Journal Materials Chemistry A* **2015**, *3* (23), 12159.
163. Suzuki, A.; Okada, H.; Oku, T. *Energies* **2016**, *9* (5), 376.
164. *Keithley: 1998 catalog & reference*. Cleveland, OH: Keithley Instruments Inc, 1998. Print.

165. Würfel, P. *Physics of solar cells: from principles to new concepts*; Wiley-VCH Verlag: Weinheim, 2008.
166. Wolf, M.; Rauschenbach, H. *Advanced Energy Conversion* **1963**, 3 (2), 455.
167. Shi, D.; Qin, X.; Li, Y.; He, Y.; Zhong, C.; Pan, J.; Dong, H.; Xu, W.; Li, T.; Hu, W.; Bredas, J.-L.; Bakr, O. M. *Science Advances* **2016**, 2 (4).
168. Mohammadian, N.; Moshaii, A.; Alizadeh, A.; Gharibzadeh, S.; Mohammadpour, R. *The Journal of Physical Chemistry Letters* **2016**, 7 (22), 4614.

Vita

Roberto Gonzalez Rodriguez was born in Apaxtla, Guerrero, Mexico on November 18, 1988. He is child of Roberto Gonzalez Garcia and Georgina Rodriguez Villalobos. He graduated in 2011 from Universidad de las Americas Puebla, Mexico. He got a Bachelor in of Science with a major in Nanotechnology. After graduation from college, Roberto Gonzalez Rodriguez entered Texas Christian University in August 2011 under the direction of Dr. Jeffery L Coffey to do research in Silicon Nanotubes.

Abstract
Silicon Nanotubes and Selected Investigations in Energy and Biomaterial Applications

Roberto Gonzalez Rodriguez
Department of Chemistry & Biochemistry

Advisor: Dr. Jeffery L. Coffey

Silicon (Si) remains the key material for electronic devices. The ability to fabricate silicon in nanostructure form is important not only to the next generation of such devices, but also in other applications relying on enhanced surface area, low dimensionality, and structural control, such as photovoltaics, battery technology, biosensing/therapeutics and magnetic resonance imaging (MRI) contrast agents.

In this presentation, we describe the basic fabrication steps for arrays of Silicon nanotubes (Si NTs) based on (1) deposition of silane (SiH_4) on a preformed ZnO nanowire array template on FTO glass or Si wafer substrates, followed by (2) sacrificial etching of the ZnO phase, resulting in the desired nanotube product. Hollow nanotube inner diameter is adjustable by size selection of the initial ZnO nanowire, while shell thickness control is achieved by concentration/duration of silicon deposition.

High surface area silicon structures are of great interest in battery applications. In one study, the synthesis and characterization of porous Si NTs arrays on stainless steel substrates was achieved. We show that this type of self-supported Si NTs electrode exhibits interesting electrochemical properties for high performance Lithium Ion Batteries (LIB). For example, a gravimetric capacity of 800 mAhg^{-1} up to 180 cycles was measured in a porous Si NT anode with a 10 nm sidewall thickness.

Fe_3O_4 nanoparticles (Fe_3O_4 NPs) are currently under investigation for possible utility in magnetic assisted drug delivery and possible MRI contrast agents. Fe_3O_4 NPs of different sizes (5 and 8 nm) were infiltrated into SiNTs with 40- and 70-nm wall thicknesses. The infiltration process performed at room temperature is supported by a magnetic field to assure optimal filling of the nanotubes. To determine the efficiency of MRI contrast agents, we measured the relaxivities of the above materials, both longitudinal r_1 and transverse r_2 in water and PBS at 37 °C. The r_2/r_1 ratios are higher when present in the nanotubes than for Fe_3O_4 NPs in suspension. All samples showed a relaxivity ratio $r_2/r_1 > 2$, placing them in the category of negative contrast agent.

Organometal perovskites have implications in photovoltaics and light emitting diodes (LEDs). We demonstrate here the formation of organolead perovskite ($\text{CH}_3\text{NH}_3\text{PbI}_3$) nanostructures of 30 nm, 70 nm and 200 nm thickness whose width is dictated by the inner diameter of a silicon nanotube (Si NT) template. Structural characterization of these structures is achieved via a combination of electron microscopies (SEM, TEM, and high resolution lattice imaging) with associated energy dispersive elemental analysis. After structural characterization, the photophysical properties of these perovskite nanostructures, in terms of optical absorption and photoluminescence (PL) as a function of temperature, were evaluated.

The above studies set the stage for further investigations of the utility of these semiconducting nanotubes for a broad spectrum of possible useful applications.